

Global Carbon Budget 2023

Supplementary Information

S.1 Methodology Fossil Fuel CO₂ emissions (E_{FOS})

S.1.1 Cement carbonation

From the moment it is created, cement begins to absorb CO₂ from the atmosphere, a process known as ‘cement carbonation’. We estimate this CO₂ sink, from 1931 onwards, as the average of two studies in the literature (Cao et al., 2020; Guo et al., 2021 extended by Huang et al., 2023). The Global Cement and Concrete Association reports a much lower carbonation rate, but this is based on the highly conservative assumption of 0% mortar (GCCA, 2021). Modelling cement carbonation requires estimation of a large number of parameters, including the different types of cement material in different countries, the lifetime of the structures before demolition, of cement waste after demolition, and the volumetric properties of structures, among others (Xi et al., 2016). Lifetime is an important parameter because demolition results in the exposure of new surfaces to the carbonation process. The main reasons for differences between the two studies appear to be the assumed lifetimes of cement structures and the geographic resolution, but the uncertainty bounds of the two studies overlap.

S.1.2 Emissions embodied in goods and services

CDIAC, UNFCCC, and BP national emission statistics ‘include greenhouse gas emissions and removals taking place within national territory and offshore areas over which the country has jurisdiction’ (Rypdal et al., 2006), and are called territorial emission inventories. Consumption-based emission inventories allocate emissions to products that are consumed within a country, and are conceptually calculated as the territorial emissions minus the ‘embodied’ territorial emissions to produce exported products plus the emissions in other countries to produce imported products (Consumption = Territorial – Exports + Imports). Consumption-based emission attribution results (e.g. Davis and Caldeira, 2010) provide additional information to territorial-based emissions that can be used to understand emission drivers (Hertwich and Peters, 2009) and quantify emission transfers by the trade of products between countries (Peters et al., 2011a). The consumption-based emissions have the same global total, but reflect the trade-driven movement of emissions across the Earth's surface in response to human activities. We estimate consumption-based emissions from 1990-2020 by enumerating the global supply chain using a global model of the economic relationships between economic sectors within and between every country (Andrew and Peters, 2013; Peters et al., 2011b). Our analysis is based on the economic and trade data from the Global Trade and Analysis Project (GTAP; Narayanan et al., 2015), and we make detailed estimates for the years 1997 (GTAP version 5), 2001 (GTAP6), and 2004, 2007, 2011, and 2014 (GTAP10.0a), covering 57 sectors and 141 countries and regions. The detailed results are then extended into an annual time series from 1990 to the latest year of the Gross Domestic Product (GDP) data (2020 in this budget), using GDP data by expenditure in current exchange rate of US dollars (USD; from the UN National Accounts main Aggregates

database; UN, 2022) and time series of trade data from GTAP (based on the methodology in Peters et al., 2011b). We estimate the sector-level CO₂ emissions using the GTAP data and methodology, add the flaring and cement emissions from our fossil CO₂ dataset, and then scale the national totals (excluding bunker fuels) to match the emission estimates from the carbon budget. We do not provide a separate uncertainty estimate for the consumption-based emissions, but based on model comparisons and sensitivity analysis, they are unlikely to be significantly different than for the territorial emission estimates (Peters et al., 2012b).

S.1.3 Uncertainty assessment for E_{FOS}

We estimate the uncertainty of the global fossil CO₂ emissions at $\pm 5\%$ (scaled down from the published $\pm 10\%$ at $\pm 2\sigma$ to the use of $\pm 1\sigma$ bounds reported here; Andres et al., 2012). This is consistent with a more detailed analysis of uncertainty of $\pm 8.4\%$ at $\pm 2\sigma$ (Andres et al., 2014) and at the high-end of the range of $\pm 5\text{--}10\%$ at $\pm 2\sigma$ reported by (Ballantyne et al., 2015). This includes an assessment of uncertainties in the amounts of fuel consumed, the carbon and heat contents of fuels, and the combustion efficiency. While we consider a fixed uncertainty of $\pm 5\%$ for all years, the uncertainty as a percentage of emissions is growing with time because of the larger share of global emissions from emerging economies and developing countries (Marland et al., 2009). Generally, emissions from mature economies with good statistical processes have an uncertainty of only a few per cent (Marland, 2008), while emissions from strongly developing economies such as China have uncertainties of around $\pm 10\%$ (for $\pm 1\sigma$; Gregg et al., 2008; Andres et al., 2014). Uncertainties of emissions are likely to be mainly systematic errors related to underlying biases of energy statistics and to the accounting method used by each country.

S.1.4 Growth rate in emissions

We report the annual growth rate in emissions for adjacent years (in percent per year) by calculating the difference between the two years and then normalising to the emissions in the first year: $(E_{FOS}(t_0+1) - E_{FOS}(t_0))/E_{FOS}(t_0) \times 100\%$. We apply a leap-year adjustment where relevant to ensure valid interpretations of annual growth rates. This affects the growth rate by about 0.3% yr⁻¹ ($1/366$) and causes calculated growth rates to go up approximately 0.3% if the first year is a leap year and down 0.3% if the second year is a leap year.

The relative growth rate of E_{FOS} over time periods of greater than one year can be rewritten using its logarithm equivalent as follows:

$$\frac{1}{E_{FOS}} \frac{dE_{FOS}}{dt} = \frac{d(\ln E_{FOS})}{dt} \quad (2)$$

Here we calculate relative growth rates in emissions for multi-year periods (e.g. a decade) by fitting a linear trend to $\ln(E_{FOS})$ in Eq. (2), reported in percent per year.

S.1.5 Emissions projection for 2023

To gain insight on emission trends for 2023, we provide an assessment of global fossil CO₂ emissions, E_{FOS} , by combining individual assessments of emissions for China, USA, the EU, and India (the four countries/regions with the largest emissions), and the rest of the world.

The methods are specific to each country or region, as described in detail below.

China: We use a regression between monthly data for each fossil fuel and cement, and annual data for consumption of fossil fuels / production of cement to project full-year growth in fossil fuel consumption and cement production. The monthly data for each product consists of the following:

- Coal: Production data from the National Bureau of Statistics (NBS), plus net imports from the China Customs Administration (i.e., gross supply of coal, not including inventory changes), adjusted using monthly production data for thermal electricity, crude steel, pig iron, coke and cement from NBS.
- Oil: Production data from NBS, plus net imports from the China Customs Administration (i.e., gross supply of oil, not including inventory changes)
- Natural gas: Same as for oil
- Cement: Production data from NBS

For oil, we use data for production and net imports of refined oil products rather than crude oil. This choice is made because refined products are one step closer to actual consumption, and because crude oil can be subject to large market-driven and strategic inventory changes that are not captured by available monthly data. Furthermore, refinery output in 2022 was atypically low through August of that year compared to the rest of the year, which results in very high growth figures for the 2023 data compared to what one can likely expect for the last four months of this year. The estimate has been adjusted down by 0.8 percentage points to account for this, corresponding to how much lower the ratio of January-August and September-December refinery output was in 2022 compared to the average for 2014-2022.

For each fuel and cement, we make a Bayesian linear regression between year-on-year cumulative growth in supply (production for cement) and full-year growth in consumption (production for cement) from annual consumption data. In the regression model, the growth rate in annual consumption (production for cement) is modelled as a regression parameter multiplied by the cumulative year-on-year growth rate from the monthly data through August of each year for past years (through 2022). We use broad Gaussian distributions centered around 1 as priors for the ratios between annual and through-August growth rates. We then use the posteriors for the growth rates together with cumulative monthly supply/production data through August of 2023 to produce a posterior predictive distribution for the full-year growth rate for fossil fuel consumption / cement production in 2023.

If the growth in supply/production through August were an unbiased estimate of the full-year growth in consumption/production, the posterior distribution for the ratio between the monthly and annual growth rates would be centered around 1. However, in practice the ratios are different from 1 (in most cases below 1). This is a result of various biasing factors such as uneven evolution in the first and second half of each year, inventory changes that are somewhat anti-correlated with production and net imports, differences in statistical coverage, and other factors that are not captured in the monthly data.

For fossil fuels, the mean of the posterior distribution is used as the central estimate for the growth rate in 2023, while the edges of a 68% credible interval (analogous to a 1-sigma confidence interval) are used for the upper and lower bounds.

USA: We use emissions estimated by the U.S. Energy Information Administration (EIA) in their Short-Term Energy Outlook (STEO) for emissions from fossil fuels to get both YTD and a full year projection (EIA, 2022). The STEO also includes a near-term forecast based on an energy forecasting model which is updated monthly (last update with preliminary data through August 2023), and takes into account expected temperatures, household expenditures by fuel type, energy markets, policies, and other effects. We combine this with our estimate of emissions from cement production using the monthly U.S. cement clinker production data from USGS for January-July 2023, assuming changes in clinker production over the first part of the year apply throughout the year.

India: We use monthly emissions estimates for India updated from Andrew (2020b) through July/August 2023. These estimates are derived from many official monthly energy and other activity data sources to produce direct estimates of national CO₂ emissions, without the use of proxies. Emissions from coal are then extended to September using a regression relationship based on power generated from coal, coal dispatches by Coal India Ltd., the composite PMI, time, and days per month. For the last 3-5 months of the year, each series is extrapolated assuming typical (pre-2019) trends.

EU: We use a refinement to the methods presented by Andrew (2021), deriving emissions from monthly energy data reported by Eurostat. Some data gaps are filled using data from the Joint Organisations Data Initiative (JODI, 2022). Sub-annual cement and cement-clinker production data are limited, but data for Germany, Poland and Spain, the three largest producers, suggest a decline of over 10%. For fossil fuels this provides estimates through July. We extend coal emissions through September using a regression model built from generation of power from hard coal, power from brown coal, and the number of working days in Germany, the biggest coal consumer in the EU. These are then extended through the end of the year assuming typical trends. We extend oil emissions by building a regression model between our monthly CO₂ estimates and oil consumption reported by the EIA for Europe in its Short-Term Energy Outlook (September edition), and then using this model with EIA's monthly forecasts. For natural gas, the strong seasonal signal allows the use of the bias-adjusted Holt-Winters exponential smoothing method (Chatfield, 1978), although this comes with larger uncertainty given the unusual energy situation in Europe in 2022-23.

Rest of the world: We use the close relationship between the growth in GDP and the growth in emissions (Raupach et al., 2007) to project emissions for the current year. This is based on a simplified Kaya Identity, whereby E_{FOS} (GtC yr⁻¹) is decomposed by the product of GDP (USD yr⁻¹) and the fossil fuel carbon intensity of the economy (I_{FOS} ; GtC USD⁻¹) as follows:

$$E_{FOS} = GDP \times I_{FOS} \quad (3)$$

Taking a time derivative of Equation (3) and rearranging gives:

$$\frac{1}{E_{FOS}} \frac{dE_{FOS}}{dt} = \frac{1}{GDP} \frac{dGDP}{dt} + \frac{1}{I_{FOS}} \frac{dI_{FOS}}{dt} \quad (4)$$

where the left-hand term is the relative growth rate of E_{FOS} , and the right-hand terms are the relative growth rates of GDP and I_{FOS} , respectively, which can simply be added linearly to give the overall growth rate.

The I_{FOS} is based on GDP in constant PPP (Purchasing Power Parity) from the International Energy Agency (IEA) up to 2017 (IEA/OECD, 2019) and extended using the International Monetary Fund (IMF) growth rates

through 2022 (IMF, 2023). Interannual variability in I_{FOS} is the largest source of uncertainty in the GDP-based emissions projections. We thus use the standard deviation of the annual IFOS for the period 2013-2022 as a measure of uncertainty, reflecting a $\pm 1\sigma$ as in the rest of the carbon budget. For rest-of-world oil emissions growth, we use the global oil demand forecast published by the EIA less our projections for the other four regions, and estimate uncertainty as the maximum absolute difference over the period available for such forecasts using the specific monthly edition (e.g. August) compared to the first estimate based on more solid data in the following year (April).

World: The global total is the sum of each of the countries and regions.

S.2 Methodology CO₂ emissions from land-use, land-use change and forestry (E_{LUC})

The net CO₂ flux from land-use, land-use change and forestry (E_{LUC}, called land-use change emissions in the rest of the text) includes CO₂ fluxes from deforestation, afforestation, logging and forest degradation (including harvest activity), shifting cultivation (cycle of cutting forest for agriculture, then abandoning), and regrowth of forests following wood harvest or abandonment of agriculture. Land-management activities are only partly included in our land-use change emissions estimates (Table S1). Emissions from peat burning and peat drainage are added from external datasets (see Supplement S.2.1 below). Some land-use change and land-management activities cause emissions of CO₂ to the atmosphere, while others remove CO₂ from the atmosphere. E_{LUC} is the net sum of emissions and removals due to all anthropogenic activities considered. Our annual estimates for 1960-2022 are provided as the average of results from three bookkeeping approaches (Supplement S.2.1 below): an estimate using the Bookkeeping of Land Use Emissions model (Hansis et al., 2015; hereafter BLUE), one using the compact Earth system model OSCAR (Gasser et al., 2020), and an estimate published by Houghton and Castanho (2023; hereafter H&C2023, an updated version of the formerly used model H&N2017). BLUE and OSCAR are updated with new land-use forcing data covering the time period until 2022. All three data sets are extrapolated to provide a projection for 2023 (see Supplement S.2.5 below). In addition, we use results from Dynamic Global Vegetation Models (DGVMs; see Supplement S.2.2 and Table 4) to help quantify the uncertainty in E_{LUC} (Supplement S.2.4), and thus better characterise our understanding of the robustness of annual estimates and trends. Note that in this budget, we follow the scientific E_{LUC} definition as used by global carbon cycle models, which counts fluxes due to environmental changes on managed land towards S_{LAND}, as opposed to the national greenhouse gas inventories under the UNFCCC, most of which include them in E_{LUC} and thus often report smaller land-use emissions (Grassi et al., 2018; Petrescu et al., 2020). Following the methodology of Grassi et al. (2023), we provide harmonised estimates of the two approaches further below (see Supplement S.2.3).

S.2.1 Bookkeeping models

CO₂ emissions and removals from land-use change are calculated by three bookkeeping models. These are based on the original bookkeeping approach of Houghton (2003), which keeps track of the carbon stored in vegetation and soils before and after a land-use change event (transitions between various natural vegetation types, croplands, and pastures). Literature-based response curves describe decay of vegetation and soil carbon, including transfer to product pools of different lifetimes, as well as carbon uptake due to regrowth. In addition, the bookkeeping models represent long-term degradation of primary forest as lowered standing vegetation and soil carbon stocks in secondary forests, and include forest management practices such as wood harvests.

BLUE and H&C2023 exclude the transient response of land ecosystems to changes in climate, atmospheric CO₂, and other environmental factors, and base the carbon densities of soil and vegetation on contemporary data from literature and inventory data. Since carbon densities thus remain fixed over time, the additional sink capacity that ecosystems provide in response to CO₂-fertilisation and some other environmental changes are not captured by these models (Pongratz et al., 2014). On the contrary, OSCAR includes this transient response, and it follows a theoretical framework (Gasser and Ciais, 2013) that allows separating bookkeeping land-use emissions and the loss of additional sink capacity. Only the former is included here, while the latter is discussed in Supplement S6.4. The bookkeeping models differ in (1) computational units (spatially explicit treatment of land-use change at 0.25° resolution for BLUE, country-level for H&C2023 and OSCAR), (2) processes represented (see Table S1), and (3) carbon densities assigned to vegetation and soils for different types of vegetation (literature-based for BLUE and H&C2023, calibrated to DGVMs for OSCAR). A notable difference between models exists with respect to the treatment of shifting cultivation: H&C2023 assumes that forest loss—derived from the Global Forest Resources Assessment (FRA; FAO, 2020)—in excess of increases in cropland and pastures—derived from FAOSTAT (FAO, 2021)—represents an increase in shifting cultivation. If the excess loss of forests in a year is negative, it is assumed that shifting cultivation is returned to forest. Historical areas in shifting cultivation are defined taking into account country-based estimates of areas in fallow in 1980 (FAO/UNEP, 1981) and expert opinion (from Heinimann et al., 2017). In contrast, BLUE and OSCAR include subgrid-scale transitions between all vegetation types. Furthermore, H&C2023 assumes conversion of natural grasslands to pasture, while BLUE and OSCAR allocate pasture transitions proportionally to all natural vegetation that exists in a grid-cell. This is one reason for generally higher emissions in BLUE and OSCAR. In this GCB, we split CO₂ emissions into emissions from permanent deforestation and from deforestation for shifting cultivation. Similarly, we separate the forest (re-)growth estimates into (re-)growth from af/reforestation and from regrowth associated with shifting cultivation. This distinction is insightful with regard to the levers on the reduction of net emissions: as deforestation for shifting cultivation is only temporary, the associated CO₂ emissions cannot easily be avoided without compromising the CO₂ removals from regrowth in shifting cultivation cycles. By contrast, permanent deforestation is typically not directly related to af/reforestation. Stopping deforestation for permanent agricultural expansion and increasing the forest area provide two independent paths towards net emissions reduction.

Bookkeeping models do not directly capture carbon emissions from the organic layers of drained peat soils nor from peat fires. Particularly the latter can create large emissions and interannual variability due to synergies of land-use and climate variability in equatorial Southeast Asia, particularly during El-Niño events. To correct for this, we add peat fire emissions based on the Global Fire Emission Database (GFED4s; van der Werf et al., 2017) to the bookkeeping models' output. Peat fire emissions are calculated by multiplying the mass of dry matter emitted by peat fires with the C emission factor for peat fires indicated in the GFED4s database. Emissions from deforestation and degradation fires (used for extrapolating the H&C2023 data beyond 2020 and to derive the 2023 projection of all three models; see below) are calculated analogously. The satellite-derived estimates of peat fire emissions start in 1997 only. We thus follow the approach by Houghton and Nassikas (2017) for earlier years, which linearly ramps up from zero emissions in 1980 to 0.04 GtC yr⁻¹ in 1996, reflecting the onset of major clearing of peatlands in equatorial Southeast Asia in the 1980s. Similarly, we add estimates of peat drainage emissions, combining estimates from three spatially explicit datasets. We employ

225 FAO peat drainage emissions 1990–2020 from croplands and grasslands (Conchedda and Tubiello, 2020), peat
 226 drainage emissions 1700–2010 from simulations with the DGVM ORCHIDEE-PEAT (Qiu et al., 2021), and
 227 peat drainage emissions 1701–2021 from simulations with the DGVM LPX-Bern v1.5 (Lienert and Joos, 2018;
 228 Müller and Joos, 2021), the latter applying the updated LUH2-GCB2023 forcing as also used by BLUE,
 229 OSCAR, and the DGVMs. The LPX-Bern industrial period simulations started from a transient run over the last
 230 deglaciation (-20,050 to 1700 AD) following Müller and Joos (2020) and are forced by changes in climate,
 231 atmospheric CO₂, nitrogen deposition/input, and land-use changes. Simulations were done with/without
 232 prescribing the human land-use changes since 1700 AD, the difference of which yields anthropogenic peat
 233 drainage emissions. Peat carbon is stored in (i) active peatlands, (ii) former peatlands (“natural”), and (iii)
 234 former peatlands under anthropogenic use. We adopt the average of the two CO₂ emission cases of Müller and
 235 Joos (2021) by assuming that half of the peat carbon is lost to the atmosphere immediately after ecosystem or
 236 land-use transformation of active to former peatland, while the rest is decaying slowly, pending on local
 237 temperature and soil moisture. The LPX-Bern peat drainage emissions show a very high emission peak in
 238 Russia in 1959 followed by very low emissions in 1960. This peak can be attributed to an artefact in the
 239 HYDE3.3 dataset (Friedlingstein et al. 2022a), which was corrected for Brazil and the Democratic Republic of
 240 the Congo in GCB2022 (Friedlingstein et al. 2022b) but remains for Russia where it strongly impacts the LPX-
 241 Bern peat drainage estimates in 1959 and 1960. To correct for this unrealistic peak, we replace the LPX-Bern
 242 peat drainage emissions in Russia in 1959 and 1960 by the average of the estimates in 1958 and 1961. FAO data
 243 are extrapolated to 1850-2022 by keeping the post-2020 emissions constant at 2020 levels and by linearly
 244 increasing tropical peat drainage emissions between 1980 and 1990 starting from 0 GtC yr⁻¹ in 1980 (consistent
 245 with H&N2017’s assumption, Houghton and Nassikas, 2017), and by keeping pre-1990 emissions from the
 246 often old drained areas of the extra-tropics constant at 1990 emission levels. ORCHIDEE-PEAT data are
 247 extrapolated to 2011-2022 by replicating the average emissions in 2000-2010 (pers. comm. C. Qiu), and LPX-
 248 Bern data for 2022 are obtained by replicating the 2021 estimate. Further, ORCHIDEE-PEAT only provides
 249 peat drainage emissions north of 30°N, and thus we fill the regions south of 30°N by the average peat drainage
 250 emissions from FAO and LPX-Bern. Peat drainage emissions are calculated as the average of the estimates from
 251 the three different peat drainage datasets. The net *ELUC* values indicated in the manuscript are the sum of *ELUC*
 252 estimates from bookkeeping models, peat fire emissions, and peat drainage emissions.
 253 The three bookkeeping estimates used in this study differ with respect to the land-use change data used to drive
 254 the models. H&C2023 base their estimates directly on the Forest Resource Assessment (FRA) of the FAO,
 255 which provides statistics on forest-area change and management at intervals of five years currently updated until
 256 2020 (FAO, 2020). The data is based on country reporting to FAO and may include remote-sensing information
 257 in more recent assessments. Changes in land use other than forests are based on annual, national changes in
 258 cropland and pasture areas reported by the FAO (FAO, 2021). On the other hand, BLUE uses the harmonised
 259 land-use change data LUH2-GCB2023 covering the period 850-2022 (an update to the previously released
 260 LUH2 v2h dataset; Hurtt et al., 2017; Hurtt et al., 2020), which was also used as input to the DGVMs
 261 (Supplement S.2.2). LUH2-GCB2023 provides land-use change data at 0.25° spatial resolution based on the
 262 FAO data (as described in Supplement S.2.2) as well as the HYDE3.3 dataset (Klein Goldewijk et al., 2017a,
 263 2017b), considering subgrid-scale transitions between primary forest, secondary forest, primary non-forest,
 264 secondary non-forest, cropland, pasture, rangeland, and urban land (Hurtt et al., 2020; Chini et al., 2021).

LUH2-GCB2023 provides a distinction between rangelands and pasture, based on inputs from HYDE. To constrain the models' interpretation on whether rangeland implies the original natural vegetation to be transformed to grassland or not (e.g., browsing on shrubland), a forest mask was provided with LUH2-GCB2021; forest is assumed to be transformed to grasslands, while other natural vegetation remains (in case of secondary vegetation) or is degraded from primary to secondary vegetation (Ma et al., 2020). This is implemented in BLUE. OSCAR was run with both LUH2-GCB2023 and FAO/FRA, where the drivers of the latter were linearly extrapolated to 2022 using their 2015-2020 trends. The best-guess OSCAR estimate used in our study is a combination of results for LUH2-GCB2023 and FAO/FRA land-use data and a large number of perturbed parameter simulations weighted against a constraint (the cumulative S_{LAND} over 1960-2021 of last year's GCB). As the record of H&C2023 ends in 2020, we extend it up to 2022 by adding the yearly anomalies of the emissions from tropical deforestation and degradation fires from GFED4s between 2020 and 2022 to the model's estimate for 2020 (emissions from peat fires and peat drainage are added to all models later in the process).

The annual E_{LUC} from 1850 onwards is calculated as the average of the estimates from BLUE, H&C2023, and OSCAR. For the cumulative numbers starting in 1750, emission estimates between 1750-1850 are added based on the average of four earlier publications (30 ± 20 GtC 1750-1850, rounded to nearest 5; Le Quéré et al., 2016).

We provide an additional split of net E_{LUC} into component fluxes to better identify reasons for divergence between bookkeeping estimates and to give more insight into the drivers of net E_{LUC} . This split distinguishes between emissions from deforestation (including due to shifting cultivation), removals from forest (re-)growth (including regrowth in shifting cultivation cycles), fluxes from wood harvest and other forest management (i.e., emissions in forests from slash decay and emissions from product decay following wood harvesting, removals from regrowth associated with wood harvesting, and fire suppression), emissions from peat drainage and peat fires, and emissions and removals associated with all other land-use transitions. Additionally, we split deforestation emissions into emissions from permanent deforestation and emissions from deforestation in shifting cultivation cycles, and we split removals from forest (re-)growth into forest (re-)growth due to afforestation and forest regrowth in shifting cultivation cycles. This split helps to identify the emission reductions that would be achievable by halting permanent deforestation, and the removals that are caused by permanently increasing the forest cover through re/afforestation. E_{LUC} data are provided as global sums, as spatially explicit estimates at 0.25° spatial resolution (i.e., the native BLUE resolution), and for 199 countries (based on the list of UNFCCC parties). Spatially explicit E_{LUC} estimates for BLUE are directly available. For OSCAR and H&C2023, the country-level estimates were scaled to the 0.25° BLUE grid based on the patterns of gross emissions and gross removals in BLUE (see Schwingshackl et al. 2022 for more details about the methodology). The gridded net E_{LUC} estimates of BLUE, OSCAR, and H&C2023 are averaged, and the gridded estimates of peat drainage emissions (average of FAO, LPX-Bern, and ORCHIDEE-PEAT) and of peat fire emissions (from GFED4s) are added. Country-level estimates for the gridded datasets (BLUE, LPX-Bern, ORCHIDEE-PEAT, GFED4s) are calculated based on a country map from Eurostat (Countries 2020, 1:1 million, available at: <https://ec.europa.eu/eurostat/web/gisco/geodata/reference-data/administrative-units-statistical-units/countries>), which was remapped to 0.25° . In case multiple countries are present in a 0.25° grid cell, the E_{LUC} estimates are allocated proportional to each country's land fraction in that grid cell.

S.2.2 Dynamic Global Vegetation Models (DGVMs)

Land-use change CO₂ emissions have also been estimated using an ensemble of 20 DGVMs simulations. The DGVMs account for deforestation and regrowth, the most important components of E_{LUC}, but they do not represent all processes resulting directly from human activities on land (Table S1). All DGVMs represent processes of vegetation growth and mortality, as well as decomposition of dead organic matter associated with natural cycles, and include the vegetation and soil carbon response to increasing atmospheric CO₂ concentration and to climate variability and change. Most models explicitly simulate the coupling of carbon and nitrogen cycles and account for atmospheric N deposition and N fertilisers (Table S1). The DGVMs are independent from the other budget terms except for their use of atmospheric CO₂ concentration to calculate the fertilisation effect of CO₂ on plant photosynthesis.

All DGVMs use the LUH2-GCB2023 dataset as input, which includes the HYDE cropland/grazing land dataset (Klein Goldewijk et al., 2017a, 2017b), and some additional information on land-use transitions, land-use management activities and wood harvest. This includes annual, quarter-degree (regridded from 5 minute resolution), fractional data on cropland and pasture from HYDE3.3.

DGVMs that do not simulate subgrid-scale transitions (i.e., net land-use emissions; see Table S1) used the HYDE information on agricultural area change. For all countries, with the exception of Brazil, the Democratic Republic of the Congo, and Indonesia these data are based on the available annual FAO statistics of change in agricultural land area available from 1961 up to and including 2017. The FAO retrospectively revised their reporting for the Democratic Republic of the Congo, which was newly available until 2020 as reported in GCB2022. In addition to FAO country-level statistics, the HYDE3.3 cropland/grazing land dataset is constrained spatially based on multi-year satellite land cover maps from ESA CCI LC (see below). After the year 2017, HYDE3.3 extrapolates the cropland and pasture data based on the trend over the previous 5 years, to generate data until the year 2022. This methodology is not appropriate for countries that have experienced recent rapid changes in the rate of land-use change, e.g. Brazil which has experienced a recent upturn in deforestation. For Brazil and Indonesia we replace FAO state-level data for cropland and grazing land in HYDE by those from the satellite-based land cover dataset MapBiomas (collection 7) for 1985-2021 (Souza et al. 2020). ESA-CCI is used to spatially disaggregate as described below. Similarly, an estimate for the year 2022 is based on the MapBiomas trend 2016-2021. The pre-1985 period is scaled with the per capita numbers from 1985 from MapBiomas, so this transition is smooth.

HYDE uses satellite imagery from ESA-CCI from 1992 – 2018 for more detailed yearly allocation of cropland and grazing land, with the ESA area data scaled to match the FAO annual totals at country-level. The original 300 metre spatial resolution data from ESA was aggregated to a 5 arc minute resolution according to the classification scheme as described in Klein Goldewijk et al (2017a).

DGVMs that simulate subgrid-scale transitions (i.e., gross land-use emissions; see Table S1) use more detailed land use transition and wood harvest information from the LUH2-GCB2023 data set. LUH2-GCB2023 is an update of the comprehensive harmonised land-use data set (Hurtt et al., 2020), that includes fractional data on primary and secondary forest vegetation, as well as all underlying transitions between land-use states (850-2020; Hurtt et al., 2011, 2017, 2020; Chini et al., 2021; Table S1). This data set consists of quarter degree fractional areas of land-use states and all transitions between those states, including a new wood harvest reconstruction,

new representation of shifting cultivation, crop rotations, management information including irrigation and fertiliser application. The land-use states include five different crop types in addition to splitting grazing land into managed pasture and rangeland. Wood harvest patterns are constrained with Landsat-based tree cover loss data (Hansen et al. 2013). Updates of LUH2-GCB2023 over last year's version (LUH2-GCB2022) are using the most recent HYDE release (covering the time period up to 2022, revision to Indonesia as described above). We use updated FAO wood harvest data for all dataset years from 1961 to 2021, and linearly extended to the year 2023. The HYDE3.3 population data is also used to extend the wood harvest time series back in time. Other wood harvest inputs (for years prior to 1961) remain the same in LUH2. These updates in the land-use forcing are shown in Figure S6 in comparison to the more pronounced version change from the GCB2020 (Friedlingstein et al., 2020) to GCB2021, which was discussed in Friedlingstein et al. (2022a), and their relevance for land-use emissions is discussed in Section 3.2.2. DGVMs implement land-use change differently (e.g. an increased cropland fraction in a grid cell can either be at the expense of grassland or shrubs, or forest, the latter resulting in deforestation; land cover fractions of the non-agricultural land differ between models). Similarly, model-specific assumptions are applied to convert deforested biomass or deforested area, and other forest product pools into carbon, and different choices are made regarding the allocation of rangelands as natural vegetation or pastures.

The difference between two DGVMs simulations (see Supplement S.4.1 below), one forced with historical changes in land-use and a second one with time-invariant pre-industrial land cover and pre-industrial wood harvest rates, allows quantification of the dynamic evolution of vegetation biomass and soil carbon pools in response to land-use change in each model (E_{LUC}). Using the difference between these two DGVM simulations to diagnose E_{LUC} means the DGVM estimate includes the loss of additional sink capacity (around 0.4 ± 0.3 GtC yr⁻¹; see Section 2.10 and Supplement S.6.4), while the bookkeeping model estimate does not.

As a criterion for inclusion in this carbon budget, we only retain models that simulate a positive E_{LUC} during the 1990s, as assessed in the IPCC AR4 (Denman et al., 2007) and AR5 (Ciais et al., 2013). All DGVMs met this criterion.

S.2.3 Translation of national GHG inventory data to E_{LUC}

An approach was implemented to reconcile the large gap between land-use emissions estimates from bookkeeping models and from national GHG Inventories (NGHGI; see Tab. A9). This gap is due to different approaches for calculating “anthropogenic” CO₂ fluxes related to land-use change and land management (Grassi et al. 2018). In particular, the land sinks due to environmental change on managed lands are treated as non-anthropogenic in the global carbon budget, while they are generally considered as anthropogenic in NGHGIs (“indirect anthropogenic fluxes”; Eggleston et al., 2006). Building on previous studies (Grassi et al. 2021), the approach implemented here adds the DGVM estimates of CO₂ fluxes due to environmental change from managed forest areas (part of S_{LAND}) to the E_{LUC} estimate from bookkeeping models. This sum is expected to be conceptually more comparable to NGHGI estimates than E_{LUC} .

E_{LUC} data are taken from bookkeeping models, in line with the global carbon budget approach. To determine S_{LAND} in managed forest, the following steps were taken: Spatially gridded data of “natural” forest NBP (S_{LAND} i.e., including carbon fluxes due to environmental change and excluding land use change fluxes) were obtained from DGVMs using S2 runs from the TRENDY v13 dataset. Results were first masked with a forest map that is

based on tree cover data from Hansen et al. (2013). To perform the conversion “tree” cover to “forest” cover, we exclude gridcells with less than 20% tree cover and isolated pixels with maximum connectivity less than 0.5 ha following the FAO definition of forest. Forest NBP is then further masked with a map of “intact” forest for the year 2013, i.e. forest areas characterised by no remotely detected signs of human activity (Potapov et al. 2017). This way, we obtained S_{LAND} in “intact” and “non-intact” forest areas, which previous studies (Grassi et al. 2021) indicated to be a good proxy, respectively, for “unmanaged” and “managed” forest areas in the NGHGI. Note that only a subset of models had forest NBP at grid cell level. For the other DGVMs, when a grid cell had forest, all the NBP in that grid cell was allocated to forest. However, since S2 simulations use pre-industrial forest cover masks that are at least 20% larger than today’s forest (Hurtt et al. 2020), we corrected this NBP by a ratio between observed (based on Hansen et al. 2013) and prescribed (from DGVMs) forest cover. This ratio is calculated for each individual DGVM that provides information on prescribed forest cover, and a common ratio (median ratio of this subset of models) is used. The details of the method used are explained in a GitHub repository (Alkama, 2022).

LULUCF data from NGHGIS are from Grassi et al. (2023). While Annex I countries report a complete time series 1990-2021, gap-filling was applied for Non-Annex I countries through linear interpolation between two points and/or through extrapolation backward (till 1990) and forward (till 2022) using the single closest available data. For all countries, the estimates of the year 2022 are assumed to be equal to those of 2021. This data includes all CO₂ fluxes from land considered managed, which in principle encompasses all land uses (forest land, cropland, grassland, wetlands, settlements, and other land), changes among them, emissions from organic soils (i.e., from peat drainage) and from fires. In practice, although almost all Annex I countries report all land uses, many non-Annex I countries report only on deforestation and forest land, and only few countries report on other land uses. In most cases, NGHGIS include most of the natural response to recent environmental change because they use direct observations (e.g., national forest inventories) that do not allow separating direct and indirect anthropogenic effects (Eggleston et al., 2006).

Tab. A9 shows the resulting translation of global carbon cycle models' land flux definitions to that of the NGHGI (discussed in Section 3.2.2). For comparison we also show FAOSTAT emissions totals (FAO, 2021), which include emissions from net forest conversion and fluxes on forest land (Tubiello et al., 2021) as well as CO₂ emissions from peat drainage and peat fires. The 2021 data was estimated by including actual 2021 estimates for peatland drainage and fire and a carry forward from 2020 to 2021 for the forest land stock change. The FAO data shows global emissions of 0.25 GtC yr⁻¹ averaged over 2012-2021, in contrast to the removals of -0.66 GtC yr⁻¹ estimated by the gap-filled NGHGI data. Most of this difference is attributable to different scopes: a focus on carbon fluxes for the NGHGI and a focus on land-use area and biomass estimates for FAO. In particular, the NGHGI data includes a larger forest sink for non-Annex 1 countries resulting from a more complete coverage of non-biomass carbon pools and non-forest land uses. NGHGI and FAO data also differ in terms of underlying data on forest land (Grassi et al., 2022).

S.2.4 Uncertainty assessment for E_{LUC}

Differences between the bookkeeping models and DGVMs originate from three main sources: different methodologies, which among others lead to inclusion of the loss of additional sink capacity in DGVMs (see Supplement S.6.4), different underlying land-use/land cover datasets, and different processes represented (Table

S1). We examine both the results from DGVMs and from the bookkeeping method and use the resulting variations as a way to characterise the uncertainty in E_{LUC} . Despite the existing differences, the E_{LUC} estimate from the DGVM multi-model mean is consistent with the average of the emissions from the bookkeeping models (Table 5). However there are large differences among individual DGVMs (standard deviation at around 0.5 GtC yr^{-1} ; Table 5), between the bookkeeping estimates (average difference 1850-2022 BLUE-H&C2023 of 0.8 GtC yr^{-1} , BLUE-OSCAR of 0.4 GtC yr^{-1} , OSCAR-H&C2023 of 0.4 GtC yr^{-1}), and between the H&C2023 model and its previous model version H&N2017 (average difference 1850-2015 of 0.2 GtC yr^{-1} ; see Table 1 in Houghton and Castanho, 2023). A factorial analysis of differences between BLUE and H&N2017 (the precursor of H&C2023) attributed them particularly to differences in carbon densities between natural and managed vegetation or primary and secondary vegetation (Bastos et al., 2021). Earlier studies additionally showed the relevance of the different land-use forcing as applied (in updated versions) also in the current study (Gasser et al., 2020). Ganzenmüller et al. (2022) showed that E_{LUC} estimates with BLUE are substantially smaller when the model is driven by a new high-resolution land-use dataset (HILDA+). They identified shifting cultivation and the way it is implemented in LUH2 as a main reason for this divergence. They further showed that a higher spatial resolution reduces the estimates of both gross emissions and gross removals because successive transitions are not adequately represented at coarser resolution, which has the effect that—despite capturing the same extent of transition areas—overall less area remains pristine at the coarser compared to the higher resolution. The uncertainty in E_{LUC} of $\pm 0.7 \text{ GtC yr}^{-1}$ reflects our best value judgement that there is at least 68% chance ($\pm 1\sigma$) that the true land-use change emissions lie within the given range, for the range of processes considered here. Prior to the year 1959, the uncertainty in E_{LUC} is taken from the standard deviation of the DGVMs. We assign low confidence to the annual estimates of E_{LUC} because of the inconsistencies among estimates and because of the difficulties to quantify some of the processes with DGVMs.

S.2.5 Emissions projection for 2023

We project the 2023 land-use emissions for BLUE, H&C2023, and OSCAR based on their E_{LUC} estimates for 2022 and on the interannual variability of peat fires and tropical deforestation and degradation fires as estimated using active fire data (MCD14ML; Giglio et al., 2016). The latter scales almost linearly with GFED emissions estimates over large areas (van der Werf et al., 2017), and thus allows for tracking fire emissions in deforestation and tropical peat zones in near-real time. Peat drainage is assumed to be unaltered, as it has low interannual variability. The 2023 E_{LUC} estimate is calculated by summing the 2022 E_{LUC} estimate and the anomalies in peat fire emissions and tropical deforestation and degradation fire emissions (both from GFED4s), calculated as the difference between the estimates for 2022 and 2023. The GFED4s estimates for 2023 are as of September 29 2023.

S.3 Methodology Ocean CO_2 sink

S.3.1 Observation-based estimates

We primarily use the observational constraints assessed by IPCC of a mean ocean CO_2 sink of $2.2 \pm 0.7 \text{ GtC yr}^{-1}$ for the 1990s (90% confidence interval; Ciais et al., 2013) to verify that the GOBMs provide a realistic assessment of SOCEAN . This is based on indirect observations with seven different methodologies and their

uncertainties, and further using three of these methods that are deemed most reliable for the assessment of this quantity (Denman et al., 2007; Ciais et al., 2013). The observation-based estimates use the ocean/land CO₂ sink partitioning from observed atmospheric CO₂ and O₂/N₂ concentration trends (Manning and Keeling, 2006; Keeling and Manning, 2014), an oceanic inversion method constrained by ocean biogeochemistry data (Mikaloff Fletcher et al., 2006), and a method based on penetration time scale for chlorofluorocarbons (McNeil et al., 2003). The IPCC estimate of 2.2 GtC yr⁻¹ for the 1990s is consistent with a range of methods (Wanninkhof et al., 2013). We refrain from using the IPCC estimates for the 2000s (2.3 ± 0.7 GtC yr⁻¹), and the period 2002-2011 (2.4 ± 0.7 GtC yr⁻¹, Ciais et al., 2013) as these are based on trends derived mainly from models and one data-product (Ciais et al., 2013). Additional constraints summarised in AR6 (Canadell et al., 2021) are the interior ocean anthropogenic carbon change (Gruber et al., 2019) and ocean sink estimate from atmospheric CO₂ and O₂/N₂ (Tohjima et al., 2019) which are used for model evaluation and discussion, respectively.

We also use eight estimates of the ocean CO₂ sink and its variability based on surface ocean *f*CO₂ maps obtained by the interpolation of surface ocean *f*CO₂ measurements from 1990 onwards due to severe restriction in data availability prior to 1990 (Figure 10). These estimates differ in many respects: they use different maps of surface *f*CO₂, different atmospheric CO₂ concentrations, wind products and different gas-exchange formulations as specified in Table S3. We refer to them as *f*CO₂-based flux estimates. The measurements underlying the surface *f*CO₂ maps are from the Surface Ocean CO₂ Atlas version 2023 (SOCATv2023; Bakker et al., 2023), which is an update of version 3 (Bakker et al., 2016) and contains quality-controlled data through 2022 (see data attribution Table S6). Each of the estimates uses a different method to then map the SOCAT v2023 data to the global ocean. The methods include a data-driven diagnostic method combined with a multi linear regression approach to extend back to 1957 (Rödenbeck et al., 2022; referred to here as Jena-MLS), three neural network models (Landschützer et al., 2014; referred to as MPI-SOMFFN; Chau et al., 2022; Copernicus Marine Environment Monitoring Service, referred to here as CMEMS-LSCE-FFNN; and Zeng et al., 2022; referred to as NIES-ML3), one cluster regression approaches (Gregor and Gruber, 2021, referred to as OS-ETHZ-GRaCER), and a multi-linear regression method (Iida et al., 2021; referred to as JMA-MLR), and one method that relates the *f*CO₂ misfit between GOBMs and SOCAT to environmental predictors using the extreme gradient boosting method (Gloege et al., 2022). The ensemble mean of the *f*CO₂-based flux estimates is calculated from these seven mapping methods. Further, we show the flux estimate of Watson et al. (2020) who also use the MPI-SOMFFN method to map the adjusted *f*CO₂ data to the globe, but resulting in a substantially larger ocean sink estimate, owing to a number of adjustments they applied to the surface ocean *f*CO₂ data. Concretely, these authors adjusted the SOCAT *f*CO₂ downward to account for differences in temperature between the depth of the ship intake and the relevant depth right near the surface, and included a further adjustment to account for the cool surface skin temperature effect. The Watson et al. flux estimate hence differs from the others by their choice of adjusting the flux to a cool, salty ocean surface skin. Watson et al. (2020) showed that this temperature adjustment leads to an upward correction of the ocean carbon sink, up to 0.9 GtC yr⁻¹, that, if correct, should be applied to all *f*CO₂-based flux estimates. A reduction of this adjustment to 0.6 GtC yr⁻¹ was proposed by Dong et al. (2022). The impact of the cool skin effect on air-sea CO₂ flux is based on established understanding of temperature gradients (as discussed by Goddijn-Murphy et al 2015), and laboratory observations (Jähne and Haussecker, 1998; Jähne, 2019), but in situ field observational evidence is lacking

(Dong et al., 2022). A modelling study suggests that the skin effect is important but would be of smaller magnitude (about 0.1 GtC yr⁻¹ or 5%) due to a feedback of larger air-sea flux on ocean surface carbon concentration (Bellenger et al., 2023). The Watson et al flux estimate presented here is therefore not included in the ensemble mean of the *f*CO₂-based flux estimates. This choice will be re-evaluated in upcoming budgets based on further lines of evidence.

Typically, *f*CO₂-products do not cover the entire ocean due to missing coastal oceans and sea ice cover. The CO₂ flux from each *f*CO₂-based product is already at or above 99% coverage of the ice-free ocean surface area in two products (Jena-MLS, OS-ETHZ-GRaCER), and filled by the data-provider in three products (using Fay et al., 2021, method for JMA-MLR and LDEO-HPD; and adopting the Landschützer et al., 2020 geographical extension to cover marginal seas and coastal domains for MPI-SOMFFN). The products that did not undergo any area filling from their original published methodology and thus remained below 99% coverage of the ice-free ocean (CMEMS-LSCE-FFNN,, NIES-ML3, UOx-Watson) were scaled by the following procedure: Before v2022 of the GCB, the missing areas were accounted for by scaling the globally integrated fluxes by the fraction of the global ocean coverage (361.9e6 km² based on ETOPO1, Amante and Eakins, 2009; Eakins and Sharman, 2010) with the area covered by the CO₂ flux predictions. This approach may lead to unnecessary scaling when the majority of the missing data are in the ice-covered region (as is often the case), where flux is already assumed to be zero. Thus, since v2022 of the GCB we now scale fluxes globally and regionally (North, Tropics, South) to match the ice-free area (using the HadISST sea surface temperature and sea ice cover; Rayner et al., 2003):

$$FCO_2^{reg-scaled} = \frac{A_{(1-ice)}^{region}}{A_{FCO_2}^{region}} \cdot FCO_2^{region}$$

In the equation, *A* represents area, (1 – ice) represents the ice free ocean, *A*_{FCO₂}^{region} represents the coverage of the *f*CO₂-product for a region, and *FCO₂*^{region} is the integrated flux for a region.

We further use results from two diagnostic ocean models, Khatiwala et al. (2013) and DeVries (2014), to estimate the anthropogenic carbon accumulated in the ocean prior to 1959. The two approaches assume constant ocean circulation and biological fluxes, with *S*_{OCEAN} estimated as a response in the change in atmospheric CO₂ concentration calibrated to observations. The uncertainty in cumulative uptake of ±20 GtC (converted to ±1σ) is taken directly from the IPCC's review of the literature (Rhein et al., 2013), or about ±30% for the annual values (Khatiwala et al., 2009).

S.3.2 Global Ocean Biogeochemistry Models (GOBMs)

The ocean CO₂ sink for 1959-2022 is estimated using ten GOBMs (Table S2). The GOBMs represent the physical, chemical, and biological processes that influence the surface ocean concentration of CO₂ and thus the air-sea CO₂ flux. The GOBMs are forced by meteorological reanalysis and atmospheric CO₂ concentration data available for the entire time period. They mostly differ in the source of the atmospheric forcing data (meteorological reanalysis), spin up strategies, and in their horizontal and vertical resolutions (Table S2). All GOBMs except one (CESM-ETHZ) do not include the effects of anthropogenic changes in nutrient supply (Duce et al., 2008). They also do not include the perturbation associated with changes in riverine organic carbon (see Section 2.10 and Supplement S.6.3).

Four sets of simulations were performed with each of the GOBMs. Simulation A applied historical changes in climate and atmospheric CO₂ concentration. Simulation B is a control simulation with constant atmospheric forcing (normal year or repeated year forcing) and constant pre-industrial atmospheric CO₂ concentration. Simulation C is forced with historical changes in atmospheric CO₂ concentration, but repeated year or normal year atmospheric climate forcing. Simulation D is forced by historical changes in climate and constant pre-industrial atmospheric CO₂ concentration. To derive So_{CEAN} from the model simulations, we subtracted the slope of a linear fit to the annual time series of the control simulation B from the annual time series of simulation A. Assuming that drift and bias are the same in simulations A and B, we thereby correct for any model drift. Further, this difference also removes the natural steady state flux (assumed to be 0 GtC yr⁻¹ globally without rivers) which is often a major source of biases. Note, however, that Gürses et al. (2023) questioned the assumption of comparable bias and drift in simulations A and B as they compared two versions of FESOM-REcoM, and found a very similar air-sea CO₂ flux in simulation A despite a different bias as derived from simulation B. This approach works for all model set-ups, including IPSL, where simulation B was forced with constant atmospheric CO₂ but observed historical changes in climate (equivalent to simulation D). This approach assures that the interannual variability is not removed from IPSL simulation A. The absolute correction for bias and drift per model in the 1990s varied between <0.01 GtC yr⁻¹ and 0.31 GtC yr⁻¹, with five models having positive biases, four having negative biases and one model having essentially no bias (NorESM). The MPI model uses riverine input and therefore simulates outgassing in simulation B. By subtracting a linear fit of simulation B, also the ocean carbon sink of the MPI model follows the definition of So_{CEAN} . This correction reduces the model mean ocean carbon sink by 0.01 GtC yr⁻¹ in the 1990s. The ocean models cover 99% to 101% of the total ocean area, so that area-scaling is not necessary.

S.3.3 GOBM evaluation

The ocean CO₂ sink for all GOBMs and the ensemble mean falls within 90% confidence of the observed range, or 1.5 to 2.9 GtC yr⁻¹ for the 1990s (Ciais et al., 2013) before and after applying adjustments. An exception is the MPI model, which simulates a low ocean carbon sink of 1.38 GtC yr⁻¹ for the 1990s in simulation A owing to the inclusion of riverine carbon flux. After adjusting to the GCB's definition of So_{CEAN} by subtracting simulation B, the MPI model falls into the observed range with an estimated sink of 1.69 GtC yr⁻¹. The GOBMs and fCO_2 -products have been further evaluated using the fugacity of sea surface CO₂ (fCO_2) from the SOCAT v2023 database (Bakker et al., 2016, 2023). We focused this evaluation on the root mean squared error (RMSE) between observed and modelled fCO_2 and on a measure of the amplitude of the interannual variability of the flux (modified after Rödenbeck et al., 2015). The RMSE is calculated from detrended, annually and regionally averaged time series of fCO_2 calculated from GOBMs and fCO_2 -products subsampled to SOCAT sampling points to measure the misfit between large-scale signals (Hauck et al., 2020). To this end, we apply the following steps: (i) subsample data points for where there are observations (GOBMs/ fCO_2 -products as well as SOCAT), (ii) average spatially, (iii) calculate annual mean, (iv) detrend both time-series (GOBMs/ fCO_2 -products as well as SOCAT), (v) calculate RMSE. We use a mask based on the minimum area coverage of the fCO_2 -products. This ensures a fair comparison over equal areas. The amplitude of the So_{CEAN} interannual variability (A-IAV) is calculated as the temporal standard deviation of the detrended annual CO₂ flux time series after area-scaling (Rödenbeck et al., 2015, Hauck et al., 2020). These metrics are chosen because RMSE is the

most direct measure of data-model mismatch and the A-IAV is a direct measure of the variability of S_{OCEAN} on interannual timescales. We apply these metrics globally and by latitude bands. Results are shown in Figure S2 and discussed in Section 3.6.5.

In addition to the interior ocean anthropogenic carbon accumulation (Section 3.6.5) and SOCAT fCO_2 , we evaluate the models with process-based metrics that were previously related to ocean carbon uptake. These are the Atlantic Meridional Overturning Circulation (Goris et al., 2018, Terhaar et al., 2022, Terhaar et al., in review), the Southern Ocean sea surface salinity (Terhaar et al., 2021, 2022, in review, Hauck et al., in review), the Southern Ocean stratification index (Bourgeois et al., 2022) and the surface ocean Revelle factor (Terhaar et al., 2022, in review).

We follow the methodology of previous studies wherever possible, particularly the RECCAP model evaluation chapter (Terhaar et al., in review). The Atlantic Meridional Overturning Circulation from the GOBMs is here defined as the maximum of the Atlantic meridional overturning streamfunction at 26°N. This is compared to data from the RAPID array at 26°N (Moat et al., 2023). We use an uncertainty of 0.6 Sv following Terhaar et al. (in review) based on reported uncertainties in McCarthy et al. (2015). We use the years 2005-2021, which are all complete calendar years available from the RAPID data set.

The Southern Ocean sea surface salinity is reported for the subpolar seasonally stratified biome (SPSS, averaged on the native model mesh by the model providers) and for the area covering both the SPSS and STSS (subtropical seasonally stratified biome) biomes with the latter being calculated from 1°x1° gridded model sea surface salinity fields. Biome definitions are taken from Fay and McKinley (2014, as provided for the RECCAP project). The averages over the SPSS biome were checked for consistency with the gridded fields. The sea surface salinity was first used as an emergent constraint for the Southern Ocean CO₂ uptake by Earth System Models (Terhaar et al. 2021, 2022) using the interfrontal salinity between the polar and subtropical fronts with dynamic fronts. As the GOBMs are forced with reanalysis data, the fronts do not vary as much as in the ESMs, and thus the use of fixed biomes is justified (Hauck et al., in review, Terhaar et al., in review). We use the time period 2005-2021 for consistency with the AMOC metric. The observational sea surface salinity values are calculated from the EN4 data set (Good et al., 2013; using the objective analyses – Gouretski and Reseghetti (2010) XBT corrections and Gouretski and Cheng (2020) MBT corrections) with the aid of the Fay and McKinley (2014) mask.

The Southern Ocean stratification index is a simplified version of the metric used in Bourgeois et al. (2022). It is defined as the difference between in situ density at the surface and at 1000 m depth in the latitudinal band of 30°S to 55°S. Each model provider calculated this metric based on their native model mesh. We use again the period of 2005-2021 for consistency with the AMOC metric. The same metric was calculated from the EN4 data set mentioned above (Good et al., 2013).

Finally, the global surface ocean Revelle factor is reported. Monthly 1°x1° gridded fields were provided by the modelling groups, based on standard carbonate chemistry routines (e.g., mocsy, Orr & Epitalon, 2015;

PyCO2SYS, Humphreys et al., 2022a,b). The observational metrics come from two sources, firstly the gridded GLODAP data set v2.2016 (Lauvset et al., 2016), which is a climatology centered around the year 2002. For comparison with GLODAP, the models were subsampled to GLODAP data coverage and to a comparable time window also centred around 2002 (1997-2007). Secondly, the OceanSODA_v2023 data set (Gregor and Gruber, 2020, updated) was used, which has all input data available to calculate the surface ocean Revelle factor. OceanSODA covers a slightly smaller surface area (~96 % of GLODAP), but provides data until 2022. Again, for consistency with the other metrics, the period 2005-2021 was used and the models were subsampled to the same spatial and temporal coverage..

For this release, only the comparison of the metrics between GOBMs and observational data sets is presented, whereas it is foreseen to translate this comparison into a quantitative benchmarking comparable to the iLAMB benchmarking for the DGVMs and the corresponding iOMB framework (Ogunro et al., 2018). In a next step, model weighting can be applied based on the benchmarking (e.g., Brunner et al., 2020).

S3.4 Uncertainty assessment for S_{OCEAN}

We quantify the 1- σ uncertainty around the mean ocean sink of anthropogenic CO_2 by assessing random and systematic uncertainties for the GOBMs and fCO_2 -products. The random uncertainties are taken from the ensemble standard deviation (0.3 GtC yr⁻¹ for GOBMs, 0.3 GtC yr⁻¹ for fCO_2 -products). We derive the GOBMs systematic uncertainty by the deviation of the DIC inventory change 1994-2007 from the Gruber et al (2019) estimate (0.4 GtC yr⁻¹) and suggest these are related to physical transport (mixing, advection) into the ocean interior. For the fCO_2 -products, we consider systematic uncertainties stemming from uncertainty in fCO_2 observations (0.2 GtC yr⁻¹, Takahashi et al., 2009; Wanninkhof et al., 2013), gas-transfer velocity (0.2 GtC yr⁻¹, Ho et al., 2011; Wanninkhof et al., 2013; Roobaert et al., 2018), wind product (0.1 GtC yr⁻¹, Fay et al., 2021), river flux adjustment (0.3 GtC yr⁻¹, Regnier et al., 2022, formally 2- σ uncertainty), and fCO_2 mapping (0.2 GtC yr⁻¹, Landschützer et al., 2014). Combining these uncertainties as their squared sums, we assign an uncertainty of ± 0.5 GtC yr⁻¹ to the GOBMs ensemble mean and an uncertainty of ± 0.6 GtC yr⁻¹ to the fCO_2 -product ensemble mean. These uncertainties are propagated as $\sigma(S_{OCEAN}) = (1/2^2 * 0.5^2 + 1/2^2 * 0.6^2)^{1/2}$ GtC yr⁻¹ and result in an ± 0.4 GtC yr⁻¹ uncertainty around the best estimate of S_{OCEAN} .

We examine the consistency between the variability of the GOBMs and the fCO_2 -products to assess confidence in S_{OCEAN} . The interannual variability of the ocean fluxes (quantified as A-IAV, the standard deviation after detrending, Figure S2) of the seven fCO_2 -products plus the Watson et al. (2020) product for 1990-2022, ranges from 0.10 to 0.31 GtC yr⁻¹ with the lower estimates by the three ensemble methods (NIES-ML3, CMEMS-LSCE-FFNN, OS-ETHZ-GRaCER). The inter-annual variability in the GOBMs ranges between 0.11 and 0.20 GtC yr⁻¹, hence there is overlap with the lower A-IAV estimates of three fCO_2 -products.

Individual estimates (both GOBMs and fCO_2 -products) generally produce a higher ocean CO_2 sink during strong El Niño events. There is emerging agreement between GOBMs and fCO_2 -products on the patterns of decadal variability of S_{OCEAN} with a global stagnation in the 1990s and an extra-tropical strengthening in the 2000s (McKinley et al., 2020, Hauck et al., 2020) and also on the stagnation or decline of S_{OCEAN} in the triple La Niña

years 2020-2023. The central estimates of the annual flux from the GOBMs and the $f\text{CO}_2$ -products have a correlation r of 0.96 (1990-2022). The agreement between the models and the $f\text{CO}_2$ products reflects some consistency in their representation of underlying variability since there is little overlap in their methodology or use of observations.

S.4 Methodology Land CO₂ sink

S.4.1 DGVM simulations

The DGVMs model runs were forced by either the merged monthly Climate Research Unit (CRU) and 6 hourly Japanese 55-year Reanalysis (JRA-55) data set or by the monthly CRU data set, both providing observation-based temperature, precipitation, and incoming surface radiation on a $0.5^\circ \times 0.5^\circ$ grid and updated to 2021 (Harris et al., 2014, 2020). The combination of CRU monthly data with 6 hourly forcing from JRA-55 (Kobayashi et al., 2015) is performed with methodology used in previous years (Viovy, 2016) adapted to the specifics of the JRA-55 data.

Introduced in GCB2021 (Friedlingstein et al., 2022a), incoming short-wave radiation fields take into account aerosol impacts and the division of total radiation into direct and diffuse components as summarised below.

The diffuse fraction dataset offers 6-hourly distributions of the diffuse fraction of surface shortwave fluxes over the period 1901-2022. Radiative transfer calculations are based on monthly-averaged distributions of tropospheric and stratospheric aerosol optical depth, and 6-hourly distributions of cloud fraction. Methods follow those described in the Methods section of Mercado et al. (2009), but with updated input datasets.

The time series of speciated tropospheric aerosol optical depth is taken from the historical and RCP8.5 simulations by the HadGEM2-ES climate model (Bellouin et al., 2011). To correct for biases in HadGEM2-ES, tropospheric aerosol optical depths are scaled over the whole period to match the global and monthly averages obtained over the period 2003-2020 by the CAMS Reanalysis of atmospheric composition (Inness et al., 2019), which assimilates satellite retrievals of aerosol optical depth.

The time series of stratospheric aerosol optical depth is taken from the by Sato et al. (1993) climatology, which has been updated to 2012. Years 2013-2020 are assumed to be background years so replicate the background year 2010. That assumption is supported by the Global Space-based Stratospheric Aerosol Climatology time series (1979-2016; Thomason et al., 2018). The time series of cloud fraction is obtained by scaling the 6-hourly distributions simulated in the Japanese Reanalysis (Kobayashi et al., 2015) to match the monthly-averaged cloud cover in the CRU TS v4.06 dataset (Harris et al., 2020). Surface radiative fluxes account for aerosol-radiation interactions from both tropospheric and stratospheric aerosols, and for aerosol-cloud interactions from tropospheric aerosols, except mineral dust. Tropospheric aerosols are also assumed to exert interactions with clouds.

The radiative effects of those aerosol-cloud interactions are assumed to scale with the radiative effects of aerosol-radiation interactions of tropospheric aerosols, using regional scaling factors derived from HadGEM2-ES. Diffuse fraction is assumed to be 1 in cloudy sky. Atmospheric constituents other than aerosols and clouds are set to a constant standard mid-latitude summer atmosphere, but their variations do not affect the diffuse fraction of surface shortwave fluxes.

In summary, the DGVMs forcing data include time dependent gridded climate forcing, global atmospheric CO₂ (Lan et al. (2023)), gridded land cover changes (see Supplement S.2.2), and gridded nitrogen deposition and fertilisers (see Table S1 for specific models details).

Four simulations were performed with each of the DGVMs. Simulation 0 (S0) is a control simulation which uses fixed pre-industrial (year 1700) atmospheric CO₂ concentrations, cycles early 20th century (1901-1920) climate and applies a time-invariant pre-industrial land cover distribution and pre-industrial wood harvest rates. Simulation 1 (S1) differs from S0 by applying historical changes in atmospheric CO₂ concentration and N inputs. Simulation 2 (S2) applies historical changes in atmospheric CO₂ concentration, N inputs, and climate, while applying time-invariant pre-industrial land cover distribution and pre-industrial wood harvest rates. Simulation 3 (S3) applies historical changes in atmospheric CO₂ concentration, N inputs, climate, and land cover distribution and wood harvest rates. S2 is used to estimate the land sink component of the global carbon budget (S_{LAND}). S3 is used to estimate the total land flux but is not used in the global carbon budget. We further separate S_{LAND} into contributions from CO₂ ($=S1-S0$) and climate ($=S2-S1+S0$).

S.4.2 DGVM evaluation and uncertainty assessment for S_{LAND} and net land flux

We apply three criteria for minimum DGVMs realism by including only those DGVMs with (1) steady state after spin up, (2) global net land flux ($S_{\text{LAND}} - E_{\text{LUC}}$) that is an atmosphere-to-land carbon flux over the 1990s ranging between -0.3 and 2.3 GtC yr⁻¹, within 90% confidence of constraints by global atmospheric and oceanic observations (Keeling and Manning, 2014; Wanninkhof et al., 2013), and (3) global E_{LUC} that is a carbon source to the atmosphere over the 1990s, as already mentioned in Supplement S.2.2. All DGVMs meet these three criteria.

In addition, the DGVMs results are also evaluated using the International Land Model Benchmarking system (ILAMB; Collier et al., 2018). This evaluation is provided here to document, encourage and support model improvements through time. ILAMB variables cover key processes that are relevant for the quantification of S_{LAND} and resulting aggregated outcomes. The selected variables are vegetation biomass, gross primary productivity, leaf area index, net ecosystem exchange, ecosystem respiration, evapotranspiration, soil carbon, runoff, and relationships between carbon cycle variables, precipitation (Adler et al., 2003) and temperature (Harris et al., 2014) (see Figure S3 for the results and for the list of observed databases). Results are shown in Figure S3 and briefly discussed in Section 3.7.5.

For the uncertainty for S_{LAND} , we use the standard deviation of the annual CO₂ sink across the DGVMs, averaging to about ± 0.6 GtC yr⁻¹ for the period 1959 to 2021. We attach a medium confidence level to the annual land CO₂ sink and its uncertainty because the estimates from the residual budget and averaged DGVMs match well within their respective uncertainties (Table 5).

S.5 Methodology Atmospheric Inversions

S.5.1 Inversion System Simulations

Fourteen atmospheric inversions (details of each in Table S4) were used to infer the spatio-temporal distribution of the CO₂ flux exchanged between the atmosphere and the land or oceans. These inversions are based on Bayesian inversion principles with prior information on fluxes and their uncertainties. They use very similar sets

of surface measurements of CO₂ time series (or subsets thereof) from various flask and in situ networks. Six inversion systems used satellite xCO₂ retrievals from GOSAT and OCO-2, of which two systems used a combination of satellite and surface observations.

Each inversion system uses different methodologies and input data but is rooted in Bayesian inversion principles. These differences mainly concern the selection of atmospheric CO₂ data and prior fluxes, as well as the spatial resolution, assumed correlation structures, and mathematical approach of the models. Each system uses a different transport model, which was demonstrated to be a driving factor behind differences in atmospheric inversion-based flux estimates, and specifically their distribution across latitudinal bands (Gaubert et al., 2019; Schuh et al., 2019).

Most of the fourteen inversion systems prescribe similar global fossil fuel emissions for E_{FOS}; specifically, the GCP's Gridded Fossil Emissions Dataset version 2023.1 (GCP-GridFEDv2023.1; Jones et al., 2023), which is an update through 2022 of the first version of GCP-GridFED presented by Jones et al. (2021b) (Table S4). All GCP-GridFED versions scale gridded estimates of CO₂ emissions from EDGARv4.3.2 (Janssens-Maenhout et al., 2019) within national territories to match national emissions estimates provided by the GCP for the years 1959-2022, which are compiled following the methodology described in Supplement S.1. GCP-GridFEDv2023.1 adopts the seasonality of emissions (the monthly distribution of annual emissions) from the Carbon Monitor (Liu et al., 2020a,b; Dou et al., 2022) for Brazil, China, all EU27 countries, the United Kingdom, the USA and shipping and aviation bunker emissions. The seasonality present in Carbon Monitor is used directly for years 2019-2022, while for years 1959-2018 the average seasonality of 2019, and 2021 and 2022 are applied (avoiding the year 2020 during which emissions were most impacted by the COVID-19 pandemic). For all other countries, seasonality of emissions is taken from EDGAR (Janssens-Maenhout et al., 2019; Jones et al., 2023), with small annual correction to the seasonality present in 2010 based on heating or cooling degree days to account for the effects of inter-annual climate variability on the seasonality of emissions (Jones et al., 2021b).

Small remaining differences between regridding of the GridFED inputs, or the use of different fossil fuel emission priors are corrected for by scaling the resulting inverse fluxes to GridFEDv2023.1. The consistent use of E_{FOS} ensures a close alignment with the estimate of E_{FOS} used in this budget assessment, enhancing the comparability of the inversion-based estimate with the flux estimates deriving from DGVMs, GOBMs and fCO₂-based methods. The fossil fuel adjustment (including emissions from cement production and cement carbonation CO₂ sink) ensures that the estimated uptake of atmospheric CO₂ by the land and oceans was fully consistent within the inversion ensemble.

The land and ocean CO₂ fluxes from atmospheric inversions contain anthropogenic perturbation and natural pre-industrial CO₂ fluxes. On annual time scales, natural pre-industrial fluxes are primarily land CO₂ sinks and ocean CO₂ sources corresponding to carbon taken up on land, transported by rivers from land to ocean, and outgassed by the ocean. These pre-industrial land CO₂ sinks are thus compensated over the globe by ocean CO₂ sources corresponding to the outgassing of riverine carbon inputs to the ocean, using the exact same numbers and distribution as described for the oceans in Section 2.5. To facilitate the comparison, we adjusted the inverse estimates of the land and ocean fluxes per latitude band with these numbers to produce historical perturbation CO₂ fluxes from inversions.

S.5.2 Inversion System Evaluation

All participating atmospheric inversions are checked for consistency with the annual global growth rate, as both are derived from the global surface network of atmospheric CO₂ observations. In this exercise, we use the conversion factor of 2.086 GtC/ppm to convert the inverted carbon fluxes to mole fractions, as suggested by Prather (2012). This number is specifically suited for the comparison to surface observations that do not respond uniformly, nor immediately, to each year's summed sources and sinks. This factor is therefore slightly smaller than the GCB conversion factor in Table 1 (2.142 GtC/ppm, Ballantyne et al., 2012). Overall, the inversions agree with the growth rate with biases between 0.002-0.041 ppm yr⁻¹ (0.005-0.09 GtCyr⁻¹) for the period 2015-2022, except for MIROC4-ACTM, which has a larger bias at 0.09 ppm yr⁻¹.

The atmospheric inversions are also evaluated using vertical profiles of atmospheric CO₂ concentrations (Figure S4). More than 30 aircraft programs over the globe, either regular programs or repeated surveys over at least 9 months (except on the SH), have been used in order to draw a robust picture of the system performance (with space-time data coverage irregular and denser in the 0-45°N latitude band; Table S6 and lower panel in Figure S4). The fourteen systems are compared to these independent aircraft CO₂ observations between 2 and 7 km above sea level between 2001 and 2022. Results are shown in Figure S4, where the inversions generally match the atmospheric mole fractions to within 0.7 ppm at all latitudes, except for MIROC4-ACTM in the Northern Hemisphere in the 2015-2022 period. Based on this larger bias with also larger standard deviations, plus the larger bias for the growth rate, the results for MIROC4-ACTM are not included in the statistics of the inversion ensemble.

S.6 Processes not included in the global carbon budget

S.6.1 Contribution of anthropogenic CO and CH₄ to the global carbon budget

Equation (1) includes only partly the net input of CO₂ to the atmosphere from the chemical oxidation of reactive carbon-containing gases from sources other than the combustion of fossil fuels, such as: (1) cement process emissions, since these do not come from combustion of fossil fuels, (2) the oxidation of fossil fuels, (3) the assumption of immediate oxidation of vented methane in oil production. However, it omits any other anthropogenic carbon-containing gases that are eventually oxidised in the atmosphere, forming a diffuse source of CO₂, such as anthropogenic emissions of CO and CH₄. An attempt is made in this section to estimate their magnitude and identify the sources of uncertainty. Anthropogenic CO emissions are from incomplete fossil fuel and biofuel burning and deforestation fires. The main anthropogenic emissions of fossil CH₄ that matter for the global (anthropogenic) carbon budget are the fugitive emissions of coal, oil and gas sectors (see below). These emissions of CO and CH₄ contribute a net addition of fossil carbon to the atmosphere.

In our estimate of E_{FOS} we assumed (Section 2.1.1) that all the fuel burned is emitted as CO₂, thus CO anthropogenic emissions associated with incomplete fossil fuel combustion and its atmospheric oxidation into CO₂ within a few months are already counted implicitly in E_{FOS} and should not be counted twice (same for E_{LUC} and anthropogenic CO emissions by deforestation fires). The diffuse atmospheric source of CO₂ deriving from anthropogenic emissions of fossil CH₄ is not included in E_{FOS}. In reality, the diffuse source of CO₂ from CH₄ oxidation contributes to the annual CO₂ growth. Emissions of fossil CH₄ represent 30% of total anthropogenic CH₄ emissions (Saunio et al. 2020; their top-down estimate is used because it is consistent with the observed CH₄ growth rate), that is 0.083 GtC yr⁻¹ for the decade 2008-2017. Assuming steady state, an amount equal to

this fossil CH₄ emission is all converted to CO₂ by OH oxidation, and thus explain 0.083 GtC yr⁻¹ of the global CO₂ growth rate with an uncertainty range of 0.061 to 0.098 GtC yr⁻¹ taken from the min-max of top-down estimates in Saunio et al. (2020). If this min-max range is assumed to be 2 σ because Saunio et al. (2020) did not account for the internal uncertainty of their min and max top-down estimates, it translates into a 1- σ uncertainty of 0.019 GtC yr⁻¹.

Other anthropogenic changes in the sources of CO and CH₄ from wildfires, vegetation biomass, wetlands, ruminants, or permafrost changes are similarly assumed to have a small effect on the CO₂ growth rate. The CH₄ and CO emissions and sinks are published and analysed separately in the Global Methane Budget and Global Carbon Monoxide Budget publications, which follow a similar approach to that presented here (Saunio et al., 2020; Zheng et al., 2019).

S.6.2 Contribution of other carbonates to CO₂ emissions

Although we do account for cement carbonation (a carbon sink), the contribution of emissions of fossil carbonates (carbon sources) other than cement production is not systematically included in estimates of E_{FOS}, except for Annex I countries and lime production in China (Andrew and Peters, 2021). The missing processes include CO₂ emissions associated with the calcination of lime and limestone outside of cement production. Carbonates are also used in various industries, including in iron and steel manufacture and in agriculture. They are found naturally in some coals. CO₂ emissions from fossil carbonates other than cement not included in our dataset are estimated to amount to about 0.3% of E_{FOS} (estimated based on Crippa et al., 2019).

S.6.3 Anthropogenic carbon fluxes in the land-to-ocean aquatic continuum

The approach used to determine the global carbon budget refers to the mean, variations, and trends in the perturbation of CO₂ in the atmosphere, referenced to the pre-industrial era. Carbon is continuously displaced from the land to the ocean through the land-ocean aquatic continuum (LOAC) comprising freshwaters, estuaries, and coastal areas (Bauer et al., 2013; Regnier et al., 2013). A substantial fraction of this lateral carbon flux is entirely ‘natural’ and is thus a steady state component of the pre-industrial carbon cycle. We account for this pre-industrial flux where appropriate in our study (see Supplement S.3). However, changes in environmental conditions and land-use change have caused an increase in the lateral transport of carbon into the LOAC – a perturbation that is relevant for the global carbon budget presented here.

The results of the analysis of Regnier et al. (2013) can be summarised in two points of relevance for the anthropogenic CO₂ budget. First, the anthropogenic perturbation of the LOAC has increased the organic carbon export from terrestrial ecosystems to the hydrosphere by as much as 1.0 ± 0.5 GtC yr⁻¹ since pre-industrial times, mainly owing to enhanced carbon export from soils. Second, this exported anthropogenic carbon is partly respired through the LOAC, partly sequestered in sediments along the LOAC and to a lesser extent, transferred to the open ocean where it may accumulate or be outgassed. The increase in storage of land-derived organic carbon in the LOAC carbon reservoirs (burial) and in the open ocean combined is estimated by Regnier et al. (2013) at 0.65 ± 0.35 GtC yr⁻¹. The inclusion of LOAC related anthropogenic CO₂ fluxes should affect estimates of S_{LAND} and S_{OCEAN} in Eq. (1) but does not affect the other terms. Representation of the anthropogenic perturbation of LOAC CO₂ fluxes is however not included in the GOBMs and DGVMs used in our global carbon budget analysis presented here.

S.6.4 Loss of additional land sink capacity

Historical land-cover change was dominated by transitions from vegetation types that can provide a large carbon sink per area unit (typically, forests) to others less efficient in removing CO₂ from the atmosphere (typically, croplands). The resultant decrease in land sink, called the ‘loss of additional sink capacity’, can be calculated as the difference between the actual land sink under changing land-cover and the counterfactual land sink under pre-industrial land-cover. This term is not accounted for in our global carbon budget estimate. Here, we provide a quantitative estimate of this term to be used in the discussion. Seven of the DGVMs used in Friedlingstein et al. (2019) performed additional simulations with and without land-use change under cycled pre-industrial environmental conditions. The resulting loss of additional sink capacity amounts to 0.9 ± 0.3 GtC yr⁻¹ on average over 2009-2018 and 42 ± 16 GtC accumulated between 1850 and 2018 (Obermeier et al., 2021). OSCAR, emulating the behaviour of 11 DGVMs finds values of the loss of additional sink capacity of 0.7 ± 0.6 GtC yr⁻¹ and 31 ± 23 GtC for the same time period (Gasser et al., 2020). Since the DGVM-based ELUC estimates are only used to quantify the uncertainty around the bookkeeping models' ELUC, we do not add the loss of additional sink capacity to the bookkeeping estimate.

Table S1. Comparison of the processes included in the bookkeeping method and DGVMs in their estimates of ELUC and SLAND. See Table 4 for model references. All models include deforestation and forest regrowth after abandonment of agriculture (or from afforestation activities on agricultural land). Processes relevant for ELUC are only described for the DGVMs used with land-cover change in this study.

	Bookkeeping Models			DGVMs																					
	H&C2023	BLUE	OSCAR	CABLE-POP	CLASIS	CLM5.0	DL-EM	EDv3	ELM	IBIS	ISAM	ISBA-CTRIP	JSBA-CH	JULES-ES	LPJ-GU-ESS	LPJml	LPJwsl	LPX-Berlin	OCNv2	ORCHIDEv3	SDGVM	VISIT	YIBs	CARDAMOM	
Processes relevant for ELUC																									
Wood harvest and forest degradation (a)	yes	yes	yes	yes	no	yes	yes		yes	yes	yes	yes	no	yes	no	yes	no	yes	no (d)	yes	yes	yes	yes	no	yes (R+L)
Shifting cultivation / Subgrid scale transitions	yes (b)	yes	yes	yes	no	yes	no			yes	no		yes	no	yes		yes	no (d)	no	no	yes	yes	no		no
Cropland harvest (removed, R, or added to litter, L)	yes (R) (j)	yes (R) (j)	yes (R)	yes (R)	yes (L)	yes (R)	yes	yes (R+L)	yes (L)	yes (R)	yes	yes (R)	yes (R+L)	yes (R)	yes (R)	yes (R+L)	yes (L)	yes (R)	yes (R+L)	yes (R)	yes (R)	yes (R)	yes (R)	yes (L)	no
Peat fires	yes	yes	yes	no	no	yes	no	no	no	no	no	yes	no	no	no	no	no	no	no	no	no	no	no	no	yes (k)
fire as a management tool	yes (j)	yes (j)	yes (h)	no	no	no	no	no	no	no	no	no	no	no	no	no	no	no	no	no	no	no	no	no	yes (k)
N fertilisation	yes (j)	yes (j)	yes (h)	no	no	yes	yes	no	no	yes	yes	no	no	yes (i)	yes	yes	no	yes	yes	yes	yes	no	no	no	no
tillage	yes (j)	yes (j)	yes (h)	no	yes (g)	no	no	no	no	no	no	no	no	no	yes	yes	no	no	no	yes (g)	no	no	no	no	no
irrigation	yes (j)	yes (j)	yes (h)	no	no	yes	yes	no	no	no	yes	no	no	no	yes	yes	no	no	no	no	no	no	no	no	no
wetland drainage	yes (j)	yes (j)	yes (h)	no	no	no	no	no	no	no	yes	no	no	no	no	no	no	no	no	no	no	no	no	no	no
erosion	yes (j)	yes (j)	yes (h)	no	no	no	yes	no	no	no	no	no	no	no	no	no	no	no	no	no	no	yes	no	no	no
peat drainage	yes	yes	yes	no	no	no	no	no	no	no	no	no	no	no	no	no	no	no	no	no	no	no	no	no	no
Grazing and mowing Harvest (removed, r, or added to litter, l)	yes (r) (j)	yes (r) (j)	yes (r)	yes (r)	no	no	no	yes (r+l)		no	yes (r, l)		yes (l)	no	yes (r)	yes (r+l)	yes (l)	no	yes (r+l)		no	no	no	no	no
Processes also relevant for SLAND (in addition to CO2 fertilisation and climate)																									
ecosystem demography / vegetation competition, ie dynamic fractional area of natural vegetation				yes (demography but no competition)					yes					No ED. Yes VC.	yes		yes					yes		no	

Fire simulation and/or suppression	N. A.	N. A.	N. A.	no	yes	yes	no	yes	yes	yes	no	yes	yes	yes	yes	yes	yes	yes	no	no	yes	yes	no	yes (k)
Carbon-nitrogen interactions, including N deposition	N. A.	N. A.	N. A.	yes	no (f)	yes	yes	no	yes	yes	yes	no	yes	yes	yes	yes	no	yes	yes	yes	yes (c)	no	no (f)	no
Separate treatment of direct and diffuse solar radiation	N. A.	N. A.	N. A.	yes	no	yes	no	no	yes	yes	no	no	no	yes	no	no	no	no	no	no	no	no	yes	no

(a) Refers to the routine harvest of established managed forests rather than pools of harvested products.

(b) No back- and forth-transitions between vegetation types at the country-level, but if forest loss based on FRA exceeded agricultural expansion based on FAO, then this amount of area was cleared for cropland and the same amount of area of old croplands abandoned.

(c) Limited. Nitrogen uptake is simulated as a function of soil C, and Vcmax is an empirical function of canopy N. Does not consider N deposition.

(d) Available but not active.

(e) Simple parameterization of nitrogen limitation based on Yin (2002; assessed on FACE experiments)

(f) Although C-N cycle interactions are not represented, the model includes a parameterization of down-regulation of photosynthesis as CO₂ increases to emulate nutrient constraints (Arora et al., 2009)

(g) Tillage is represented over croplands by increased soil carbon decomposition rate and reduced humification of litter to soil carbon.

(h) as far as the DGVMs that OSCAR is calibrated to include it

(i) perfect fertilisation assumed, i.e. crops are not nitrogen limited and the implied fertiliser diagnosed

(j) Process captured implicitly by use of observed carbon densities.

(k) Fire imposed based on EO burned area

880
881
882

Table S2. Comparison of the processes and model set up for the Global Ocean Biogeochemistry Models for their estimates of SOCEAN. See Table 4 for model references.

	NEMO-PlankTOM12	NEMO-PISCES (IPSL)	MICOM-HAMOC (NorESM1-OCv1.2)	MPIOM-HAMOC6	FESOM-2.1-REcoM3	NEMO3.6-PISCESv2-gas (CNRM)	MOM6-COBALT (Princeton)	CESM-ETHZ	MRI-ESM2-2	ACCESS (CSIRO)
Model specifics										
Physical ocean model	NEMOv3.6-ORCA2	NEMOv3.6-eORCA1L75	MICOM (NorESM1-OCv1.2)	MPIOM	FESOM-2.1	NEMOv3.6-GELATOv6-eORCA1L75	MOM6-SIS2	CESMv1.3 (ocean model based on POP2)	MRI.COMv5	MOM5
Biogeochemistry model	PlankTOM12	PISCESv2	HAMOC (NorESM1-OCv1.2)	HAMOC6	REcoM-3	PISCESv2-gas	COBALTv2	BEC (modified & extended)	NPZD	WOMBAT
Horizontal resolution	2° lon, 0.3 to 1.5° lat	1° lon, 0.3 to 1° lat	1° lon, 0.17 to 0.25 lat	1.5°	unstructured mesh, 20-120 km resolution (CORE mesh)	1° lon, 0.3 to 1° lat	0.5° lon, 0.25 to 0.5° lat	1.125° lon, 0.53° to 0.27° lat	1° lon, 0.3 to 0.5° lat	1°x1° with enhanced latitudinal resolution in the tropics and high-lat Southern Ocean
Vertical resolution	31 levels	75 levels, 1m at the surface	51 isopycnic layers + 2 layers representing a bulk mixed layer	40 levels	46 levels, 10 m spacing in the top 100 m	75 levels, 1m at surface	75 levels hybrid coordinates, 2m at surface	60 levels	60 levels with 1-level bottom boundary layer	50 levels, 20 in the top 200m
Total ocean area on native grid (km ²)	3.6080E+08	3.6270E+08	3.6006E+08	3.6598E+08	3.6435E+08	3.6270E+14	3.6111E+08	3.5926E+08	3.6096E+08	3.6134E+08
Gas-exchange parameterization	Wanninkhof et al. (1992)	Orr et al. (2017)	Orr et al. (2017), but with a=0.337	Orr et al. (2017)	Orr et al. (2017)	Orr et al. (2017); Wanninkhof et al. (2014)	Orr et al. (2017)	Wanninkhof (1992, coefficient a scaled down to 0.31)	Orr et al. (2017)	Wanninkhof et al. (1992)
CO ₂ chemistry routines	OCMIP2 (Orr et al. 2017)	mocsy	Following Dickson et al. (2007)	Ilyina et al. (2013) adapted to comply with OMIP protocol (Orr et al. (2017))	mocsy	mocsy	mocsy	OCMIP2 (Orr et al., 2017)	mocsy	OCMIP2 (Orr et al., 2017)
River input (PgC/yr) (organic/inorganic DIC)	0.723 / -	0.61 / -	0	0.77 / -	0 / 0	0.611 / -	~0.07 / ~0.15	0.33 / -	0 / 0	0/0
Net flux to sediment (PgC/yr) (organic/other)	0.723 / -	0.59 / -	around 0.54 / -	- / 0.44	0 / 0	around 0.656 / -	~0.11 / ~0.07 (CaCO ₃)	0.21 / -	0 / 0	0/0
SPIN-UP procedure										
Initialisation of carbon chemistry	GLODAPv1 (preindustrial DIC)	GLODAPv2 (preindustrial DIC)	GLODAPv1 (preindustrial DIC)	initialization from previous simulation	GLODAPv2 (preindustrial DIC)	GLODAPv2	GLODAPv2 (Alkalinity, DIC) corrected to 1959 level (simulation A and C) and to pre-industrial level (simulation)	GLODAPv2 (preindustrial DIC)	GLODAPv2 (preindustrial DIC)	GLODAPv1 preindustrial DIC

							B and D) using Khatiwala et al. (2009)			
Preindustrial spin-up prior to 1850	spin-up 1750-1940	spin-up starting in 1836 with 3 loops of JRA55	1000 year spin up (prior to 1762)	~2000 years	189 years	long spin-up (> 1000 years)	Other bgc tracers initialized from a GFDL-ESM2M spin-up (> 1000 years)	spinup 1655-1849, with xCO2 = 278	1661 years with xCO2 = 278	1000+ years
Atmospheric forcing fields and CO2										
Atmospheric forcing for (i) pre-industrial spin-up, (ii) spin-up 1850-1958 for simulation B, (iii) simulation B	looping ERA5 year 1990 (i, ii, iii)	(i) and (ii) looping full JRA55-do-v1.4 reanalysis from 1836 to 1958, and (iii) looping first ten years (1958-1967) of JRA55-do-v1.4 for simulation B.	CORE-I (normal year) forcing (i, ii, iii)	OMIP climatology (i), NCEP year 1957 (ii,iii)	JRA55-do v.1.5.0 repeated year 1961 (i, ii, iii)	JRA55-do-v1.5.0 full reanalysis (i) cycling year 1958 (ii,iii)	GFDL-ESM2M internal forcing (i), JRA55-do-v1.5.0 repeat year 1959 (ii,iii)	COREv2 until 1837, from 1837-1850: JRA (1958-1971) (ii,iii) JRA cyclical	JRA55-do v1.5.0 repeat year 1990/91 (i, ii, iii)	(i) 800+ years CORE spinup. 250 years with JRA55-do and another 300 years JRA55-do and 278ppm CO2, (ii) and (iii) JRA55-do, 1990/1991 repeat year forcing
Atmospheric CO2 for control spin-up 1850-1958 for simulation B, and for simulation B	constant 278ppm; converted to pCO2 temperature formulation (Sarmiento et al., 1992)	xCO2 of 286.46ppm, converted to pCO2 with constant sea-level pressure and water vapour pressure	xCO2 of 278ppm, converted to pCO2 with sea-level pressure and water vapour pressure	xCO2 of 278ppm, no conversion to pCO2	xCO2 of 278ppm, converted to pCO2 with sea-level pressure and water vapour pressure	xCO2 of 286.46ppm, converted to pCO2 with constant sea-level pressure and water vapour pressure	xCO2 of 278ppm, converted to pCO2 with sea-level pressure and water vapour pressure	xCO2 = 278 ppm, converted to pCO2 with atmospheric pressure, and water vapour pressure	xCO2 of 278ppm, converted to pCO2 with water vapour and sea-level pressure (JRA55-do repeat year 1990/91)	xCO2 of 278ppm, converted to pCO2 with sea-level pressure
Atmospheric forcing for historical spin-up 1850-1958 for simulation A (i) and for simulation A (ii)	1750-1940: looping ERA5 year 1990; 1940-2022: ERA5	1836-1958 : looping full JRA55 reanalysis (i), JRA55-do-v1.4 then 1.5 for 2020-22 (ii)	CORE-I (normal year) forcing; from 1948 onwards NCEP-R1 with CORE-II corrections	NCEP 6 hourly cyclic forcing (10 years starting from 1948, i), 1948-2022: transient NCEP forcing	JRA55-do-v1.5.0 repeated year 1961 (i), transient JRA55-do-v1.5.0 (1958-2021), v1.5.0.1 (2022,ii)	JRA55-do cycling year 1958 (i), JRA55-do-v1.5.0 (ii)	JRA55-do-v1.5 repeat year 1959 (i), v1.5.0 (1959-2019, v1.5.0.1b (2020), v1.5.0.1 (2021-2022; ii)	JRA55 version 1.3, repeat cycle between 1958-2018 (i), v1.3 (1959-2018), v1.5.0.1 (2020-2022)	1653-1957: repeated cycle JRA55-do v1.5.0 (1958-2018 (i), v1.5.0.1 (2019-2022; ii)	(i) JRA55-do, 1990/1991 repeat year forcing, (ii) JRA55-do v1.5.0 for 1958-2019, and v1.5.0.1 for 2020-2023.
Atmospheric CO2 for historical spin-up 1850-1958 for simulation A (i) and simulation A (ii)	xCO2 provided by the GCB; converted to pCO2 temperature formulation (Sarmiento et al., 1992), monthly resolution (i, ii)	xCO2 as provided by the GCB, global mean, annual resolution, converted to pCO2 with sea-level pressure and water vapour pressure (i, ii)	xCO2 as provided by the GCB, converted to pCO2 with sea level pressure (taken from the atmospheric forcing) and water vapor correction (i, ii)	transient monthly xCO2 provided by GCB, no conversion (i, ii)	xCO2 as provided by the GCB, converted to pCO2 with sea-level pressure and water vapour pressure, global mean, monthly resolution (i, ii)	xCO2 as provided by the GCB, converted to pCO2 with constant sea-level pressure and water vapour pressure, global mean, yearly resolution (i, ii)	xCO2 at year 1959 level (i) and as provided by GCB (ii), both converted to pCO2 with sea-level pressure and water vapour pressure, global mean, yearly resolution	xCO2 as provided by the GCB, converted to pCO2 with locally determined atm. pressure, and water vapour pressure (i, ii)	xCO2 as provided by GCB, converted to pCO2 with water vapour and sea-level pressure (i, ii).	xCO2 as provided by the GCB, converted to pCO2 with sea-level pressure

Table S3: Description of ocean $f\text{CO}_2$ -products used for assessment of SOCEAN. See Table 4 for references.

	Jena-MLS	MPI-SOMFFN	CMEMS-LSCE-FFNN	UOEx-Watson	NIES-ML3	JMA-MLR	OS-ETHZ-GRaCER	LDEO HPD
Method	Spatio-temporal interpolation (version oc_v2023). Spatio-temporal field of ocean-internal carbon sources/sinks is fit to the SOCATv2022 pCO ₂ data. Includes a multi-linear regression against environmental drivers to bridge data gaps,	A feed-forward neural network (FFN) determines non-linear relationship between SOCAT pCO ₂ measurements and environmental predictor data for 16 biogeochemical provinces (defined through a self-organizing map, SOM) and is used to fill the existing data gaps.	An ensemble of neural network models trained on 100 subsampled datasets from SOCAT and environmental predictors. The models are used to reconstruct sea surface fugacity of CO ₂ and convert to air-sea CO ₂ fluxes	Modified MPI-SOMFFN with SOCATv2023 fCO ₂ database, corrected to the subskin temperature (ESA CCI v2.1) of the ocean as measured by satellites (Goddijn-Murphy et al., 2015). Flux calculation corrected for the cool and salty surface skin. Monthly skin temperature calculated from ESA CCI v2.1 (Merchant et al., 2019) with the cool skin difference calculated using NOAA COARE 3.5.	The ensemble of a random forest, a gradient boost machine, and a feed forward neural network trained on SOCAT 2023 fCO ₂ and environmental predictor data. The interannual trend of fCO ₂ was estimated first by the decadal trend of atmospheric CO ₂ and then corrected by a so-called leave-one-year-out validation method. The trend was used to normalize fCO ₂ to the reference year 2005 for model training and fCO ₂ prediction. The monthly fCO ₂ maps were reconstructed using the prediction and trend.	Fields of total alkalinity (TA) were estimated by using a multiple linear regressions (MLR) method based on GLODAPv2.2022 and satellite observation data. SOCATv2023 fCO ₂ data were converted to dissolved inorganic carbon (DIC) with the TA. Fields of DIC were estimated by using a MLR method based on the DIC and satellite observation data	Geospatial Random Cluster Ensemble Regression is a two-step cluster-regression approach, where multiple clustering instances with slight variations are run to create an ensemble of estimates. We use K-means clustering and a combination of Gradient boosted trees and Feed-forward neural-networks to estimate SOCAT v2023 fCO ₂ .	Based on fCO ₂ -misfit between observed fCO ₂ and eight Global Carbon Budget ocean biogeochemical models. The eXtreme Gradient Boosting method links this misfit to environmental observations to reconstruct the model misfit across all space and time., which is then added back to model-based fCO ₂ estimate. The final reconstruction of surface fCO ₂ is the average across the eight reconstructions. A climatology of the misfits calculated for the years 2000-2022 is used as an offset for years prior to 1982 when no/limited environmental observations are available to train the ML algorithm.
Gas-exchange parameterization	Wanninkhof (1992). Transfer coefficient k scaled to match a global mean transfer rate of 16.5 cm/hr by (Naegler, 2009)	Wanninkhof (1992). Transfer coefficient k scaled to match a global mean transfer rate of 16.5 cm/hr	Wanninkhof 2014. Transfer coefficient k scaled to match a global mean transfer rate of 16.5 cm/hr (Naegler, 2009)	Nightingale et al. (2000)	Wanninkhof (2014). Transfer coefficient k scaled to match a global mean transfer rate of 16.5 cm/hr (Naegler, 2009)	Wanninkhof (2014). Transfer coefficient k scaled to match a global mean transfer rate of 16.5 cm/hr (Naegler, 2009)	Wanninkhof (1992), averaged and scaled for three reanalysis wind data, to a global mean 16.5 cm/hr (after Naegler 2009; Fay & Gregor et al. 2021)	Transfer coefficient k scaled to match a global mean transfer rate of 16.5 cm/hr (Naegler, 2009)

Wind product	JMA55-do reanalysis	ERA 5	ERA5	CCMP3.0	ERA5	JRA55	JRA55, ERA5, NCEP1	ERA5
Spatial resolution	2.5 degrees longitude x 2 degrees latitude	1x1 degree	0.25x0.25 degree regridded to 1x1 degree	1x1 degree	1x1 degree	1x1 degree	1x1 degree	1x1 degree
Temporal resolution	daily	monthly	monthly	monthly	monthly	monthly	monthly	monthly
Atmospheric CO2	Spatially and temporally varying field based on atmospheric CO2 data from 169 stations (Jena CarboScope atmospheric inversion sEXTALL_v2021)	Spatially varying 1x1 degree atmospheric pCO2_wet calculated from the NOAA ESRL marine boundary layer xCO2 and NCEP sea level pressure with the moisture correction by Dickson et al. (2007).	Spatially and monthly varying fields of atmospheric pCO2 computed from CO2 mole fraction (CO2 atmospheric inversion from the Copernicus Atmosphere Monitoring Service), and atmospheric dry-air pressure which is derived from monthly surface pressure (ERA5) and water vapour pressure fitted by Weiss and Price (1980)	Atmospheric fCO2 (wet) calculated from NOAA marine boundary layer XCO2(atm) and ERA5 sea level pressure, with pH2O calculated from Cooper et al. (1998). 2022 XCO2 marine boundary values were not available at submission so we used preliminary values, estimated from 2021 values and increase at Mauna Loa.	NOAA Greenhouse Gas Marine Boundary Layer Reference. https://gml.noaa.gov/ccgg/mbbl/mbbl.html	Atmospheric xCO2 fields of JMA-GSAM inversion model (Maki et al. 2010; Nakamura et al. 2015) were converted to pCO2 by using JRA55 sea level pressure. 2022 xCO2 fields were not available at this stage, and we used Cape Grim and Mauna Loa xCO2 increments from 2021 to 2022 for the southern and northern hemispheres, respectively.	NOAA's marine boundary layer product for xCO2 is linearly interpolated onto a 1x1 degree grid and resampled from weekly to monthly. xCO2 is multiplied by ERA5 mean sea level pressure, where the latter corrected for water vapour pressure using Dickson et al. (2007). This results in monthly 1x1 degree pCO2atm.	Spatially varying 1x1 degree atmospheric pCO2_wet calculated from the NOAA ESRL marine boundary layer xCO2 and NCEP sea level pressure with the moisture correction by Dickson et al. (2007). NOAA GML xCO2 global monthly xCO2 is multiplied by ERA5 mean sea level pressure, where the latter corrected for water vapour pressure using Dickson et al. (2007). Earlier years (pre 1979) utilize NOAA GML xCO2 from Mauna Loa, corrected to a "global" value by calculating an offset between global and ML seasonal climatologic xCO2 values for common years (1979-2022).
Total ocean area on native grid (km2)	3.63E+08	3.63E+08	3.50E+08	3.48E+09	3.58E+08	3.10E+08 (2.98E+08 to 3.16E+08, depending on ice cover)	3.55E+08	3.61E+08
method to extend product to full global ocean coverage		Arctic and marginal seas added following Landschützer et				Fay et al. (2021)	Method has near full coverage	Fay et al. (2021). Gaps were filled with monthly

886

		al. (2020). No coastal cut.						climatology (Landschützer et al. 2020)with interannual variability added based on the temporal evolution of this product for all years.
--	--	-----------------------------	--	--	--	--	--	---

Table S4. Comparison of the inversion set up and input fields for the atmospheric inversions. Atmospheric inversions see the full CO₂ fluxes, including the anthropogenic and pre-industrial fluxes, hence they need to be adjusted for the pre-industrial flux of CO₂ from the land to the ocean that is part of the natural carbon cycle before they can be compared with SOCEAN and SLAND from process models. See Table 4 for references.

	Jena CarboScope	Copernicus Atmosphere Monitoring Service (CAMS)	Carbon-Tracker Europe (CTE)	NISMON-CO ₂	CT-NOAA	CMS-Flux	Copernicus Atmosphere Monitoring Service (CAMS)	GONGGA	THU	COLA	GCA5v2	UoE	IAPCAS	MIROC4-ATCM
Version number	nbetEXToc_v2023	v22r1	v2023	v2023.1	CT2022 + CT-NRT.v2023-3	v2023	FT23r1	v2023	v2023	v2023	v2023	v2023	v2023	v2023
Flags														Decadal growth rate bias and NH aircraft residuals large
Observations														
Atmospheric observations	Flasks and hourly from various institutions (outliers removed by 2 σ criterion)	Hourly resolution (well-mixed conditions) obspack GLOBALVIEWplus v8.0 (NOAA and ICOS) and NRT_v8.1	Hourly resolution (well-mixed conditions) obspack GLOBALVIEWplus v8.0 and NRT_v8.1	Hourly resolution (well-mixed conditions) obspack GLOBALVIEWplus v8.0 and NRT_v8.1	Hourly resolution (well-mixed conditions) obspack GLOBALVIEWplus v8.0 and NRT_v8.1	ACOS-GOSAT v9r, V11.1 OCO-2 scaled to WMO 2019 standard and obspack GLOBALVIEWplus v8.0 and NRT_v8.1.	OCO-2 ACOS retrievals from NASA, v11.1	OCO-2 v11r data that scaled to WMO 2019 standard	OCO-2 v11r data scaled to WMO 2019 standard	Hourly resolution (well-mixed conditions) obspack GLOBALVIEWplus v8.0 and NRT_v8.1. And OCO-2_b11.1_LNLG	ACOS v11 OCO-2 retrievals, scaled to WMO 2019 standard	Hourly resolution (well-mixed conditions) obspack GLOBALVIEWplus v8.0 and NRT_v8.1	Hourly resolution (well-mixed conditions) obspack GLOBALVIEWplus v8.0 and NRT_v8.1	Hourly resolution (well-mixed conditions) obspack GLOBALVIEWplus v8.0 and NRT_v8.2 and JMA
Period covered	1957-2022	1979-2022	2001-2022	1990-2022	2000-2022	2010-2022	2015-2022	2015-2022	2015-2022	2015-2022	2015-2022	2001-2022	2001-2022	2001-2022
Prior fluxes														
Biosphere and fires	Zero	ORCHIDEE, GFEDv4.1s	SiB4 and GFAS	VISIT and GFEDv4.1s	GFED-CASA and GFED_CMS (Climatology for the CT-NRT of CT2022 plus statistical flux anomaly model).	CARDAMOM	ORCHIDEE, GFEDv4.1s	ORCHIDEE-MICT and GFEDv4.1s	SiB4.2 and GFEDv4.1s	SiB4+ GFAS (climatology for the last 4 years)	BEPS	CASA v1.0, climatology after 2016 and GFED4.0	CASA v1.0, climatology after 2016 and GFED4.0	CASA-3h + VISIT-3h

Ocean	CarboSc ope v2023	CMEMS- LSCE- FFNN 2022	CarboSc ope v2022	JMA global ocean mapping (Iida et al., 2021)	Ocean inversio n fluxes, Takahas hi pCO ₂	MOM6	CMEMS -LSCE- FFNN 2022	Takahas hi climatol ogy	Takahas hi climatol ogy	CarboSc ope v2022	JMA Ocean CO ₂ Map v2022 (Global) and v2023 (regiona l)	Takahas hi climatol ogy	Takahas hi climatol ogy	Takahas hi climatol ogy
Fossil fuels (c)	GridFED v2023.1	GridFED 2022.2 with an extrapol ation to 2022-23 based on Carbon monitor and NO ₂	GridFED 2023.1	GridFED v2023.1	Miller/C T, and ODIAC/ NASA	GridFED 2023.1	GridFED 2022.2 with an extrapol ation to 2022-23 based on Carbon monitor and NO ₂	GridFED 2023.1	GridFED v2023.1	GridFED v2023.1	GridFED v2023.1	GridFED 2023.1	GridFED 2023.1	GridFED v2023.1
Transport and optimization														
Transport model	TM3	LMDZ v6	TM5	NICAM- TM	TM5	GEOS- CHEM	LMDZ v6	GEOS- Chem v12.9.3	GEOS- CHEM	GEOS- CHEM v13.0.2	MOZAR T-4	GEOS- CHEM	GEOS- CHEM v12.5	MIROC4 -ACTM
Weather forcing	NCEP	ECMWF	ECMWF	JRA55	ERA5	MERRA 2	ECMWF	MERRA 2	GEOS- FP	MERRA- 2	GEOS5	MERRA	MERRA	JRA-55
Horizontal Resolution	Global 3.83°x5°	Global 2.5°x1.2 7°	Global 3°x2°, Europe 1°x1°, North America 1°x1°	Isocahed ral grid: ~223km	Global 3°x2°, North America 1°x1°	Global 4°x5°	Global 2.5°x1.2 7°	Global 2°x2.5°	Global 4°x5°	Global 2°x2.5°	Global 2.5°x1.8 75°	Global 2°x2.5°	Global 4°x5°	Global 2.8°x2.8 °
Optimization	Conjugat e gradient (re- ortho- normaliz ation)	Variatio nal	5-week ensemble Kalman smoother	Variation al	12- week ensembl e Kalman smooth er	Variatio nal	Variatio nal	Nonline ar least squares four- dimensi onal variatio n (NLS- 4DVar)	Ensemb le Kalman filter	Ensemb le Kalman Filter (LETKF with CEnKF/ AAPO)	Ensemb le Kalman filter	Ensemb le Kalman filter	Ensemb le Kalman filter	Bayesia n inversio n, similar to that of Rayner et al. (1999)
(a) Schuldt et al. (2022)														
(b) Schuldt et al. (2023)														
(c) GCP-GridFED v2023.1 and v2022.2 (Jones et al., 2023) are updates through the year 2022 of the GCP-GridFED dataset presented by Jones et al. (2021b).														
(d) ocean prior not optimised														

887

888

889

890

891

892

Table S5. Comparison of the projection with realised fossil CO₂ emissions (EFOS). The ‘Actual’ values are first the estimate available using actual data, and the ‘Projected’ values refers to estimates made before the end of the year for each publication. Projections based on a different method from that described here during 2008-2014 are available in Le Quéré et al., (2016). All values are adjusted for leap years.

	World		China		USA		EU28 / EU27 (i)		India		Rest of World	
	Projected	Actual	Projected	Actual	Projected	Actual	Projected	Actual	Projected	Actual	Projected	Actual
2015 (a)	-0.6%	0.06%	-3.9%	-0.7%	-1.5%	-2.5%	-	-	-	-	1.2%	1.2%
	(-1.6 to 0.5)		(-4.6 to -1.1)		(-5.5 to 0.3)						(-0.2 to 2.6)	
2016 (b)	-0.2%	0.20%	-0.5%	-0.3%	-1.7%	-2.1%	-	-	-	-	1.0%	1.3%
	(-1.0 to +1.8)		(-3.8 to +1.3)		(-4.0 to +0.6)						(-0.4 to +2.5)	
2017 (c)	2.0%	1.6%	3.5%	1.5%	-0.4%	-0.5%	-	-	2.00%	3.9%	1.6%	1.9%
	(+0.8 to +3.0)		(+0.7 to +5.4)		(-2.7 to +1.0)				(+0.2 to +3.8)		(0.0 to +3.2)	
2018 (d)	2.7%	2.1%	4.7%	2.3%	2.5%	2.8%	-0.7%	-2.1%	6.3%	8.0%	1.8%	1.7%
	(+1.8 to +3.7)		(+2.0 to +7.4)		(+0.5 to +4.5)		(-2.6 to +1.3)		(+4.3 to +8.3)		(+0.5 to +3.0)	
2019 (e)	0.5%	0.1%	2.6%	2.2%	-2.4%	-2.6%	-1.7%	-4.3%	1.8%	1.0%	0.5%	0.5%
	(-0.3 to +1.4)		(+0.7 to +4.4)		(-4.7 to -0.1)		(-5.1 to +1.8%)		(-0.7 to +3.7)		(-0.8 to +1.8)	
2020 (f)	-6.7%	-5.4%	-1.7%	1.4%	-12.2%	-10.6%	-11.3% (EU27)	-10.9%	-9.1%	-7.3%	-7.4%	-7.0%
2021 (g)	4.8%	5.1%	4.3%	3.5%	6.8%	6.2%	6.3%	6.8%	11.2%	11.1%	3.2%	4.5%
	(4.2 to 5.4%)		(3.0 to 5.4%)		(6.6 to 7.0%)		(4.3 to 8.3%)		(10.7 to 11.7%)		(2.0 to 4.3%)	
2022 (h)	1.1%	0.9%	-1.5%	0.9%	1.6%	1.0%	-1.0%	-1.9%	5.6%	5.8%	2.5%	0.6%
	(0% to 1.7%)		(-3.0 to 0.1%)		(-0.9 to 4.1%)		(-2.9 to 1.0%)		(3.5 to 7.7%)		(0.1 to 2.3%)	
2023 (j)	1.2%		4.0%		-3.4%		-7.1%		8.0%		0.9%	
	(0.2 to 2.3%)		(1.9 to 6.2%)		(-5.9 to -0.9%)		(-9.6 to -4.6%)		(5.8 to 10.2%)		(-0.8 to 2.6%)	

(a) Jackson et al. (2016) and Le Quéré et al. (2015a). (b) Le Quéré et al. (2016). (c) Le Quéré et al. (2018a). (d) Le Quéré et al. (2018b). (e) Friedlingstein et al., (2019), (f) Friedlingstein et al., (2020), (g) Friedlingstein et al., (2022a), (h) Friedlingstein et al., (2022b) (j) This study

(i) EU28 until 2019, EU27 from 2020

Table S6 Attribution of fCO₂ measurements for the year 2022 included in SOCATv2023 (Bakker et al., 2016, 2023) to inform ocean fCO₂-based data products.

Platform Name	Regions	No. of measurements	Principal Investigators	No. of datasets	Platform Type
Atlantic Explorer	North Atlantic, Tropical Atlantic, coastal	45,321	Bates, N. R.	22	Ship
Atlantic Sail	North Atlantic, coastal	25,691	Steinhoff, T.; Körtzinger, A.	7	Ship
Bell M. Shimida	North Pacific, Tropical Pacific, coastal	42,300	Alin, S. R.; Feely, R. A.	12	Ship
Cap San Lorenzo	North Atlantic, tropical Atlantic, coastal	32,145	Lefèvre, N.	6	Ship
Celtic Explorer	North Atlantic, coastal	36,155	Cronin, M.	3	Ship
Colibri	North Atlantic, tropical Atlantic, coastal	19,199	Lefèvre, N.	3	Ship
Equinox	North Atlantic, Tropical Atlantic, coastal	6,021	Wanninkhof, R.; Pierrot, D.	3	Ship
F.G. Walton Smith	Coastal	19,487	Rodriguez, C.; Millero, F. J.; Barbero, L.; Pierrot, D.; Wanninkhof, R.	14	Ship
Finnmaid	Coastal	218,365	Rehder, G.; Bittig, H. C.; Glockzin, M.	14	Ship
GEOMAR surface buoy 1	Tropical Atlantic	7,223	Paulsen M.; Fielder B.; Körtzinger A.	1	Mooring
GEOMAR waveglider 4	Tropical Atlantic	1,228	Paulsen M.; Fielder B.; Körtzinger A.	1	Autonomous Surface Vehicle
G.O. Sars	Arctic, North Atlantic, coastal	105,798	Skjelvan, I.	12	Ship
GAKOA_149W_60N	Coastal	696	Monacci, N.; Sutton, A.J.	1	Mooring
Gordon Gunter	Coastal	11,542	Wanninkhof, R.; Pierrot, D.	2	Ship
Healy	Arctic, North Pacific, coastal	35,557	Sweeney, C.; Newberger, T.; Sutherland, S. C.; Munro, D. R.	7	Ship
Henry B. Bigelow	Coastal	61,347	Wanninkhof, R.; Pierrot, D.	12	Ship
Heron Island	Coastal	1,531	Tilbrook, B.	1	Mooring
Investigator	Southern Ocean	8,505	Tilbrook, B.; Akl, J.; Neill, C.	1	Ship
Kangaroo Island	Southern Ocean	1,533	Tilbrook, B.	1	Mooring
KC_BUOY	Coastal	7,750	Evans, W.	1	Mooring
Keifu Maru II	North Pacific, Tropical Pacific, coastal	7,264	Enyo, K.	5	Ship
Laurence M. Gould	Southern Ocean	10,640	Sweeney, C.; Newberger, T.; Sutherland, S. C.; Munro, D. R.	5	Ship
Maria Island	Southern Ocean	1,707	Tilbrook, B.	1	Mooring
Marion Dufresne	Indian, Southern Ocean	3,609	Lo Monaco, C.; Metzl, N.	1	Ship
M2_164W_57N	Coastal	926	Monacci, N.; Sutton, A.J.	2	Mooring
Nathaniel B. Palmer	Southern Ocean	19,754	Sweeney, C.; Newberger, T.; Sutherland, S. C.; Munro, D. R.	1	Ship

New Century 2	North Pacific, Tropical Pacific, North Atlantic, Tropical Atlantic, Southern Ocean, coastal	278,287	Nakaoka, S.-I., Takao, S.	11	Ship
Nexans - Art and Fenetres	North Atlantic, coastal	4,732	Tanhua, T.	1	Ship
Quadra Island Field Station	Coastal	83,322	Evans, W.	1	Mooring
Roger Revelle	North Pacific, Tropical Pacific, coastal	37,705	Alin, S. R.; Feely, R. A.	3	Ship
Ronald H. Brown	North Atlantic, Tropical Atlantic, coastal	47,311	Wanninkhof, R.; Pierrot, D.	5	Ship
Ryofu Maru III	North Pacific, Tropical Pacific, coastal	8,409	Enyo, K.	7	Ship
Saildrone 1079 EuroSea 2021	Tropical Atlantic, coastal	164	Wimart-Rousseau, C.; Sutton, A.J.; Fiedler, B	1	Autonomous Surface Vehicle
Sarmiento de Gamboa	Coastal	2,557	Fontela, M.	1	Ship
Seaspan Royal	Coastal	37,081	Evans, W.	2	Mooring
Sikuliaq	Arctic, North Pacific, coastal	61,475	Sweeney, C.; Newberger, T.; Sutherland, S. C.; Munro, D. R.	14	Ship
Simon Stevin	Coastal	58,087	Gkritzalis, T.; Theetaert, H.; T'Jampens, M.	11	Ship
SOFS_142E_46S	Southern Ocean	1,040	Sutton, A.J.	1	Mooring
Statsraad Lehmkuhl	North Atlantic, Tropical Atlantic, North Pacific, Tropical Pacific, Indian, Southern Ocean, coastal	82,297	Becker, M.; Olsen, A.	5	Ship
Thomas G. Thompson	North Pacific, Tropical Pacific, coastal	51,535	Alin, S. R.; Feely, R. A.	10	Ship
Trans Future 5	North Pacific, Tropical Pacific, Southern Ocean, coastal	167,811	Nakaoka, S.-I.; Nojiri, Y.	15	Ship
Tukuma Arctica	North Atlantic, coastal	58,635	Becker, M.; Olsen, A.	22	Ship
Wakataka Maru	North Pacific, coastal	14,068	Tadokoro, K.; Ono, T.	8	Ship

898
899
900
901
902
903
904
905
906
907
908
909
910
911
912
913
914
915

Table S7. Aircraft measurement programs archived by Cooperative Global Atmospheric Data Integration Project (CGADIP; Schuldt et al. 2022 and 2023) that contribute to the evaluation of the atmospheric inversions (Figure S4).

Site code	Measurement program name in Obstack	Specific doi	Data providers
AAO	Airborne Aerosol Observatory, Bondville, Illinois		Sweeney, C.; Dlugokencky, E.J.
ABOVE	Carbon in Arctic Reservoirs Vulnerability Experiment (CARVE)	https://doi.org/10.3334/ORNLDAC/1404	Sweeney, C., J.B. Miller, A. Karion, S.J. Dinardo, and C.E. Miller. 2016. CARVE: L2 Atmospheric Gas Concentrations, Airborne Flasks, Alaska, 2012-2015. ORNL DAAC, Oak Ridge, Tennessee, USA.
ACG	Alaska Coast Guard		Sweeney, C.; McKain, K.; Karion, A.; Dlugokencky, E.J.
ACT	Atmospheric Carbon and Transport - America		Sweeney, C.; Dlugokencky, E.J.; Baier, B.; Montzka, S.; Davis, K.
AIRCOREN OAA	NOAA AirCore		Colm Sweeney (NOAA) AND Bianca Baier (NOAA)
ALF	Alta Floresta		Gatti, L.V.; Gloor, E.; Miller, J.B.;
AOA	Aircraft Observation of Atmospheric trace gases by JMA		ghg_obs@met.kishou.go.jp
BGI	Bradgate, Iowa		Sweeney, C.; Dlugokencky, E.J.
BNE	Beaver Crossing, Nebraska		Sweeney, C.; Dlugokencky, E.J.
BRZ	Berezorechka, Russia		Sasakama, N.; Machida, T.
CAR	Briggsdale, Colorado		Sweeney, C.; Dlugokencky, E.J.
CMA	Cape May, New Jersey		Sweeney, C.; Dlugokencky, E.J.
CON	CONTRAIL (Comprehensive Observation Network for TRace gases by AirLiner)	http://dx.doi.org/10.17595/20180208.001	Machida, T.; Ishijima, K.; Niwa, Y.; Tsuboi, K.; Sawa, Y.; Matsueda, H.; Sasakawa, M.
CRV	Carbon in Arctic Reservoirs Vulnerability Experiment (CARVE)		Sweeney, C.; Karion, A.; Miller, J.B.; Miller, C.E.; Dlugokencky, E.J.
DND	Dahlen, North Dakota		Sweeney, C.; Dlugokencky, E.J.
ESP	Estevan Point, British Columbia		Sweeney, C.; Dlugokencky, E.J.
ETL	East Trout Lake, Saskatchewan		Sweeney, C.; Dlugokencky, E.J.
FWI	Fairchild, Wisconsin		Sweeney, C.; Dlugokencky, E.J.
GSFC	NASA Goddard Space Flight Center Aircraft Campaign		Kawa, S.R.; Abshire, J.B.; Riris, H.
HAA	Molokai Island, Hawaii		Sweeney, C.; Dlugokencky, E.J.
HFM	Harvard University Aircraft Campaign		Wofsy, S.C.
HIL	Homer, Illinois		Sweeney, C.; Dlugokencky, E.J.
HIP	HIPPO (HIAPER Pole-to-Pole Observations)	https://doi.org/10.3334/CDIAC/HIPPO_010	Wofsy, S.C.; Stephens, B.B.; Elkins, J.W.; Hints, E.J.; Moore, F.
IAGOS-CARIBIC	In-service Aircraft for a Global Observing System		Obersteiner, F.; Boenisch, H.; Gehrlein, T.; Zahn, A.; Schuck, T.
INX	INFLUX (Indianapolis Flux Experiment)		Sweeney, C.; Dlugokencky, E.J.; Shepson, P.B.; Turnbull, J.
LEF	Park Falls, Wisconsin		Sweeney, C.; Dlugokencky, E.J.
MAN	Manaus, Brazil		Miller, J.B.; Martins, G.A.; de Souza, R.A.F.
MEX	High Altitude Global Climate Observation Center, Mexico		Lan, X.; Dlugokencky, E.
NHA	Offshore Portsmouth, New Hampshire (Isles of Shoals)		Sweeney, C.; Dlugokencky, E.J.

OIL	Oglesby, Illinois		Sweeney, C.; Dlugokencky, E.J.
ORC	ORCAS (O ₂ /N ₂ Ratio and CO ₂ Airborne Southern Ocean Study)	https://doi.org/10.5065/D6SB445X	Stephens, B.B, Sweeney, C., McKain, K., Kort, E.
PFA	Poker Flat, Alaska		Sweeney, C.; Dlugokencky, E.J.
RBA-B	Rio Branco		Gatti, L.V.; Gloor, E.; Miller, J.B.
RTA	Rarotonga		Sweeney, C.; Dlugokencky, E.J.
SAN	Santarem, Brazil		Sweeney, C.; Dlugokencky, E.J.; Gatti, L.V.; Gloor, E.; Miller, J.B.
SCA	Charleston, South Carolina		Sweeney, C.; Dlugokencky, E.J.
SGP	Southern Great Plains, Oklahoma		Sweeney, C.; Dlugokencky, E.J.; Biraud, S.
TAB	Tabatinga		Gatti, L.V.; Gloor, E.; Miller, J.B.
TGC	Offshore Corpus Christi, Texas		Sweeney, C.; Dlugokencky, E.J.
THD	Trinidad Head, California		Sweeney, C.; Dlugokencky, E.J.
UGD	Kajjansi Airfield, Kampala, Uganda		McKain, K; Sweeney, C
ULB	Ulaanbaatar, Mongolia		Sweeney, C.; Dlugokencky, E.J.
WBI	West Branch, Iowa		Sweeney, C.; Dlugokencky, E.J.
(a) Schuldt et al. (2022)			
(b) Schuldt et al. (2023)			

917

918

919

Table S8. Main methodological changes in the global carbon budget since first publication. Methodological changes introduced in one year are kept for the following years unless noted. Empty cells mean there were no methodological changes introduced that year.

Publication year	Fossil fuel emissions			LUC emissions	Reservoirs			Uncertainty & other changes
	Global	Country (territorial)	Country (consumption)		Atmosphere	Ocean	Land	
2006 (a)		Split in regions						
2007 (b)				ELUC based on FAO-FRA 2005; constant ELUC for 2006	1959-1979 data from Mauna Loa; data after 1980 from global average	Based on one ocean model tuned to reproduced observed 1990s sink		$\pm 1\sigma$ provided for all components
2008 (c)				Constant ELUC for 2007				
2009 (d)		Split between Annex B and non-Annex B	Results from an independent study discussed	Fire-based emission anomalies used for 2006-2008		Based on four ocean models normalised to observations with constant delta	First use of five DGVMs to compare with budget residual	
2010 (e)	Projection for current year based on GDP	Emissions for top emitters		ELUC updated with FAO-FRA 2010				
2011 (f)			Split between Annex B and non-Annex B					
2012 (g)		129 countries from 1959	129 countries and regions from 1990-2010 based on GTAP8.0	ELUC for 1997-2011 includes interannual anomalies from fire-based emissions	All years from global average	Based on 5 ocean models normalised to observations with ratio	Ten DGVMs available for SLAND; First use of four models to compare with ELUC	

2013 (h)		250 countries ^b	134 countries and regions 1990-2011 based on GTAP8.1, with detailed estimates for years 1997, 2001, 2004, and 2007	ELUC for 2012 estimated from 2001-2010 average		Based on six models compared with two data-products to year 2011	Coordinated DGVM experiments for SLAND and ELUC	Confidence levels; cumulative emissions; budget from 1750
2014 (i)	Three years of BP data	Three years of BP data	Extended to 2012 with updated GDP data	ELUC for 1997-2013 includes interannual anomalies from fire-based emissions		Based on seven models	Based on ten models	Inclusion of breakdown of the sinks in three latitude bands and comparison with three atmospheric inversions
2015 (j)	Projection for current year based Jan-Aug data	National emissions from UNFCCC extended to 2014 also provided	Detailed estimates introduced for 2011 based on GTAP9			Based on eight models	Based on ten models with assessment of minimum realism	The decadal uncertainty for the DGVM ensemble mean now uses $\pm 1\sigma$ of the decadal spread across models
2016 (k)	Two years of BP data	Added three small countries; China's emissions from 1990 from BP data (this release only)		Preliminary ELUC using FRA-2015 shown for comparison; use of five DGVMs		Based on seven models	Based on fourteen models	Discussion of projection for full budget for current year
2017 (l)	Projection includes India-specific data			Average of two bookkeeping models; use of 12 DGVMs		Based on eight models that match the observed sink for the 1990s; no longer normalised	Based on 15 models that meet observation-based criteria (see Sect. 2.5)	Land multi-model average now used in main carbon budget, with the carbon imbalance presented separately; new table of key uncertainties

2018	Revision in cement emissions; Projection includes EU-specific data	Aggregation of overseas territories into governing nations for total of 213 countries a		Average of two bookkeeping models; use of 16 DGVMs	Use of four atmospheric inversions	Based on seven models	Based on 16 models; revised atmospheric forcing from CRUNCEP to CRUJRA	Introduction of metrics for evaluation of individual models using observations
a Raupach et al. (2007)								
b Canadell et al. (2007)								
c GCP (2008)								
d Le Quéré et al. (2009)								
e Friedlingstein et al. (2010)								
f Peters et al. (2012a)								
g Le Quéré et al. (2013), Peters et al. (2013)								
h Le Quéré et al. (2014)								
i Le Quéré et al. (2015a)								
j Le Quéré et al. (2015b)								
k Le Quéré et al. (2016)								
l Le Quéré et al. (2018a)								

Table S9: Mapping of global carbon cycle models' land flux definitions to the definition of the LULUCF net flux used in national reporting to UNFCCC. Non-intact lands are used here as proxy for "managed lands" in the country reporting, national Greenhouse Gas Inventories (NGHGI) are gap-filled (see Supplement S.2.3 for details). For comparison, we provide FAOSTAT estimates (note that FAOSTAT refers to 2003-2012 and 2012-2021). Units are GtC yr⁻¹.

			2003-2012	2013-2022
ELUC from bookkeeping estimates (from Tab. 5)			1.41	1.27
SLAND	Total (from Tab. 5)	from DGVMs	2.86	3.35
	in non-forest lands	from DGVMs	0.53	0.58
	in non-intact forest	from DGVMs	1.87	2.04
	in intact forests	from DGVMs	0.44	0.48
ELUC subtract SLAND on non-intact lands	considering non-intact forests only	from bookkeeping ELUC and DGVMs	-0.46	-0.77
National Greenhouse Gas Inventories (LULUCF)			-0.43	-0.66
FAOSTAT (LULUCF)			0.35	0.25

Table S10 - Evaluation of global ocean biogeochemistry models based on comparison with observation-based interior ocean carbon accumulation (Gruber et al., 2019) and process-based evaluation metrics for Atlantic Meridional Overturning Circulation (AMOC), Southern Ocean sea surface salinity and surface ocean Revelle factor (following the RECCAP2 ocean model evaluation chapter, Terhaar et al., in review) and Southern Ocean stratification index (Bourgeois et al., 2022). See supplement S3.3 for details of calculation and observational data sources. Note that AMOC from MOM6-Cobalt (Princeton) is only available between 2018 - 2022, which is the value reported here

Global Ocean Biogeochemistry Models											
Metric	Observations	ACCESS (CSIRO)	CESM-ETHZ	FESOM2.1-REcoM	MOM6-Cobalt (Princeton)	MPIOM-HAMOC6	MRI-ESM2-2	NEMO-PISCES (IPSL)	NEMO-PlankTOM12	NEMO3.6-PISCESv2-gas (CNRM)	NorESM-OC1.2
Interior ocean anthropogenic carbon accumulation 1994-2007 in GtC yr⁻¹ (Gruber et al., 2019)											
Global	33.7 ± 4.0	36.4	26.7	30.9	27.3	25.5	27.6	26.0	26.0	26.2	33.5
North	5.9	6.3	5.5	5.8	5.2	6.9	5.6	5.7	4.1	5.6	6.8
Tropics	17.5	15.1	12.2	13.2	11.6	10.9	12.5	11.1	12.6	12.1	13.7
South	10.4	15.0	9.0	11.9	10.6	7.8	9.5	9.2	9.4	8.5	12.9
Atlantic Meridional Overturning Circulation at 26°N, 2005-2021 in Sv (Moat et al., 2023)	16.8 ± 0.6	9.5	14.3	10.0	11.6	15.1	13.4	15.7	18.0	12.8	23.0
Southern Ocean sea surface salinity 2005-2021 in psu (Good et al., 2013)											
subpolar seasonally stratified biome (SPSS)	33.936	34.266	33.806	34.262	34.053	33.921	34.090	34.179	34.050	33.817	34.133
subpolar seasonally stratified and subtropical seasonally stratified biomes (SPSS+STSS)	34.302	34.582	34.177	34.537	34.385	34.256	34.388	34.445	34.361	34.121	34.503
Southern Ocean stratification index 2005-	5.88	5.44	5.94	5.68	6.13	5.97	6.00	5.92	5.11	6.21	5.77

2021, in kg m-3 (Bourgeois et al., 2022, Good et al., 2013)											
Surface ocean Revelle factor											
1997-2007, unitless (GLODAPv2.2016, Lauvset et al., 2016)	10.44	10.60	10.31	10.66	10.33	10.72	10.58	10.64	10.33	10.75	10.57
2005-2021, unitless (OceanSODA_v2023, updated from Gregor and Gruber, 2021)	10.62	10.76	10.50	10.85	10.51	10.92	10.77	10.80	10.48	10.91	10.74

924
925

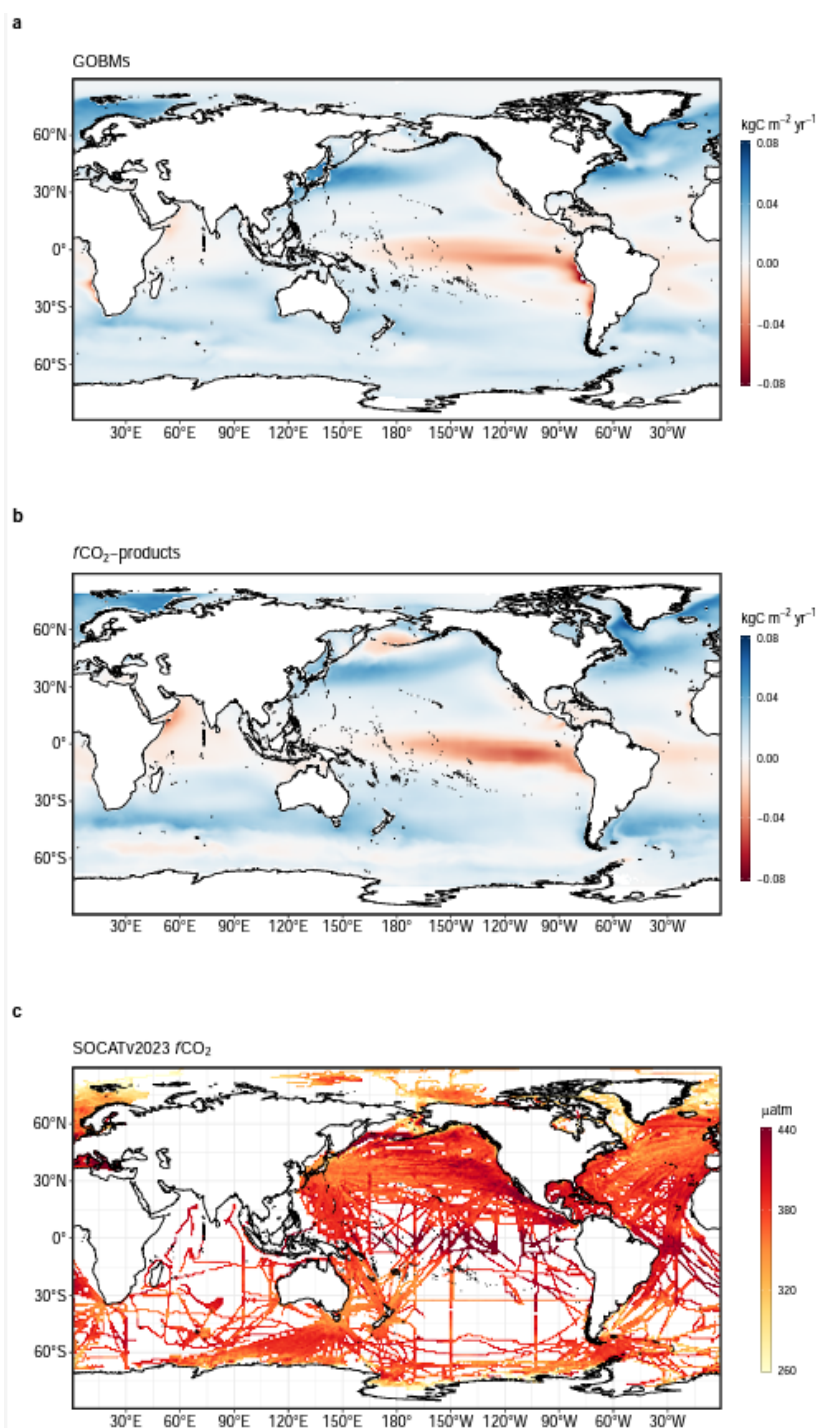


Figure S1. Ensemble mean air-sea CO₂ flux from a) global ocean biogeochemistry models and b) fCO₂ based data products, averaged over 2013-2022 period (kgC m⁻² yr⁻¹). Positive numbers indicate a flux into the ocean. c) gridded SOCAT v2023 fCO₂ measurements, averaged over the 2013-2022 period (μatm). In (a) model simulation A is shown. The fCO₂-products represent the contemporary flux, i.e. including outgassing of riverine carbon, which is estimated to amount to 0.65 GtC yr⁻¹ globally.

Evaluation metrics annual detrended time series (masked, 1990-2022)

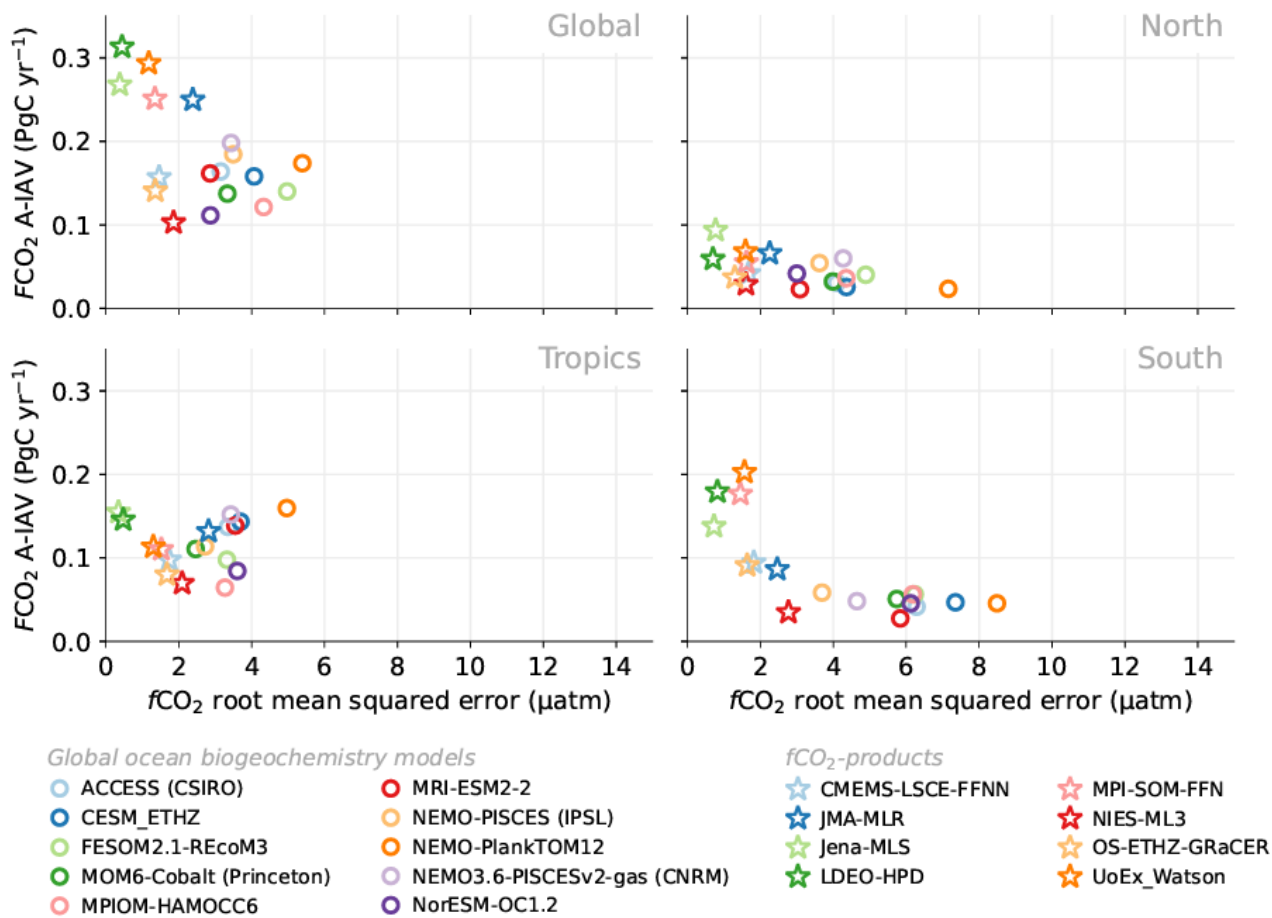


Figure S2. Evaluation of the GOBMs and $f\text{CO}_2$ -products using the root mean squared error (RMSE) for the period 1990 to 2022, between the individual surface ocean $f\text{CO}_2$ mapping schemes and the SOCAT v2023 database. The y-axis shows the amplitude of the interannual variability of the air-sea CO_2 flux (A-IAV, taken as the standard deviation of the detrended annual time series). Results are presented for the globe, north ($>30^\circ\text{N}$), tropics (30°S - 30°N), and south ($<30^\circ\text{S}$) for the GOBMs (see legend, circles) and for the $f\text{CO}_2$ -based data products (star symbols). The $f\text{CO}_2$ -products use the SOCAT database and therefore are not independent from the data (see Section 2.5.1).

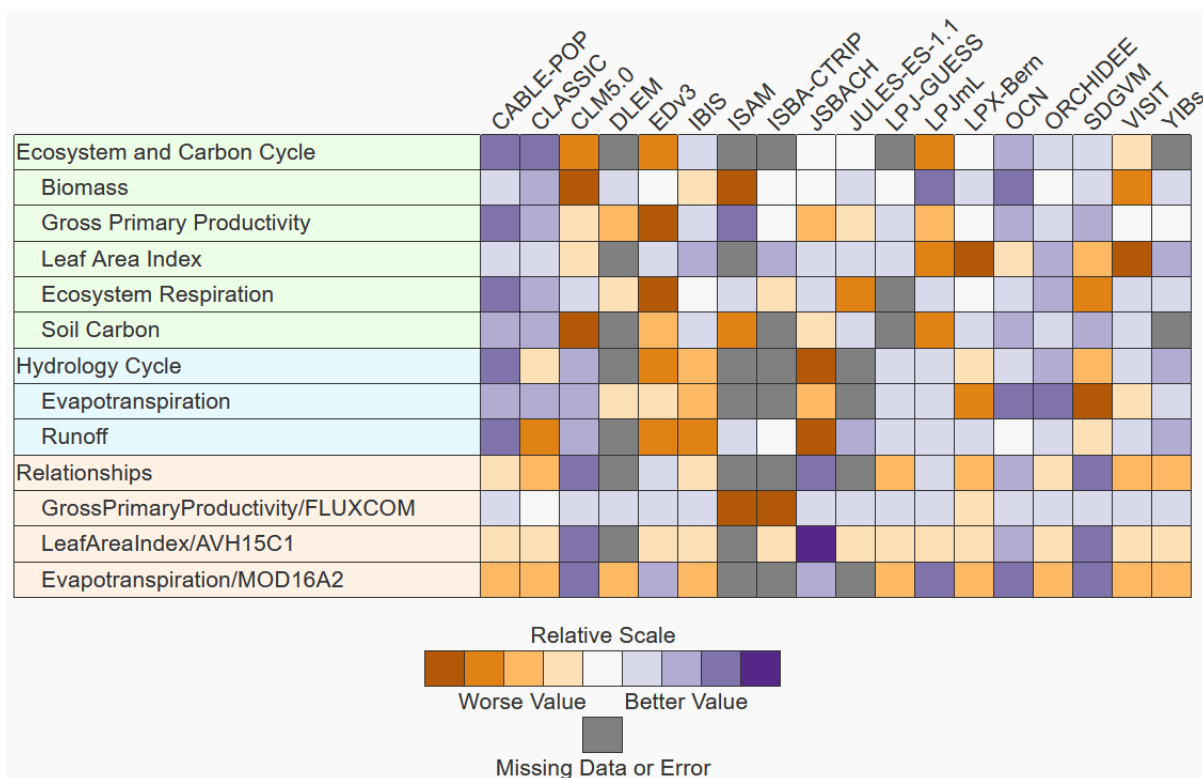


Figure S3. Evaluation of the DGVMs using the International Land Model Benchmarking system (ILAMB; Collier et al., 2018) Skill scores relative to other models. The benchmarking is done with observations for vegetation biomass (Santoro and Cartus, 2021; Saatchi et al., 2011; Thurner et al. 2014), GPP and ecosystem respiration (Reichstein et al., 2007; Lasslop et al., 2010; Knauer et al., 2018; Jung et al., 2017; Tramontana et al., 2016; Alemohammad et al., 2017), leaf area index (Vermote, 2019; Claverie et al., 2016; De Kauwe et al., 2011; Myneni et al., 1997), soil carbon (Hugelius et al., 2013; Fischer et al., 2008), evapotranspiration (De Kauwe et al., 2011; Martens et al., 2017; Miralles et al., 2011; Mu et al., 2011), and runoff (Dai and Trenberth, 2002; Hobeichi et al., 2019; Hobeichi et al., 2020). Metrics include relationships between carbon cycle variables, precipitation (Adler et al., 2003) and temperature (Harris et al., 2014). For each model–observation comparison a series of error metrics are calculated, scores are then calculated as an exponential function of each error metric, and finally for each variable the multiple scores from different metrics and observational datasets are combined to give the overall variable scores. Overall variable scores increase from 0 to 1 with improvements in model performance. The set of error metrics vary with dataset and can include metrics based on the period mean, bias, root mean squared error, spatial distribution, interannual variability, and seasonal cycle. The relative skill score shown is a Z score, which indicates in units of standard deviation the model scores relative to the multi-model mean score for a given variable. Grey boxes represent missing model data.

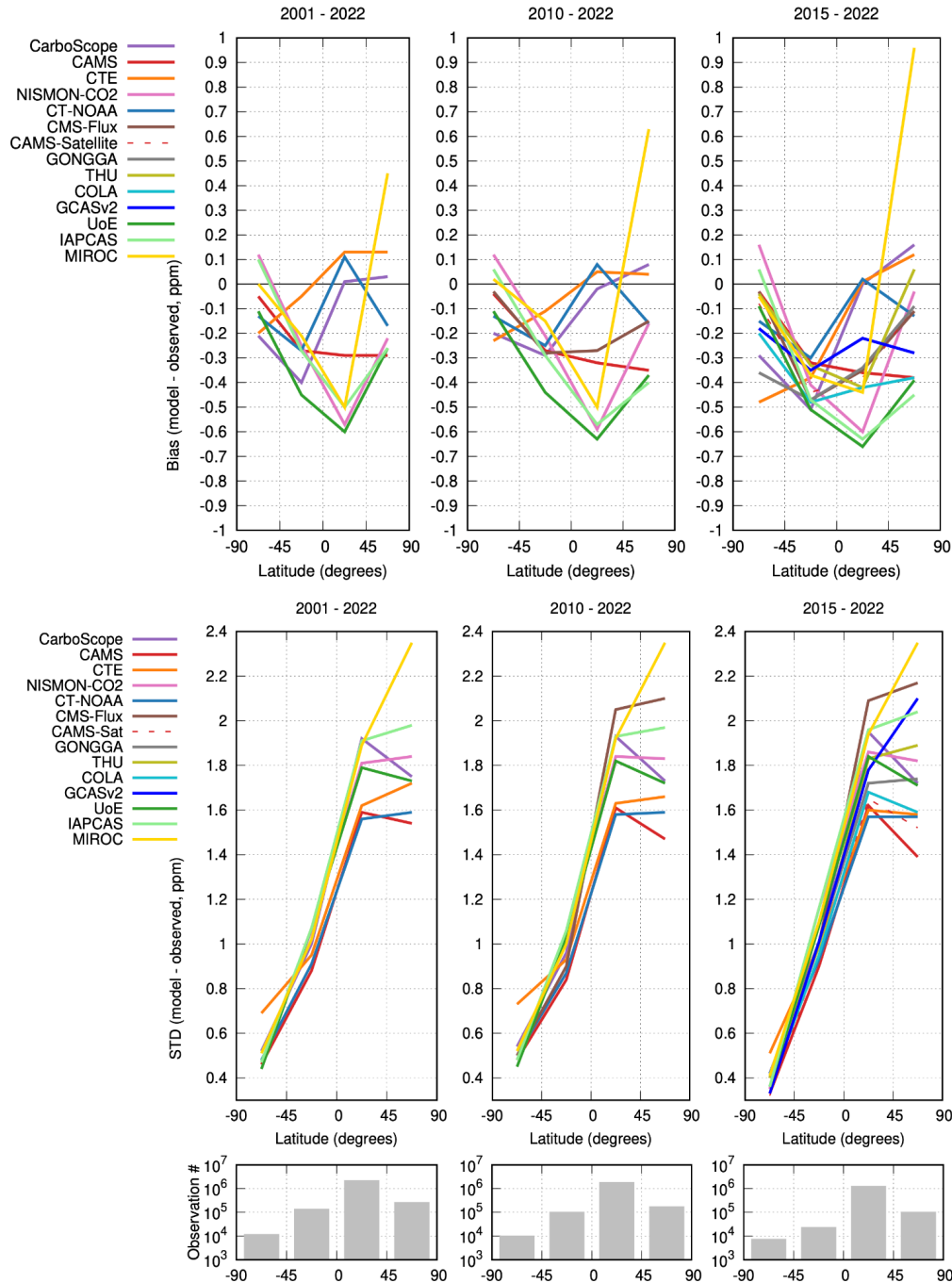


Figure S4. Evaluation of the atmospheric inversion products. The mean of the model minus observations is shown for four latitude bands in three periods: (first panel) 2001-2022, (second panel) 2010-2012, (third panel) 2015-2023. The 14 systems are compared to independent CO₂ observations from aircraft over many places of the world between 2 and 7 km above sea level. Aircraft measurements archived in the Cooperative Global Atmospheric Data Integration Project (Schuldt et al. 2022, Schuldt et al. 2023) from sites, campaigns or programs that have not been assimilated and cover at least 9 months (except for SH programs) between 2001 and 2022, have been used to compute the biases (top row) and their standard deviations (middle row) in four 45° latitude bins. Land and ocean data are used without distinction, and observation density varies strongly with latitude and time as seen on the lower panels.

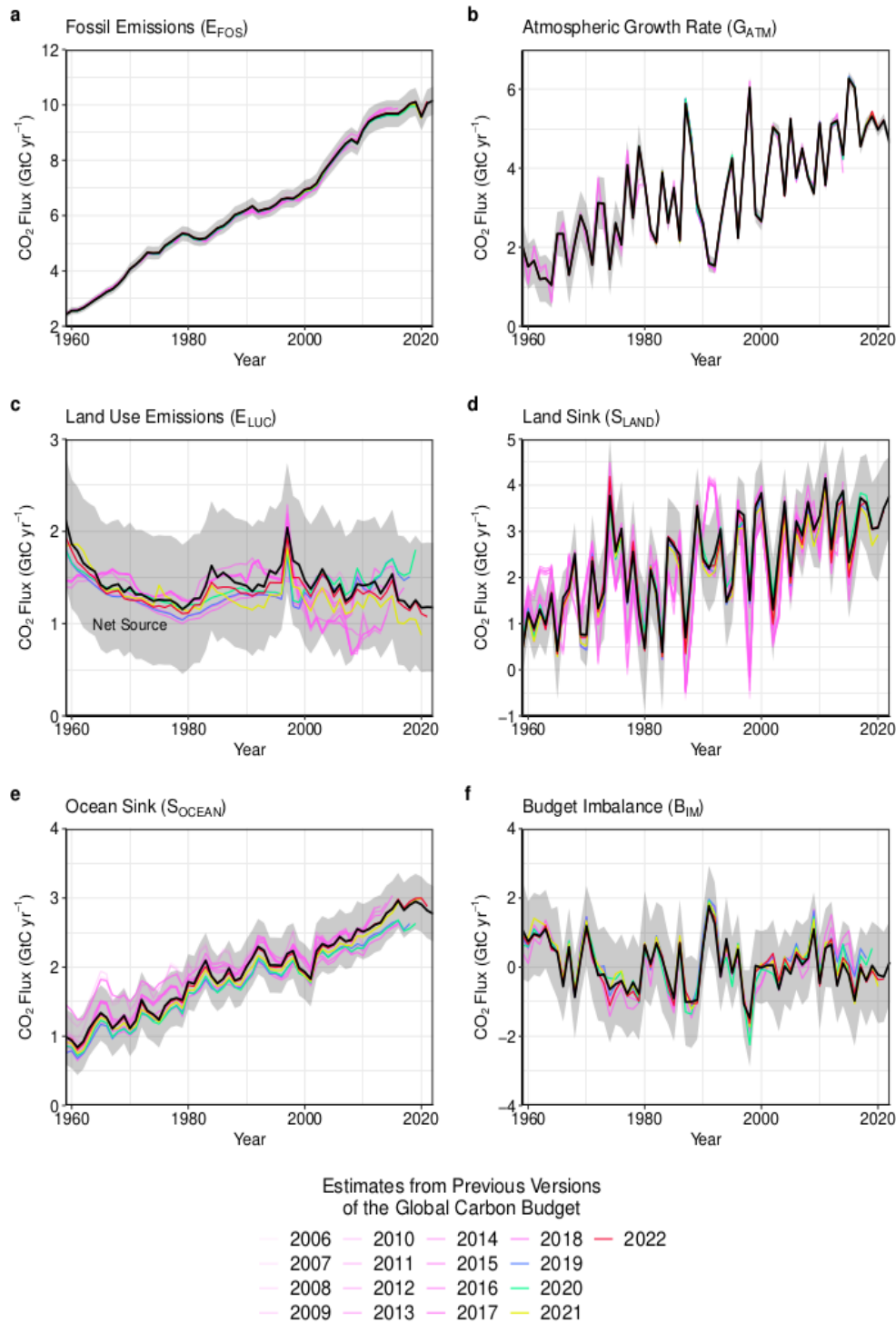


Figure S5. Comparison of the estimates of each component of the global carbon budget in this study (black line) with the estimates released annually by the GCP since 2006. Grey shading shows the uncertainty bounds representing ± 1 standard deviation of the current global carbon budget, based on the uncertainty assessments described in Supplement S1 to S4. CO₂ emissions from (a) fossil CO₂ emissions excluding cement carbonation (E_{FOS}), and (b) land-use change (E_{LUC}), as well as their partitioning among (c) the atmosphere (G_{ATM}), (d) the land (S_{LAND}), and (e) the ocean (S_{OCEAN}). See legend for the corresponding years, and Tables 3 and A8 for description of changes in methodology. The budget year corresponds to the year when the budget was first released. All values are in GtC yr⁻¹.

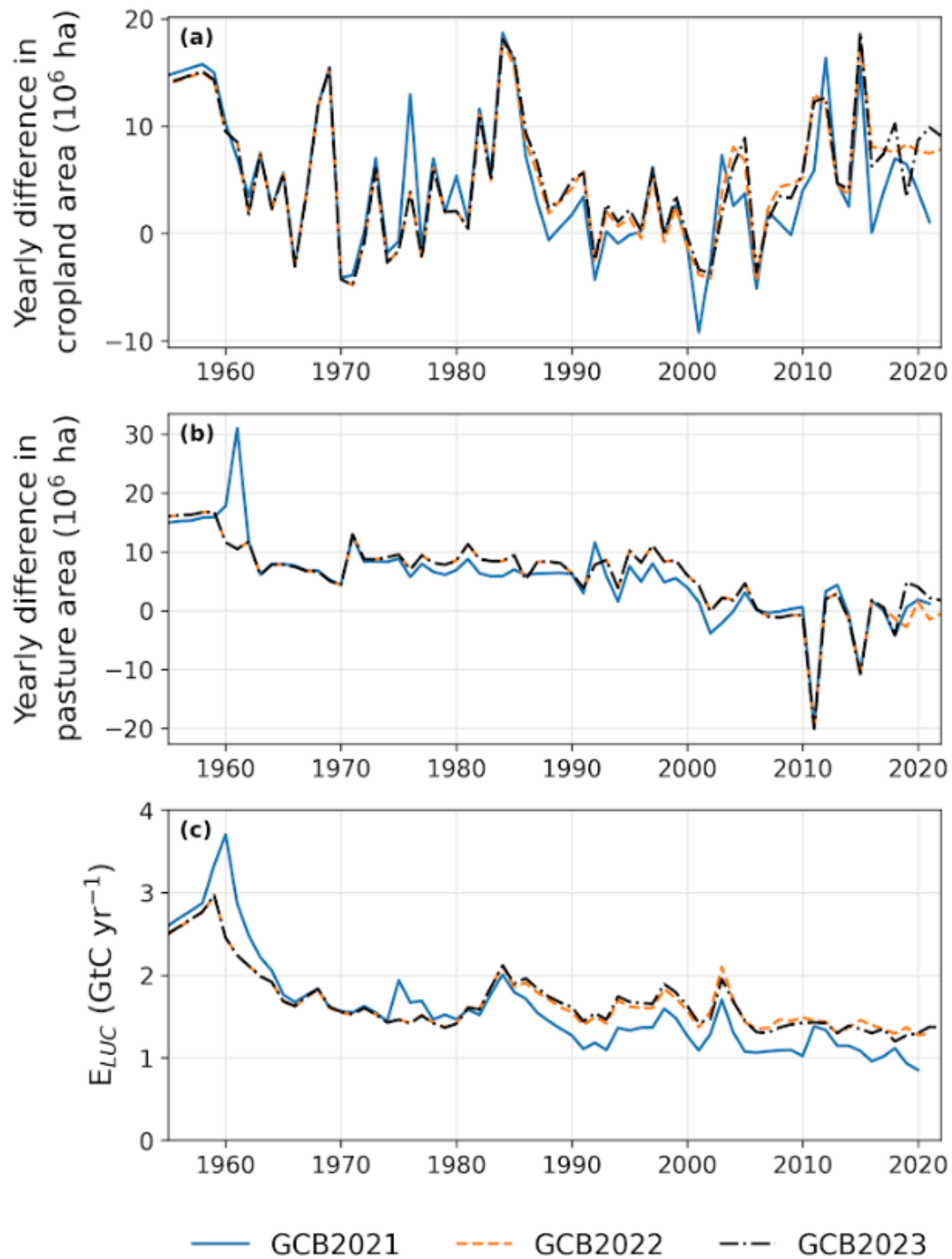


Figure S6. Differences in the HYDE/LUH2 land-use forcing used for the global carbon budgets GCB2021 (Friedlingstein et al., 2022a), GCB2022 (Friedlingstein et al., 2022b), and GCB2023 (this paper). Shown are year-to-year changes in cropland area (top panel) and pasture area (middle panel). To illustrate the relevance of the update in the land-use forcing to the recent trends in E_{LUC} , the bottom panel shows the land-use emission estimate from the bookkeeping model BLUE (original model output, i.e., excluding emissions from peat fire and peat drainage).

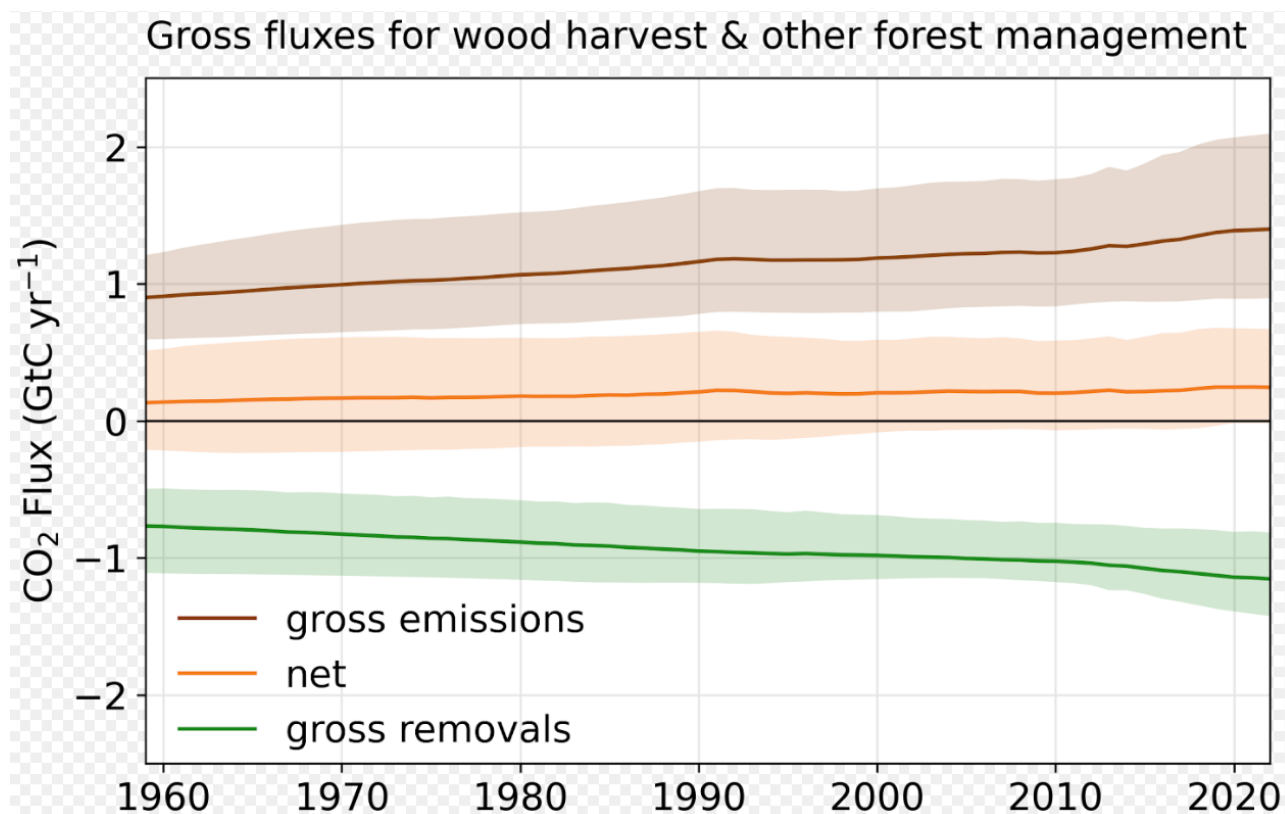


Figure S7: Split of net fluxes from wood harvest and other forest management into gross emissions and gross removals. Solid lines denote the average of the three bookkeeping models and shaded areas the full range (min-max) of the bookkeeping model estimates.

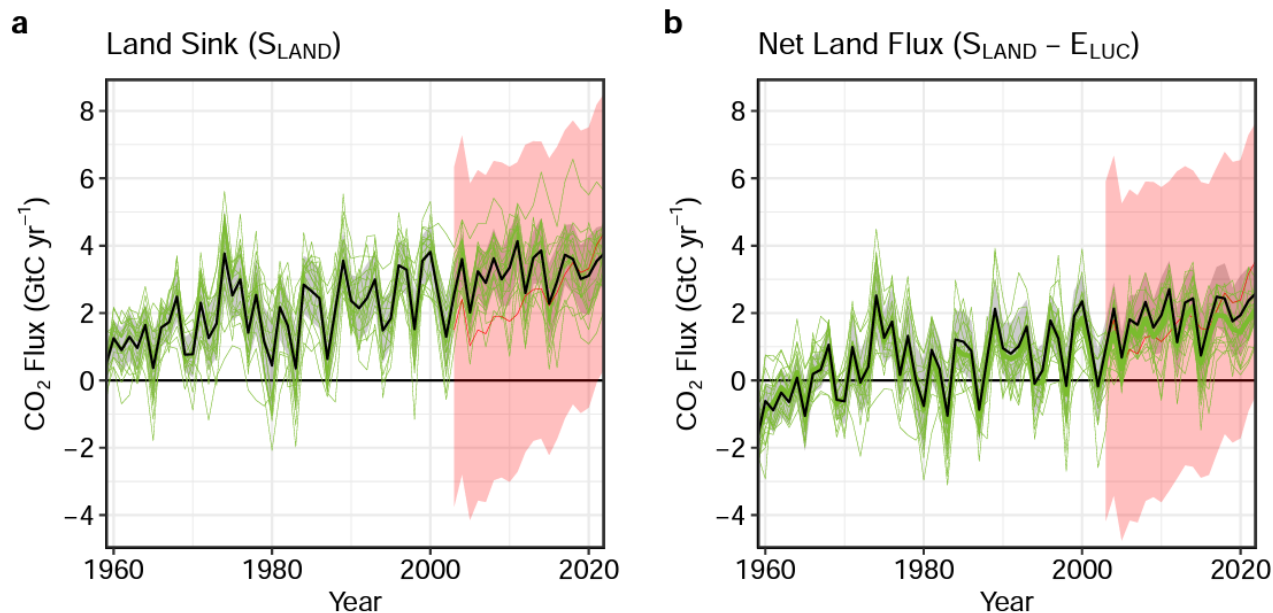


Figure S8. As Figure 8 but with the inclusion of CARDAMOM) (a) The land CO₂ sink (S_{LAND}) estimated by individual DGVMs estimates (green), as well as the budget estimate (black with $\pm 1\sigma$ uncertainty), which is the average of all DGVMs. (b) Total atmosphere-land CO₂ fluxes ($S_{\text{LAND}} - E_{\text{LUC}}$). Panel (b) also includes an estimate for the total land flux for individual DGVMs (thin green lines) and their multi-model mean (thick green line). The red line is the mean CARDAMOM result and uncertainty range in pink.



Figure S9. Fire carbon emissions for the months January-September for each year 2003-2023 from two global fire emissions products. **(Top row)** Global emissions. **(Middle row)** Emissions for the northern hemisphere extratropics (>30° N), tropics (30° N-30° S) and southern extratropics (>30° S). **(Bottom row)** Emissions by RECCAP2 region. The Global Fire Assimilation System (GFAS; Di Giuseppe et al., 2018) (**left column**) and the Global Fire Emissions Database (GFED, version 4.1s; van der Werf et al., 2017) (**right column**) are among the most widely applied global fire emissions products based on satellite remote sensing of fire. GFED relies on the post-fire detection of burned areas combined with fuel consumption factors. GFAS relies on the detection of thermal energy release during active fires.

1011

1012 References

- 1013 Adler, R. F., Huffman, G. J., Chang, A., Ferraro, R., Xie, P.-P., Janowiak, J., Rudolf, B., Schneider, U., Curtis, S., Bolvin,
1014 D., Gruber, A., Susskind, J., Arkin, P., and Nelkin, E.: The Version-2 Global Precipitation Climatology Project (GPCP)
1015 Monthly Precipitation Analysis (1979–Present), *J. Hydrometeor.*, 4, 1147–1167, [https://doi.org/10.1175/1525-7541\(2003\)004<1147:TVGPCP>2.0.CO;2](https://doi.org/10.1175/1525-7541(2003)004<1147:TVGPCP>2.0.CO;2), 2003.
- 1017 Alemohammad, S. H., Fang, B., Konings, A. G., Aires, F., Green, J. K., Kolassa, J., Miralles, D., Prigent, C., and Gentile,
1018 P.: Water, Energy, and Carbon with Artificial Neural Networks (WECANN): a statistically based estimate of global surface
1019 turbulent fluxes and gross primary productivity using solar-induced fluorescence, *Biogeosciences*, 14, 4101–4124,
1020 <https://doi.org/10.5194/bg-14-4101-2017>, 2017.
- 1021 Alkama, R.: Land Carbon Budget: Intact and Non-Intact Forest NBP from TRENDY-v11 S2 simulations [code], available
1022 at: https://github.com/RamAlkama/LandCarbonBudget_IntactAndNonIntactForest, last access: 27 September 2023, 2022.
- 1023 Amante, C. and Eakins, B. W.: ETOPO1 Global Relief Model converted to PanMap layer format, PANGAEA [dataset],
1024 <https://doi.org/10.1594/PANGAEA.769615>, 2009.
- 1025 Andres, R. J., Boden, T. A., Bréon, F.-M., Ciais, P., Davis, S., Erickson, D., Gregg, J. S., Jacobson, A., Marland, G., Miller,
1026 J., Oda, T., Olivier, J. G. J., Raupach, M. R., Rayner, P., and Treanton, K.: A synthesis of carbon dioxide emissions from
1027 fossil-fuel combustion, *Biogeosciences*, 9, 1845–1871, <https://doi.org/10.5194/bg-9-1845-2012>, 2012.
- 1028 Andres, R. J., Boden, T. A., and Higdon, D.: A new evaluation of the uncertainty associated with CDIAC estimates of fossil
1029 fuel carbon dioxide emission, *Tellus B: Chemical and Physical Meteorology*, 66, 23616,
1030 <https://doi.org/10.3402/tellusb.v66.23616>, 2014.
- 1031 Andrew, R. M.: Towards near real-time, monthly fossil CO₂ emissions estimates for the European Union with current-year
1032 projections, *Atmos. Pollut. Res.*, 12, 12, 101229, <https://doi.org/10.1016/j.apr.2021.101229>, 2021.
- 1033 Andrew, R. M. and Peters, G. P.: A multi-region input–output table based on the global trade analysis project database
1034 (GTAP-MRIO), *Economic Systems Research*, 25, 99–121, <https://doi.org/10.1080/09535314.2012.761953>, 2013.
- 1035 Arora, V. K., Boer, G. J., Christian, J. R., Curry, C. L., Denman, K. L., Zahariev, K., Flato, G. M., Scinocca, J. F.,
1036 Merryfield, W. J., and Lee, W. G.: The Effect of Terrestrial Photosynthesis Down Regulation on the Twentieth-Century
1037 Carbon Budget Simulated with the CCCma Earth System Model, 22, 6066–6088, <https://doi.org/10.1175/2009JCLI3037.1>,
1038 2009.
- 1039 Bauer, J. E., Cai, W.-J., Raymond, P. A., Bianchi, T. S., Hopkinson, C. S., and Regnier, P. A. G.: The changing carbon cycle
1040 of the coastal ocean, *Nature*, 504, 61–70, <https://doi.org/10.1038/nature12857>, 2013.
- 1041 Bellouin, N., Rae, J., Jones, A., Johnson, C., Haywood, J., and Boucher, O.: Aerosol forcing in the Climate Model
1042 Intercomparison Project (CMIP5) simulations by HadGEM2-ES and the role of ammonium nitrate, *J. Geophys. Res.-Atmos.*,
1043 116, D20206, <https://doi.org/10.1029/2011JD016074>, 2011.
- 1044 Broecker, W. S.: Ocean chemistry during glacial time, *Geochimica et Cosmochimica Acta*, 46, 1689–1705,
1045 [https://doi.org/10.1016/0016-7037\(82\)90110-7](https://doi.org/10.1016/0016-7037(82)90110-7), 1982.
- 1046 Brunner, L., Pendergrass, A. G., Lehner, F., Merrifield, A. L., Lorenz, R., and Knutti, R.: Reduced global warming from
1047 CMIP6 projections when weighting models by performance and independence, *Earth Syst. Dynam.*, 11, 995–1012,
1048 <https://doi.org/10.5194/esd-11-995-2020>, 2020.
- 1049 Chini, L., Hurtt, G., Sahajpal, R., Frolking, S., Klein Goldewijk, K., Sitch, S., Ganzenmüller, R., Ma, L., Ott, L., Pongratz,
1050 J., and Poulter, B.: Land-use harmonization datasets for annual global carbon budgets, 13, 4175–4189,
1051 <https://doi.org/10.5194/essd-13-4175-2021>, 2021.
- 1052 Claverie, M., Matthews, J., Vermote, E., and Justice, C.: A 30+ Year AVHRR LAI and FAPAR Climate Data Record:
1053 Algorithm Description and Validation, *Remote Sensing*, 8, 263, <https://doi.org/10.3390/rs8030263>, 2016.
- 1054 Conchedda, G. and Tubiello, F. N.: Drainage of organic soils and GHG emissions: Validation with country data, *Biosphere –*
1055 *Biogeosciences*, <https://doi.org/10.5194/essd-2020-202>, 2020.
- 1056 Cooper, D. J., Watson, A. J., and Ling, R. D.: Variation of pCO₂ along a North Atlantic shipping route (U.K. to the
1057 Caribbean): A year of automated observations, *Marine Chemistry*, 60, 147–164, 1998.

1058 Crippa, M., Janssens-Maenhout, G., Guizzardi, D., Van Dingenen, R., and Dentener, F.: Contribution and uncertainty of
1059 sectorial and regional emissions to regional and global PM_{2.5} health impacts, 19, 5165–5186, [https://doi.org/10.5194/acp-](https://doi.org/10.5194/acp-19-5165-2019)
1060 19-5165-2019, 2019.

1061 Dai, A. and Trenberth, K. E.: Estimates of Freshwater Discharge from Continents: Latitudinal and Seasonal Variations, *J.*
1062 *Hydrometeorol.*, 3, 660–687, [https://doi.org/10.1175/1525-7541\(2002\)003<0660:EOFDfC>2.0.CO;2](https://doi.org/10.1175/1525-7541(2002)003<0660:EOFDfC>2.0.CO;2), 2002.

1063 Davis, S. J. and Caldeira, K.: Consumption-based accounting of CO₂ emissions, *Proceedings of the National Academy of*
1064 *Sciences*, 107, 5687–5692, <https://doi.org/10.1073/pnas.0906974107>, 2010.

1065 De Kauwe, M. G., Disney, M. I., Quaife, T., Lewis, P., and Williams, M.: An assessment of the MODIS collection 5 leaf
1066 area index product for a region of mixed coniferous forest, *Remote Sensing of Environment*, 115, 767–780,
1067 <https://doi.org/10.1016/j.rse.2010.11.004>, 2011.

1068 DeVries, T.: The oceanic anthropogenic CO₂ sink: Storage, air-sea fluxes, and transports over the industrial era, *Global*
1069 *Biogeochem. Cycles*, 28, 631–647, <https://doi.org/10.1002/2013GB004739>, 2014.

1070 Dickson, A. G., Sabine, C. L., and Christian, J. R.: Guide to best practices for ocean CO₂ measurement. Sidney, British
1071 Columbia, North Pacific Marine Science Organization, 191pp. (PICES Special Publication 3; IOCCP Report 8). DOI:
1072 <https://doi.org/10.25607/OBP-1342>, 2007.

1073 Duce, R. A., LaRoche, J., Altieri, K., Arrigo, K. R., Baker, A. R., Capone, D. G., Cornell, S., Dentener, F., Galloway, J.,
1074 Ganeshram, R. S., Geider, R. J., Jickells, T., Kuypers, M. M., Langlois, R., Liss, P. S., Liu, S. M., Middelburg, J. J., Moore,
1075 C. M., Nickovic, S., Oschlies, A., Pedersen, T., Prospero, J., Schlitzer, R., Seitzinger, S., Sorensen, L. L., Uematsu, M.,
1076 Ulloa, O., Voss, M., Ward, B., and Zamora, L.: Impacts of Atmospheric Anthropogenic Nitrogen on the Open Ocean,
1077 *Science*, 320, 893–897, <https://doi.org/10.1126/science.1150369>, 2008.

1078 Eakins, B. W. and Sharman, G. F.: National Geophysical Data Center: Volumes of the World's Oceans from ETOPO1,
1079 available at: https://www.ngdc.noaa.gov/mgg/global/etopo1_ocean_volumes.html, last access: 27 September 2023, U.S.
1080 Department of Commerce, 2010.

1081 Eggleston, H. S., Buendia, L., Miwa, K., Ngara, T., and Tanabe, K.: Volume 4: Agriculture, forestry and land use. in: 2006
1082 IPCC guidelines for national greenhouse gas inventories, available at: [https://www.ipcc-](https://www.ipcc-nggip.iges.or.jp/public/2006gl/vol4.html)
1083 [nggip.iges.or.jp/public/2006gl/vol4.html](https://www.ipcc-nggip.iges.or.jp/public/2006gl/vol4.html), last access: 27 September 2023, 2006.

1084 EIA: U.S. Energy Information Administration: Short-Term Energy Outlook, available at:
1085 <http://www.eia.gov/forecasts/steo/outlook>, last access: 27 September 2023, 2022.

1086 FAO: Global Forest Resources Assessment 2020: Main report, FAO, Rome, Italy, 184 pp., <https://doi.org/10.4060/ca9825en>,
1087 2020.

1088 FAO: FAO Statistical Database (FAOSTAT), domains Climate Change, available at:
1089 <http://www.fao.org/faostat/en/#data/GT>, last access: 27 September 2023, 2021.

1090 FAO/UNEP: Food and Agriculture Organisation / United Nations Environment Programme: The state of food and
1091 agriculture 1981, available at: <https://www.fao.org/3/ap661e/ap661e.pdf>, last access: 27 September 2023, 1981.

1092 Fay, A. R. and McKinley, G. A.: Global open-ocean biomes: mean and temporal variability, 6, 273–284,
1093 <https://doi.org/10.5194/essd-6-273-2014>, 2014.

1094 Fischer, G., Nachtergaele, F., Prieler, S., van Velthuisen, H. T., Verelst, L., and Wiberg, D.: Global Agro-ecological Zones
1095 Assessment for Agriculture (GAEZ 2008). IIASA, Laxenburg, Austria and FAO, Rome, Italy, available at:
1096 <https://www.fao.org/soils-portal/data-hub/soil-maps-and-databases/harmonized-world-soil-database-v12/land-cover-data/ar/>,
1097 last access: 27 September 2023, 2008.

1098 Gasser, T. and Ciais, P.: A theoretical framework for the net land-to-atmosphere CO₂ flux and its implications in the
1099 definition of "emissions from land-use change", *Earth Syst. Dynam.*, 4, 171–186, <https://doi.org/10.5194/esd-4-171-2013>,
1100 2013.

1101 GCCA. Concrete Future: The GCCA 2050 Cement and Concrete Industry Roadmap for Net Zero Concrete, available at:
1102 <https://gccassociation.org/concretefuture/>, last access: 2 August 2022, 2021.

1103 Goddijn-Murphy, L. M., Woolf, D. K., Land, P. E., Shutler, J. D., and Donlon, C.: The OceanFlux Greenhouse Gases
1104 methodology for deriving a sea surface climatology of CO₂ fugacity in support of air–sea gas flux studies, 11, 519–541,
1105 <https://doi.org/10.5194/os-11-519-2015>, 2015.

- 1106 Good, S. A., Martin, M. J., and Rayner, N. A.: EN4: Quality controlled ocean temperature and salinity profiles and monthly
1107 objective analyses with uncertainty estimates, *Journal of Geophysical Research: Oceans*, 118, 6704–6716,
1108 <https://doi.org/10.1002/2013JC009067>, 2013.
- 1109 Gouretski, V. and Cheng, L.: Correction for Systematic Errors in the Global Dataset of Temperature Profiles from
1110 Mechanical Bathythermographs, *Journal of Atmospheric and Oceanic Technology*, 37, 841–855,
1111 <https://doi.org/10.1175/JTECH-D-19-0205.1>, 2020.
- 1112 Gouretski, V. and Reseghetti, F.: On depth and temperature biases in bathythermograph data: Development of a new
1113 correction scheme based on analysis of a global ocean database, *Deep Sea Research Part I: Oceanographic Research Papers*,
1114 57, 812–833, <https://doi.org/10.1016/j.dsr.2010.03.011>, 2010.
- 1115 Grassi, G., Conchedda, G., Federici, S., Abad Viñas, R., Korosuo, A., Melo, J., Rossi, S., Sandker, M., Somogyi, Z., and
1116 Tubiello, F. N.: Carbon fluxes from land 2000–2020: bringing clarity on countries’ reporting, *Biogeosciences and*
1117 *biodiversity*, <https://doi.org/10.5194/essd-2022-104>, 2022.
- 1118 Gregg, J. S., Andres, R. J., and Marland, G.: China: Emissions pattern of the world leader in CO₂ emissions from fossil fuel
1119 consumption and cement production, *Geophys. Res. Lett.*, 35, L08806, <https://doi.org/10.1029/2007GL032887>, 2008.
- 1120 Gürses, Ö., Oziel, L., Karakuş, O., Sidorenko, D., Völker, C., Ye, Y., Zeising, M., Butzin, M., and Hauck, J.: Ocean
1121 biogeochemistry in the coupled ocean–sea ice–biogeochemistry model FESOM2.1–REcoM3, *Geoscientific Model*
1122 *Development*, 16, 4883–4936, <https://doi.org/10.5194/gmd-16-4883-2023>, 2023.
- 1123 Hansen, M. C., Potapov, P. V., Moore, R., Hancher, M., Turubanova, S. A., Tyukavina, A., Thau, D., Stehman, S. V., Goetz,
1124 S. J., Loveland, T. R., Kommareddy, A., Egorov, A., Chini, L., Justice, C. O., and Townshend, J. R. G.: High-Resolution
1125 Global Maps of 21st-Century Forest Cover Change, *Science*, 342, 850–853, <https://doi.org/10.1126/science.1244693>, 2013.
- 1126 Harris, I., Jones, P. D., Osborn, T. J., and Lister, D. H.: Updated high-resolution grids of monthly climatic observations - the
1127 CRU TS3.10 Dataset, *Int. J. Climatol.*, 34, 623–642, <https://doi.org/10.1002/joc.3711>, 2014.
- 1128 Harris, I., Osborn, T. J., Jones, P., and Lister, D.: Version 4 of the CRU TS monthly high-resolution gridded multivariate
1129 climate dataset, *Sci Data*, 7, 109, <https://doi.org/10.1038/s41597-020-0453-3>, 2020.
- 1130 Heinemann, A., Mertz, O., Frolking, S., Christensen, A. E., Hurni, K., Sedano, F., Chini, L. P., Sahajpal, R., Hansen, M., and
1131 Hurtt, G.: A global view of shifting cultivation: Recent, current, and future extent, *PLOS ONE*, 12, e0184479,
1132 <https://doi.org/10.1371/journal.pone.0184479>, 2017.
- 1133 Hertwich, E. G. and Peters, G. P.: Carbon Footprint of Nations: A Global, Trade-Linked Analysis, *Environ. Sci. Technol.*,
1134 43, 6414–6420, <https://doi.org/10.1021/es803496a>, 2009.
- 1135 Ho, D. T., Wanninkhof, R., Schlosser, P., Ullman, D. S., Hebert, D., and Sullivan, K. F.: Toward a universal relationship
1136 between wind speed and gas exchange: Gas transfer velocities measured with ³He/SF₆ during the Southern Ocean Gas
1137 Exchange Experiment, *J. Geophys. Res.-Oceans*, 116, C00F04, <https://doi.org/10.1029/2010JC006854>, 2011.
- 1138 Hobeichi, S., Abramowitz, G., Evans, J., and Beck, H. E.: Linear Optimal Runoff Aggregate (LORA): a global gridded
1139 synthesis runoff product, *Hydrol. Earth Syst. Sci.*, 23, 851–870, <https://doi.org/10.5194/hess-23-851-2019>, 2019.
- 1140 Hobeichi, S., Abramowitz, G., and Evans, J.: Conserving Land–Atmosphere Synthesis Suite (CLASS), *Journal of Climate*,
1141 33, 1821–1844, <https://doi.org/10.1175/JCLI-D-19-0036.1>, 2020.
- 1142 Houghton, R. A.: Why are estimates of the terrestrial carbon balance so different?, *Glob. Change Biol.*, 9, 500–509,
1143 <https://doi.org/10.1046/j.1365-2486.2003.00620.x>, 2003.
- 1144 Houghton, R. A. and Nassikas, A. A.: Global and regional fluxes of carbon from land use and land cover change 1850–2015:
1145 Carbon Emissions From Land Use, *Global Biogeochem. Cycles*, 31, 456–472, <https://doi.org/10.1002/2016GB005546>,
1146 2017.
- 1147 Hugelius, G., Bockheim, J. G., Camill, P., Elberling, B., Grosse, G., Harden, J. W., Johnson, K., Jorgenson, T., Koven, C.
1148 D., Kuhry, P., Michaelson, G., Mishra, U., Palmtag, J., Ping, C.-L., O’Donnell, J., Schirrmeister, L., Schuur, E. A. G.,
1149 Sheng, Y., Smith, L. C., Strauss, J., and Yu, Z.: A new data set for estimating organic carbon storage to 3 m depth in soils of
1150 the northern circumpolar permafrost region, *Earth Syst. Sci. Data*, 5, 393–402, <https://doi.org/10.5194/essd-5-393-2013>,
1151 2013.

- 1152 Hurtt, G., Chini, L., Sahajpal, R., Frolking, S., Bodirsky, B. L., Calvin, K., Doelman, J., Fisk, J., Fujimori, S., Klein
1153 Goldewijk, K., Hasegawa, T., Havlik, P., Heinemann, A., Humpenöder, F., Jungclaus, J., Kaplan, J., Krisztin, T., Lawrence,
1154 D., Lawrence, P., Mertz, O., Pongratz, J., Popp, A., Riahi, K., Shevliakova, E., Stehfest, E., Thornton, P., van Vuuren, D.,
1155 and Zhang, X.: input4MIPs.CMIP6.CMIP.UofMD.UofMD-landState-2-1-h, World Climate Research Programme [dataset],
1156 <https://doi.org/10.22033/ESGF/input4MIPs.1127>, 2017.
- 1157 Hurtt, G. C., Chini, L. P., Frolking, S., Betts, R. A., Feddema, J., Fischer, G., Fisk, J. P., Hibbard, K., Houghton, R. A.,
1158 Janetos, A., Jones, C. D., Kindermann, G., Kinoshita, T., Klein Goldewijk, K., Riahi, K., Shevliakova, E., Smith, S.,
1159 Stehfest, E., Thomson, A., Thornton, P., van Vuuren, D. P., and Wang, Y. P.: Harmonization of land-use scenarios for the
1160 period 1500–2100: 600 years of global gridded annual land-use transitions, wood harvest, and resulting secondary lands,
1161 *Climatic Change*, 109, 117–161, <https://doi.org/10.1007/s10584-011-0153-2>, 2011.
- 1162 Hurtt, G. C., Chini, L., Sahajpal, R., Frolking, S., Bodirsky, B. L., Calvin, K., Doelman, J. C., Fisk, J., Fujimori, S., Klein
1163 Goldewijk, K., Hasegawa, T., Havlik, P., Heinemann, A., Humpenöder, F., Jungclaus, J., Kaplan, J. O., Kennedy, J.,
1164 Krisztin, T., Lawrence, D., Lawrence, P., Ma, L., Mertz, O., Pongratz, J., Popp, A., Poulter, B., Riahi, K., Shevliakova, E.,
1165 Stehfest, E., Thornton, P., Tubiello, F. N., van Vuuren, D. P., and Zhang, X.: Harmonization of global land use change and
1166 management for the period 850–2100 (LUH2) for CMIP6, *Geosci. Model Dev.*, 13, 5425–5464,
1167 <https://doi.org/10.5194/gmd-13-5425-2020>, 2020.
- 1168 IEA/OECD: International Energy Agency/Organisation for Economic Cooperation and Development: CO2 emissions from
1169 fuel combustion, available at: <https://webstore.iea.org/co2-emissions-from-fuel-combustion-2019-highlights>, last access: 27
1170 September 2023, 2019.
- 1171 Iida, Y., Kojima, A., Takatani, Y., Nakano, T., Sugimoto, H., Midorikawa, T., and Ishii, M.: Trends in pCO₂ and sea–air
1172 CO₂ flux over the global open oceans for the last two decades, *J Oceanogr*, 71, 637–661, [https://doi.org/10.1007/s10872-](https://doi.org/10.1007/s10872-015-0306-4)
1173 015-0306-4, 2015.
- 1174 Ilyina, T., Six, K. D., Segschneider, J., Maier-Reimer, E., Li, H., and Núñez-Riboni, I.: Global ocean biogeochemistry model
1175 HAMOCC: Model architecture and performance as component of the MPI-Earth system model in different CMIP5
1176 experimental realizations: The Model Hamocce within Mpi-Esm in Cmp5, *J. Adv. Model. Earth Syst.*, 5, 287–315,
1177 <https://doi.org/10.1029/2012MS000178>, 2013.
- 1178 Inness, A., Ades, M., Agustí-Panareda, A., Barré, J., Benedictow, A., Blechschmidt, A.-M., Dominguez, J. J., Engelen, R.,
1179 Eskes, H., Flemming, J., Huijnen, V., Jones, L., Kipling, Z., Massart, S., Parrington, M., Peuch, V.-H., Razinger, M., Remy,
1180 S., Schulz, M., and Suttie, M.: The CAMS reanalysis of atmospheric composition, 19, 3515–3556,
1181 <https://doi.org/10.5194/acp-19-3515-2019>, 2019.
- 1182 Jähne, B.: Air-Sea Gas Exchange, in: *Encyclopedia of Ocean Sciences*, Elsevier, 1–13, [https://doi.org/10.1016/B978-0-12-](https://doi.org/10.1016/B978-0-12-409548-9.11613-6)
1183 409548-9.11613-6, 2019.
- 1184 Jähne, B. and Haußecker, H.: Air-water gas exchange, *Annu. Rev. Fluid Mech.*, 30, 443–468,
1185 <https://doi.org/10.1146/annurev.fluid.30.1.443>, 1998.
- 1186 JODI: Joint Organisations Data Initiative, available at: <https://www.jodidata.org>, last access: 27 September 2023, 2022.
- 1187 Jung, M., Reichstein, M., Schwalm, C. R., Huntingford, C., Sitch, S., Ahlström, A., Arneth, A., Camps-Valls, G., Ciais, P.,
1188 Friedlingstein, P., Gans, F., Ichii, K., Jain, A. K., Kato, E., Papale, D., Poulter, B., Raduly, B., Rödenbeck, C., Tramontana,
1189 G., Viovy, N., Wang, Y.-P., Weber, U., Zaehle, S., and Zeng, N.: Compensatory water effects link yearly global land CO₂
1190 sink changes to temperature, *Nature*, 541, 516–520, <https://doi.org/10.1038/nature20780>, 2017.
- 1191 Keeling, R. F. and Manning, A. C.: 5.15 - Studies of Recent Changes in Atmospheric O₂ Content, in: *Treatise on*
1192 *Geochemistry* (Second Edition), edited by: Holland, H. D. and Turekian, K. K., Elsevier, Oxford, 385–404,
1193 <https://doi.org/10.1016/B978-0-08-095975-7.00420-4>, 2014.
- 1194 Klein Goldewijk, K., Beusen, A., Doelman, J., and Stehfest, E.: Anthropogenic land use estimates for the Holocene – HYDE
1195 3.2, *Earth Syst. Sci. Data*, 9, 927–953, <https://doi.org/10.5194/essd-9-927-2017>, 2017a.
- 1196 Klein Goldewijk, K., Dekker, S. C., and van Zanden, J. L.: Per-capita estimations of long-term historical land use and the
1197 consequences for global change research, *J. Land Use Sci.*, 12, 313–337, <https://doi.org/10.1080/1747423X.2017.1354938>,
1198 2017b.
- 1199 Knauer, J., Zaehle, S., Medlyn, B. E., Reichstein, M., Williams, C. A., Migliavacca, M., De Kauwe, M. G., Werner, C.,
1200 Keitel, C., Kolari, P., Limousin, J., and Linderson, M.: Towards physiologically meaningful water-use efficiency estimates
1201 from eddy covariance data, *Global Change Biology*, 24, 694–710, <https://doi.org/10.1111/gcb.13893>, 2018.

- 1202 Kobayashi, S., Ota, Y., Harada, Y., Ebita, A., Moriya, M., Onoda, H., Onogi, K., Kamahori, H., Kobayashi, C., Endo, H.,
1203 Miyaoka, K., and Takahashi, K.: The JRA-55 Reanalysis: General Specifications and Basic Characteristics, *Journal of the*
1204 *Meteorological Society of Japan*, 93, 5–48, <https://doi.org/10.2151/jmsj.2015-001>, 2015.
- 1205 Landschützer, P., Gruber, N., Bakker, D. C. E., and Schuster, U.: Recent variability of the global ocean carbon sink, *Global*
1206 *Biogeochem. Cycles*, 28, 927–949, <https://doi.org/10.1002/2014GB004853>, 2014.
- 1207 Landschützer, P., Laruelle, G. G., Roobaert, A., and Regnier, P.: A uniform pCO₂ climatology combining open and coastal
1208 oceans, 12, 2537–2553, <https://doi.org/10.5194/essd-12-2537-2020>, 2020.
- 1209 Lasslop, G., Reichstein, M., Papale, D., Richardson, A. D., Arneth, A., Barr, A., Stoy, P., and Wohlfahrt, G.: Separation of
1210 net ecosystem exchange into assimilation and respiration using a light response curve approach: critical issues and global
1211 evaluation: Separation of NEE into GPP and RECO, *Glob. Change Biol.*, 16, 187–208, [https://doi.org/10.1111/j.1365-](https://doi.org/10.1111/j.1365-2486.2009.02041.x)
1212 2486.2009.02041.x, 2010.
- 1213 Lauvset, S. K., Key, R. M., Olsen, A., van Heuven, S., Velo, A., Lin, X., Schirnack, C., Kozyr, A., Tanhua, T., Hoppema,
1214 M., Jutterström, S., Steinfeldt, R., Jeansson, E., Ishii, M., Perez, F. F., Suzuki, T., and Watelet, S.: A new global interior
1215 ocean mapped climatology: the 1° × 1° GLODAP version 2, *Earth System Science Data*, 8, 325–340,
1216 <https://doi.org/10.5194/essd-8-325-2016>, 2016.
- 1217 Liu, Z., Ciais, P., Deng, Z., Davis, S. J., Zheng, B., Wang, Y., Cui, D., Zhu, B., Dou, X., Ke, P., Sun, T., Guo, R., Zhong, H.,
1218 Boucher, O., Bréon, F.-M., Lu, C., Guo, R., Xue, J., Boucher, E., Tanaka, K., and Chevallier, F.: Carbon Monitor, a near-
1219 real-time daily dataset of global CO₂ emission from fossil fuel and cement production, *Sci Data*, 7, 392,
1220 <https://doi.org/10.1038/s41597-020-00708-7>, 2020a.
- 1221 Liu, Z., Ciais, P., Deng, Z., Lei, R., Davis, S. J., Feng, S., Zheng, B., Cui, D., Dou, X., Zhu, B., Guo, R., Ke, P., Sun, T., Lu,
1222 C., He, P., Wang, Y., Yue, X., Wang, Y., Lei, Y., Zhou, H., Cai, Z., Wu, Y., Guo, R., Han, T., Xue, J., Boucher, O.,
1223 Boucher, E., Chevallier, F., Tanaka, K., Wei, Y., Zhong, H., Kang, C., Zhang, N., Chen, B., Xi, F., Liu, M., Bréon, F.-M.,
1224 Lu, Y., Zhang, Q., Guan, D., Gong, P., Kammen, D. M., He, K., and Schellnhuber, H. J.: Near-real-time monitoring of
1225 global CO₂ emissions reveals the effects of the COVID-19 pandemic, *Nat Commun*, 11, 5172,
1226 <https://doi.org/10.1038/s41467-020-18922-7>, 2020b.
- 1227 Ma, L., Hurtt, G. C., Chini, L. P., Sahajpal, R., Pongratz, J., Frohling, S., Stehfest, E., Klein Goldewijk, K., O’Leary, D., and
1228 Doelman, J. C.: Global rules for translating land-use change (LUH2) to land-cover change for CMIP6 using GLM2, *Geosci.*
1229 *Model Dev.*, 13, 3203–3220, <https://doi.org/10.5194/gmd-13-3203-2020>, 2020.
- 1230 Maki, T., Ikegami, M., Fujita, T., Hirahara, T., Yamada, K., Mori, K., Takeuchi, A., Tsutsumi, Y., Suda, K., and Conway, T.
1231 J.: New technique to analyse global distributions of CO₂ concentrations and fluxes from non-processed observational data,
1232 *Tellus B*, 62, 797–809, <https://doi.org/10.1111/j.1600-0889.2010.00488.x>, 2010.
- 1233 Manning, A. and Keeling, R. F.: Global oceanic and land biotic carbon sinks from the Scripps atmospheric oxygen flask
1234 sampling network, *Tellus B Chem. Phys. Meteorol.*, 58, 95–116, <https://doi.org/10.1111/j.1600-0889.2006.00175.x>, 2006.
- 1235 Marland, G.: Uncertainties in Accounting for CO₂ From Fossil Fuels, *J. Indust. Ecol.*, 12, 136–139,
1236 <https://doi.org/10.1111/j.1530-9290.2008.00014.x>, 2008.
- 1237 Marland, G., Hamal, K., and Jonas, M.: How Uncertain Are Estimates of CO₂ Emissions?, *J. Indust. Ecol.*, 13, 4–7,
1238 <https://doi.org/10.1111/j.1530-9290.2009.00108.x>, 2009.
- 1239 Martens, B., Miralles, D. G., Lievens, H., Van Der Schalie, R., De Jeu, R. A. M., Fernández-Prieto, D., Beck, H. E., Dorigo,
1240 W. A., and Verhoest, N. E. C.: GLEAM v3: satellite-based land evaporation and root-zone soil moisture, *Geosci. Model*
1241 *Dev.*, 10, 1903–1925, <https://doi.org/10.5194/gmd-10-1903-2017>, 2017.
- 1242 McNeil, B. I.: Anthropogenic CO₂ Uptake by the Ocean Based on the Global Chlorofluorocarbon Data Set, *Science*, 299,
1243 235–239, <https://doi.org/10.1126/science.1077429>, 2003.
- 1244 Mikaloff Fletcher, S. E., Gruber, N., Jacobson, A. R., Doney, S. C., Dutkiewicz, S., Gerber, M., Follows, M., Joos, F.,
1245 Lindsay, K., Menemenlis, D., Mouchet, A., Müller, S. A., and Sarmiento, J. L.: Inverse estimates of anthropogenic CO₂
1246 uptake, transport, and storage by the ocean, *Glob. Biogeochem. Cycles*, 20, GB2002,
1247 <https://doi.org/10.1029/2005GB002530>, 2006.
- 1248 Miralles, D. G., Holmes, T. R. H., De Jeu, R. A. M., Gash, J. H., Meesters, A. G. C. A., and Dolman, A. J.: Global land-
1249 surface evaporation estimated from satellite-based observations, *Hydrol. Earth Syst. Sci.*, 15, 453–469,
1250 <https://doi.org/10.5194/hess-15-453-2011>, 2011.

- 1251 Mu, Q., Zhao, M., and Running, S. W.: Improvements to a MODIS global terrestrial evapotranspiration algorithm, *Remote*
1252 *Sensing of Environment*, 115, 1781–1800, <https://doi.org/10.1016/j.rse.2011.02.019>, 2011.
- 1253 Müller, J. and Joos, F.: Global peatland area and carbon dynamics from the Last Glacial Maximum to the present – a
1254 process-based model investigation, *Biogeosciences*, 17, 5285–5308, <https://doi.org/10.5194/bg-17-5285-2020>, 2020.
- 1255 Müller, J. and Joos, F.: Committed and projected future changes in global peatlands – continued transient model simulations
1256 since the Last Glacial Maximum, *Biogeosciences*, 18, 3657–3687, <https://doi.org/10.5194/bg-18-3657-2021>, 2021.
- 1257 Myneni, R. B., Ramakrishna, R., Nemani, R., and Running, S. W.: Estimation of global leaf area index and absorbed par
1258 using radiative transfer models, *IEEE Trans. Geosci. Remote Sensing*, 35, 1380–1393, <https://doi.org/10.1109/36.649788>,
1259 1997.
- 1260 Naegler, T.: Reconciliation of excess ^{14}C -constrained global CO_2 piston velocity estimates, *Tellus B.*, 61, 372–384,
1261 <https://doi.org/10.1111/j.1600-0889.2008.00408.x>, 2009.
- 1262 Nakamura, T., Yamazaki, K., Iwamoto, K., Honda, M., Miyoshi, Y., Ogawa, Y., and Ukita, J.: A negative phase shift of the
1263 winter AO/NAO due to the recent Arctic sea-ice reduction in late autumn, *J. Geophys. Res. Atmos.*, 120, 3209–3227,
1264 <https://doi.org/10.1002/2014JD022848>, 2015.
- 1265 Narayanan, B., Aguiar, A., and McDougall, R.: Global Trade, Assistance, and Production: The GTAP 9 Data Base, Cent.
1266 Glob. Trade Anal. Purdue Univ., available at: [https:// www.gtap.agecon.purdue.edu/databases/v9/default.asp](https://www.gtap.agecon.purdue.edu/databases/v9/default.asp), last access: 27
1267 September 2023, 2015.
- 1268 Nightingale, P. D., Liss, P. S., and Schlosser, P.: Measurements of air-sea gas transfer during an open ocean algal bloom,
1269 *Geophys. Res. Lett.*, 27, 2117–2120, <https://doi.org/10.1029/2000GL011541>, 2000.
- 1270 Orr, J. C., Najjar, R. G., Aumont, O., Bopp, L., Bullister, J. L., Danabasoglu, G., Doney, S. C., Dunne, J. P., Dutay, J.-C.,
1271 Graven, H., Griffies, S. M., John, J. G., Joos, F., Levin, I., Lindsay, K., Matear, R. J., McKinley, G. A., Mouchet, A.,
1272 Oschlies, A., Romanou, A., Schlitzer, R., Tagliabue, A., Tanhua, T., and Yool, A.: Biogeochemical protocols and
1273 diagnostics for the CMIP6 Ocean Model Intercomparison Project (OMIP), 10, 2169–2199, [https://doi.org/10.5194/gmd-10-](https://doi.org/10.5194/gmd-10-2169-2017)
1274 2169-2017, 2017.
- 1275 Peters, G. P., Andrew, R., and Lennox, J.: Constructing an environmentally-extended multi-regional input–output table using
1276 the GTAP database, *Economic Systems Research*, 23, 131–152, <https://doi.org/10.1080/09535314.2011.563234>, 2011b.
- 1277 Peters, G. P., Davis, S. J., and Andrew, R.: A synthesis of carbon in international trade, *Biogeosciences*, 9, 3247–3276,
1278 <https://doi.org/10.5194/bg-9-3247-2012>, 2012b.
- 1279 Potapov, P., Hansen, M. C., Laestadius, L., Turubanova, S., Yaroshenko, A., Thies, C., Smith, W., Zhuravleva, I.,
1280 Komarova, A., Minnemeyer, S., and Esipova, E.: The last frontiers of wilderness: Tracking loss of intact forest landscapes
1281 from 2000 to 2013, *Sci. Adv.*, 3, e1600821, <https://doi.org/10.1126/sciadv.1600821>, 2017.
- 1282 Prather, M.: Interactive comment on “Carbon dioxide and climate impulse response functions for the computation of
1283 greenhouse gas metrics: a multi-model analysis” by F. Joos et al., *Atmospheric Chem. Phys. Discuss.*, 12, C8465, 2012.
- 1284 Qiu, C., Ciais, P., Zhu, D., Guenet, B., Peng, S., Petrescu, A. M. R., Lauerwald, R., Makowski, D., Gallego-Sala, A. V.,
1285 Charman, D. J., and Brewer, S. C.: Large historical carbon emissions from cultivated northern peatlands, *Sci. Adv.*, 7,
1286 eabf1332, <https://doi.org/10.1126/sciadv.abf1332>, 2021.
- 1287 Rayner, N. A., Parker, D. E., Horton, E. B., Folland, C. K., Alexander, L. V., Rowell, D. P., Kent, E. C., and Kaplan, A.:
1288 Global analyses of sea surface temperature, sea ice, and night marine air temperature since the late nineteenth century,
1289 *Journal of Geophysical Research: Atmospheres*, 108, <https://doi.org/10.1029/2002JD002670>, 2003.
- 1290 Rayner, P. J., Enting, I. G., Francey, R. J., and Langenfelds, R.: Reconstructing the recent carbon cycle from atmospheric
1291 CO_2 , $\delta^{13}\text{C}$ and O_2/N_2 observations*, *Tellus B*, 51, 213–232, <https://doi.org/10.1034/j.1600-0889.1999.t01-1-00008.x>,
1292 1999.
- 1293 Regnier, P., Friedlingstein, P., Ciais, P., Mackenzie, F. T., Gruber, N., Janssens, I. A., Laruelle, G. G., Lauerwald, R.,
1294 Luyssaert, S., Andersson, A. J., Arndt, S., Arnosti, C., Borges, A. V., Dale, A. W., Gallego-Sala, A., Godd  ris, Y., Goossens,
1295 N., Hartmann, J., Heinze, C., Ilyina, T., Joos, F., LaRowe, D. E., Leifeld, J., Meysman, F. J. R., Munhoven, G., Raymond, P.
1296 A., Spahni, R., Suntharalingam, P., and Thullner, M.: Anthropogenic perturbation of the carbon fluxes from land to ocean,
1297 *Nature Geosci.*, 6, 597–607, <https://doi.org/10.1038/ngeo1830>, 2013.

- 1298 Reichstein, M., Papale, D., Valentini, R., Aubinet, M., Bernhofer, C., Knohl, A., Laurila, T., Lindroth, A., Moors, E.,
1299 Pilegaard, K., and Seufert, G.: Determinants of terrestrial ecosystem carbon balance inferred from European eddy covariance
1300 flux sites, *Geophys. Res. Lett.*, 34, L01402, <https://doi.org/10.1029/2006GL027880>, 2007.
- 1301 Rhein, M., Rintoul, S. R., Aoki, S., Campos, E., Chambers, D., Feely, R. A., Gulev, S., Johnson, G. C., Josey, S. A.,
1302 Kostianoy, A., Mauritzen, C., Roemmich, D., and Talley, L. D.: Observations: Ocean, in: *Climate Change 2013: The*
1303 *Physical Science Basis. Contribution of Working Group I to the Fifth Assessment Report of the Intergovernmental Panel on*
1304 *Climate Change* [Stocker, T. F., Qin, D., Plattner, G.-K., Tignor, M., Allen, S. K., Boschung, J., Nauels, A., Xia, Y., Bex, V.,
1305 and Midgley, P. M. (eds.)], Cambridge University Press, 255–316, ISBN: 9781107057991, 2013.
- 1306 Rödenbeck, C., Bakker, D. C. E., Gruber, N., Iida, Y., Jacobson, A. R., Jones, S., Landschützer, P., Metzl, N., Nakaoka, S.,
1307 Olsen, A., Park, G.-H., Peylin, P., Rodgers, K. B., Sasse, T. P., Schuster, U., Shutler, J. D., Valsala, V., Wanninkhof, R., and
1308 Zeng, J.: Data-based estimates of the ocean carbon sink variability – first results of the Surface Ocean CO₂ Mapping
1309 intercomparison (SOCOM), *Biogeosciences*, 12, 7251–7278, <https://doi.org/10.5194/bg-12-7251-2015>, 2015.
- 1310 Roobaert, A., Laruelle, G. G., Landschützer, P., and Regnier, P.: Uncertainty in the global oceanic CO₂ uptake induced by
1311 wind forcing: quantification and spatial analysis, 15, 1701–1720, <https://doi.org/10.5194/bg-15-1701-2018>, 2018.
- 1312 Rypdal, K., Paciorek, N., Eggleston, S., Goodwin, J., Irving, W., Penman, J., and Woodfield, M.: Volume 1: Introduction to
1313 the 2006 Guidelines in: 2006 IPCC guidelines for national greenhouse gas inventories, available at: [https://www.ipcc-](https://www.ipcc-nggip.iges.or.jp/public/2006gl/vol1.html)
1314 [nggip.iges.or.jp/public/2006gl/vol1.html](https://www.ipcc-nggip.iges.or.jp/public/2006gl/vol1.html), last access: 27 September 2023, 2006.
- 1315 Saatchi, S. S., Harris, N. L., Brown, S., Lefsky, M., Mitchard, E. T. A., Salas, W., Zutta, B. R., Buermann, W., Lewis, S. L.,
1316 Hagen, S., Petrova, S., White, L., Silman, M., and Morel, A.: Benchmark map of forest carbon stocks in tropical regions
1317 across three continents, *Proceedings of the National Academy of Sciences*, 108, 9899–9904,
1318 <https://doi.org/10.1073/pnas.1019576108>, 2011.
- 1319 Santoro, M. and Cartus, O.: ESA Biomass Climate Change Initiative (Biomass_cci): Global datasets of forest above-ground
1320 biomass for the years 2010, 2017 and 2018, v3, <https://doi.org/10.5285/5F331C418E9F4935B8EB1B836F8A91B8>, 2021.
- 1321 Sarmiento, J. L., Orr, J. C., and Siegenthaler, U.: A perturbation simulation of CO₂ uptake in an ocean general circulation
1322 model, *J. Geophys. Res.-Oceans*, 97, 3621–3645, <https://doi.org/10.1029/91JC02849>, 1992.
- 1323 Sato, M., Hansen, J. E., McCormick, M. P., and Pollack, J. B.: Stratospheric aerosol optical depths, 1850–1990, *Geophys.*
1324 *Res.-Atmos.*, 98, 22987–22994, <https://doi.org/10.1029/93JD02553>, 1993.
- 1325 Saunio, M., Stavert, A. R., Poulter, B., Bousquet, P., Canadell, J. G., Jackson, R. B., Raymond, P. A., Dlugokencky, E. J.,
1326 Houweling, S., Patra, P. K., Ciais, P., Arora, V. K., Bastviken, D., Bergamaschi, P., Blake, D. R., Brailsford, G., Bruhwiler,
1327 L., Carlson, K. M., Carrol, M., Castaldi, S., Chandra, N., Crevoisier, C., Crill, P. M., Covey, K., Curry, C. L., Etiope, G.,
1328 Frankenberg, C., Gedney, N., Hegglin, M. I., Höglund-Isaksson, L., Hugelius, G., Ishizawa, M., Ito, A., Janssens-Maenhout,
1329 G., Jensen, K. M., Joos, F., Kleinen, T., Krummel, P. B., Langenfelds, R. L., Laruelle, G. G., Liu, L., Machida, T.,
1330 Maksyutov, S., McDonald, K. C., McNorton, J., Miller, P. A., Melton, J. R., Morino, I., Müller, J., Murguía-Flores, F., Naik,
1331 V., Niwa, Y., Noce, S., O'Doherty, S., Parker, R. J., Peng, C., Peng, S., Peters, G. P., Prigent, C., Prinn, R., Ramonet, M.,
1332 Regnier, P., Riley, W. J., Rosentreter, J. A., Segers, A., Simpson, I. J., Shi, H., Smith, S. J., Steele, L. P., Thornton, B. F.,
1333 Tian, H., Tohjima, Y., Tubiello, F. N., Tsuruta, A., Viovy, N., Voulgarakis, A., Weber, T. S., van Weele, M., van der Werf,
1334 G. R., Weiss, R. F., Worthy, D., Wunch, D., Yin, Y., Yoshida, Y., Zhang, W., Zhang, Z., Zhao, Y., Zheng, B., Zhu, Q., Zhu,
1335 Q., and Zhuang, Q.: The Global Methane Budget 2000–2017, *Earth Syst. Sci. Data*, 12, 1561–1623,
1336 <https://doi.org/10.5194/essd-12-1561-2020>, 2020.
- 1337 Schuldt, Kenneth N., John Mund, Ingrid T. Luijkx, Tuula Aalto, James B. Abshire, Ken Aikin, Arlyn Andrews, Shuji Aoki,
1338 Francesco Apadula, Bianca Baier, Peter Bakwin, Jakub Bartyzel, Gilles Bentz, Peter Bergamaschi, Andreas Beyersdorf,
1339 Tobias Biermann, Sebastien C. Biraud, Harald Boenisch, David Bowling, Gordon Brailsford, Willi A. Brand, Huilin Chen,
1340 Gao Chen, Lukasz Chmura, Shane Clark, Sites Climadat, Aurelie Colomb, Roisin Commene, Sébastien Conil, Cedric
1341 Couret, Adam Cox, Paolo Cristofanelli, Emilio Cuevas, Roger Curcoll, Bruce Daube, Kenneth Davis, Martine De Mazière,
1342 Stephan De Wekker, Julian Della Coletta, Marc Delmotte, Joshua P. DiGangi, Ed Dlugokencky, James W. Elkins, Lukas
1343 Emmenegger, Shuangxi Fang, Marc L. Fischer, Grant Forster, Arnoud Frumau, Michal Galkowski, Luciana V. Gatti,
1344 Torsten Gehrlein, Christoph Gerbig, Francois Gheusi, Emanuel Gloor, Vanessa Gomez-Trueba, Daisuke Goto, Tim Griffis,
1345 Samuel Hammer, Chad Hanson, László Haszpra, Juhana Hatakka, Martin Heimann, Michal Heliasz, Daniela Heltai, Arjan
1346 Hensen, Ove Hermanssen, Eric Hintsa, Antje Hoheisel, Jutta Holst, Viktor Ivakhov, Dan Jaffe, Armin Jordan, Warren
1347 Joubert, Anna Karion, Stephan R. Kawa, Victor Kazan, Ralph Keeling, Petri Keronen, Joil Kim, Tobias Kneuer, Pasi
1348 Kolari, Katerina Kominkova, Eric Kort, Elena Kozlova, Paul Krummel, Dagmar Kubistin, Casper Labuschagne, David H.
1349 Lam, Xin Lan, Ray Langenfelds, Olivier Laurent, Tuomas Laurila, Thomas Lauvaux, Jost Lavric, Bev Law, Olivia S. Lee,
1350 John Lee, Irene Lehner, Kari Lehtinen, Reimo Leppert, Ari Leskinen, Markus Leuenberger, Ingeborg Levin, Janne Levula,
1351 John Lin, Matthias Lindauer, Zoe Loh, Morgan Lopez, Chris R. Lunder, Toshinobu Machida, Ivan Mammarella, Giovanni
1352 Manca, Alistair Manning, Andrew Manning, Michal V. Marek, Melissa Y. Martin, Giordane A. Martins, Hidekazu

- 1353 Matsueda, Kathryn McKain, Harro Meijer, Frank Meinhardt, Lynne Merchant, N. Mihalopoulos, Natasha Miles, John B.
1354 Miller, Charles E. Miller, Logan Mitchell, Stephen Montzka, Fred Moore, Heiko Moossen, Eric Morgan, Josep-Anton
1355 Morgui, Shinji Morimoto, Bill Munger, David Munro, Cathrine L. Myhre, Meelis Mölder, Jennifer Müller-Williams,
1356 Jaroslaw Necki, Sally Newman, Sylvia Nichol, Yosuke Niwa, Simon O'Doherty, Florian Obersteiner, Bill Paplawsky, Jeff
1357 Peischl, Olli Peltola, Salvatore Piacentino, Jean M. Pichon, Steve Piper, Joseph Pitt, Christian Plass-Duelmer, Stephen M.
1358 Platt, Steve Prinzivalli, Michel Ramonet, Ramon Ramos, Enrique Reyes-Sanchez, Scott Richardson, Haris Riris, Pedro P.
1359 Rivas, Michael Rothe, Thomas Ryerson, Kazuyuki Saito, Maryann Sargent, Motoki Sasakawa, Bert Scheeren, Martina
1360 Schmidt, Tanja Schuck, Marcus Schumacher, Thomas Seifert, Mahesh K. Sha, Paul Shepson, Michael Shook, Christopher
1361 D. Sloop, Paul Smith, Martin Steinbacher, Britton Stephens, Colm Sweeney, Lise L. Sørensen, Pieter Tans, Kirk Thoning,
1362 Helder Timas, Margaret Torn, Pamela Trisolino, Jocelyn Turnbull, Kjetil Tørseth, Alex Vermeulen, Brian Viner, Gabriela
1363 Vitkova, Stephen Walker, Andrew Watson, Ray Weiss, Steve Wofsy, Justin Worsley, Doug Worthy, Dickon Young, Sönke
1364 Zaehle, Andreas Zahn, Mirosław Zimnoch, Rodrigo A. de Souza, Alcide G. di Sarra, Danielle van Dinter, Pim van den
1365 Bulk; Multi-laboratory compilation of atmospheric carbon dioxide data for the period 1957-2021;
1366 obspack_co2_1_GLOBALVIEWplus_v8.0 2022-08-27; NOAA Earth System Research Laboratory, Global Monitoring
1367 Laboratory. <http://doi.org/10.25925/20220808>, 2022.
- 1368 Schuldt, Kenneth N., Andrew R. Jacobson, Tuula Aalto, Arlyn Andrews, Francesco Apadula, Sabrina Arnold, Peter Bakwin,
1369 Peter Bergamaschi, Tobias Biermann, Sebastien C. Biraud, Huilin Chen, Aurelie Colomb, Sébastien Conil, Cédric Couret,
1370 Paolo Cristofanelli, Martine De Mazière, Stephan De Wekker, Marc Delmotte, Ed Dlugokencky, Lukas Emmenegger, Marc
1371 L. Fischer, Grant Forster, Juha Hatakka, Michal Heliasz, Daniela Heltai, Ove Hermansen, Antje Hoheisel, Jutta Holst,
1372 Daniel A. Jaffe, Anna Karion, Victor Kazan, Petri Keronen, Tobias Kneuer, Katerina Kominkova, Dagmar Kubistin, Xin
1373 Lan, Olivier Laurent, Tuomas Laurila, John Lee, Irene Lehner, Kari Lehtinen, Ari Leskinen, Markus Leuenberger, Matthias
1374 Lindauer, Morgan Lopez, Chris R. Lunder, Ivan Mammarella, Giovanni Manca, Michal V. Marek, Kathryn McKain, Frank
1375 Meinhardt, Charles E. Miller, John B. Miller, Cathrine L. Myhre, Meelis Mölder, Jennifer Müller-Williams, Salvatore
1376 Piacentino, Jean M. Pichon, Penelope Pickers, Joseph Pitt, Christian Plass-Dülmer, Stephen M. Platt, Michel Ramonet, Bert
1377 Scheeren, Martina Schmidt, Marcus Schumacher, Mahesh K. Sha, Christopher D. Sloop, Paul D. Smith, Martin Steinbacher,
1378 Colm Sweeney, Lise L. Sørensen, Pieter Tans, Kirk Thoning, Pamela Trisolino, Kjetil Tørseth, Brian Viner, Gabriela
1379 Vitkova, Alcide G. di Sarra; Multi-laboratory compilation of atmospheric carbon dioxide data for the period 2022-2023;
1380 obspack_co2_1_NRT_v8.1 2023-02-08; NOAA Earth System Research Laboratory, Global Monitoring Laboratory.
1381 <http://doi.org/10.25925/20230201>, 2023.
- 1382 Souza, C. M., Z. Shimbo, J., Rosa, M. R., Parente, L. L., A. Alencar, A., Rudorff, B. F. T., Hasenack, H., Matsumoto, M., G.
1383 Ferreira, L., Souza-Filho, P. W. M., de Oliveira, S. W., Rocha, W. F., Fonseca, A. V., Marques, C. B., Diniz, C. G., Costa,
1384 D., Monteiro, D., Rosa, E. R., Vélez-Martin, E., Weber, E. J., Lenti, F. E. B., Paternost, F. F., Pareyn, F. G. C., Siqueira, J.
1385 V., Viera, J. L., Neto, L. C. F., Saraiva, M. M., Sales, M. H., Salgado, M. P. G., Vasconcelos, R., Galano, S., Mesquita, V.
1386 V., and Azevedo, T.: Reconstructing Three Decades of Land Use and Land Cover Changes in Brazilian Biomes with
1387 Landsat Archive and Earth Engine, Remote Sens., 12, 2735, <https://doi.org/10.3390/rs12172735>, 2020.
- 1388 Thomason, L. W., Ernest, N., Millán, L., Rieger, L., Bourassa, A., Vernier, J.-P., Manney, G., Luo, B., Arfeuille, F., and
1389 Peter, T.: A global space-based stratospheric aerosol climatology: 1979–2016, 10, 469–492, <https://doi.org/10.5194/essd-10-469-2018>, 2018.
- 1391 Thurner, M., Beer, C., Santoro, M., Carvalhais, N., Wutzler, T., Schepaschenko, D., Shvidenko, A., Kompter, E., Ahrens, B.,
1392 Levick, S. R., and Schmullius, C.: Carbon stock and density of northern boreal and temperate forests, Global Ecology and
1393 Biogeography, 23, 297–310, <https://doi.org/10.1111/geb.12125>, 2014.
- 1394 Tohjima, Y., Mukai, H., Machida, T., Hoshina, Y., and Nakaoka, S.-I.: Global carbon budgets estimated from atmospheric
1395 O₂/N₂ and CO₂ observations in the western Pacific region over a 15-year period, 19, 9269–9285,
1396 <https://doi.org/10.5194/acp-19-9269-2019>, 2019.
- 1397 Tramontana, G., Jung, M., Schwalm, C. R., Ichii, K., Camps-Valls, G., Ráduly, B., Reichstein, M., Arain, M. A., Cescatti,
1398 A., Kiely, G., Merbold, L., Serrano-Ortiz, P., Sickert, S., Wolf, S., and Papale, D.: Predicting carbon dioxide and energy
1399 fluxes across global FLUXNET sites with regression algorithms, Biogeosciences, 13, 4291–4313, <https://doi.org/10.5194/bg-13-4291-2016>, 2016.
- 1401 UN: United Nations Statistics Division: National Accounts Main Aggregates Database, available at:
1402 <http://unstats.un.org/unsd/snaama/Introduction.asp>, last access: 27 September 2023, 2021.
- 1403 Vermote, E. and NOAA CDR Program: NOAA Climate Data Record (CDR) of AVHRR Leaf Area Index (LAI) and
1404 Fraction of Absorbed Photosynthetically Active Radiation (FAPAR), Version 5, <https://doi.org/10.7289/V5TT4P69>, 2018.
- 1405 Viovy, N.: CRUNCEP data set, available at:
1406 ftp://nacp.ornl.gov/synthesis/2009/frescati/temp/land_use_change/original/readme.htm, last access: 27 September 2023,
1407 2016.

- 1408 Wanninkhof, R.: Relationship between wind speed and gas exchange over the ocean, *J. Geophys. Res.-Oceans.*, 97, 7373–
1409 7382, <https://doi.org/10.1029/92JC00188>, 1992.
- 1410 Wanninkhof, R.: Relationship between wind speed and gas exchange over the ocean revisited, *Limnol. Oceanogr. Methods.*,
1411 12, 351–362, <https://doi.org/10.4319/lom.2014.12.351>, 2014.
- 1412 Wanninkhof, R., Park, G.-H., Takahashi, T., Sweeney, C., Feely, R., Nojiri, Y., Gruber, N., Doney, S. C., McKinley, G. A.,
1413 Lenton, A., Le Quéré, C., Heinze, C., Schwinger, J., Graven, H., and Khatiwala, S.: Global ocean carbon uptake: magnitude,
1414 variability and trends, *Biogeosciences*, 10, 1983–2000, <https://doi.org/10.5194/bg-10-1983-2013>, 2013.
- 1415 Weiss, R. F. and Price, B. A.: Nitrous oxide solubility in water and seawater, *Marine Chemistry*, 8, 347–359,
1416 [https://doi.org/10.1016/0304-4203\(80\)90024-9](https://doi.org/10.1016/0304-4203(80)90024-9), 1980.
- 1417 Zheng, B., Chevallier, F., Yin, Y., Ciais, P., Fortems-Cheiney, A., Deeter, M. N., Parker, R. J., Wang, Y., Worden, H. M.,
1418 and Zhao, Y.: Global atmospheric carbon monoxide budget 2000–2017 inferred from multi-species atmospheric inversions,
1419 *Earth Syst. Sci. Data*, 11, 1411–1436, <https://doi.org/10.5194/essd-11-1411-2019>, 2019.